Metrology and Characterization of Electrically Conductive Filaments (ECF) for Fused Deposition Modeling (FDM).

by

Mauricio Henriquez Schott

A dissertation submitted to the Graduate Faculty of
Auburn University
in partial fulfillment of the
requirements for the Degree of
Doctor of Philosophy

Auburn, Alabama
December 14, 2019

Keywords: additive manufacturing, conductive filaments, characterization

Approved by

Jorge Valenzuela, Chair, Philpott-WestPoint Stevens Endowed Distinguished Professor of Industrial and Systems Engineering, Auburn University
David Blersch, Assistant Professor of Biosystems Engineering, Auburn University
Daniel E. Wells, Assistant Professor of Agriculture, Auburn University
Andres Carrano, Professor and Associate Dean for Research of Manufacturing Engineering, Georgia Southern University

Acknowledgments

To my mother, my brother and the family I was born with, but also to my friends, the family that life gave me.

Table of Contents

List of Figures

List of Tables

Chapter 1

Introduction

Current electronics manufacturing is composed of several processes, usually with a high energy, space and knowledge footprint costs to produce a working product. The product is assembled from subcomponents such as the PCB, case and peripherals among others. Each of them requires several steps and multiple machines to be produced. Electronics boards require PCB routers, components mounting, and a soldering oven. The case and mounting require molding or CNC equipment, components such as bolts and nuts, and an assortment of assembly tools (such as screwdriver and pliers). Most of this equipment consumes a significant amount of energy to operate. This situation makes the production of electronics devices a centralized endeavor, where only certain locations around the world supply the global demand. In recent years, small volume and fast delivery of electronics has become available for small demand. Still, the amount of equipment and energy required to operate those production systems is excessive. In some cases, like the arctic or deeps space stations, or prolonged underwater missions, access to these locations presents a significant challenge. In these cases, a spare part may not be available and its on-time delivery may be impossible.

Additive Manufacturing (AM) technology offers a potential solution to at least some of these challenges. Technologies such as *Fusion Deposition Modeling (FDM)* , where shapes are built layer by layer using different polymers, can build, with just one machine, high complex geometries with materials that can withstand high temperatures and be chemical-resistant. In recent years, FDM machines can use *Electrically Conductive Filaments (ECF)* to make the integration of electronics features such as electric traces, antennas, heat sinks, resistors and touch buttons, possible within the process of manufacturing the device itself. While the machine uses

a regular plastic to print the case and support structures, the printing machine switches to a conductive filament to add electric paths and interface buttons that are completed by a rubber material that is also 3D printed using the same machine. After the printing is finished, adding the battery, screen and other components becomes easy by using the connectors and terminals already set in place by the printing process. The whole building and assembly process is reduced in terms of tooling, personnel and expertise required. Fewer tools and less equipment to operate can also reduce the risk of injury and supply of spare parts on-demand. If raw stock materials are impossible to produce in-situ, remote locations would still need to supply them. Nevertheless, in this case, it is more flexible to manufacture what is needed, instead of waiting for components and spare parts.

Several types of ECF materials are available in the market that have different resistivity properties. In order to use these materials in real scenarios, we need to understand their principal characteristics.

The goal of this dissertation is to characterize these new composite materials for proper use and understand their limitations. The characterization of the electric resistivity of the material and the resistance of printed specimens is the focus of this research. Three main objectives are defined to accomplish this goal.

Objective 1 - Ensuring correct measurements of electric resistivity and resistance of ECF materials:

The first objective of this research is to ensure correct measurements of the resistivity and resistance of raw and printed ECF specimens using the FDM technology. A *Crossed Gage Repeatability and Reproducibility (Gage R&R)* study will be used [7] to answer the following research questions:

- How much of the variability in the measured resistivity/resistance of raw and printed ECF specimens is caused by the metrology system? - Repeatability
- How much of the variability in the measured resistivity/resistance of raw and printed ECF specimens is caused by the operator? - Reproducibility

- Can the metrology system discriminate between specimens printed by using different manufacturer materials? - Part-to-Part factor

The study will compare ten metrology systems under three operators, six raw and six printed specimens from five manufacturers. The systems will include metrology equipment recommended or used in the literature about electrical resistivity measurements [8, 9, 10, 11, 12]. The ten metrology systems will be validated by using common resistance components (non-ECF materials) under the same experimental conditions as using the ECF materials.

Objective 2 - Characterization of the electric resistivity/resistance of ECF materials:

A metrology system with the higher precision will be selected from the study of objective 1.

The system will be used to measure and report the resistivity and resistances of specimens according to the Standard Test Method for D-C Resistance or Conductance of Moderately Conductive Materials, ASTM D4496-13 [13].

The method is suggested for materials that exhibit volume resistivity in the range of 10^0 to $10^7\Omega - cm$. It also describes a special fixture called Test Cell, also known as Resistivity Cell [13, p. 3]. The Test Cell has been shown to be satisfactory for measurements in moderately conductive materials.

The purpose of this fixture is to standardize the electrode placement and pressure along different operator readings. The following research questions will be addressed:

- How accurate are the reported resistivity and resistance of the ECF materials from the manufacturers compared to the measured specimens?

- Does the FDM printing process alter the resistivity and resistance of the printed ECF materials?

With the selected metrology system, the study will measure resistivity and resistance of five printed specimens from each manufacturer as also five raw samples. Each specimen will be measured under controlled laboratory conditions by an operator in each of the two major

isotropic axes. The measurement will be aggregated, and the results reported according to the ASTM D4496-13 standard.

Objective 3 - ECF characterization of H_2O condition effects over electric resistance response:

The results from objectives 1 and 2 will be used to select an ECF material to study the effects on the electric resistance measurements at different conditions or states of ECF samples (dry, wet). A characterization of the behavior of the material under different conditions will be reported.

The following research questions will be addressed:

- Is possible to detect the different conditions/states of ECF samples after dry-wet cycles?
- Do the Wet-Dry cycles produce a detectable repetitive cyclic change in the electrical resistance response of ECF samples?
- How much time is needed to produce a change in the electric resistance of the ECF samples when they are submerge in water?
- What are the effects of different infill pattern angles on the detection of the electric resistance response?

Two specimens of each infill pattern angle will be printed with the selected ECF material. Six Dry-Wet cycles will be produced, data about electric resistance and mass will be registered under controlled laboratory conditions (samples will be dried in between each cycle). An automatic electric resistance measuring system will perform one read per hour during the complete water-submerge period to collect additional data.

Chapter 2

Background and Literature Review

2.1 Filament Deposition Modeling (FDM)

The Filament Deposition Modeling (FDM) technique is one of the most common "Additive Manufacturing" (AM) technologies (Figure 2.1). The machine uses a print head (1) to distribute the material layer by layer over a flat surface or "Print Bed". The mechanism can be composed of one or more nozzles that can have one or many sources of raw materials. An extruder, pulls the raw filament into the heat-block (lower section of the print head), where the material is melted to a soft point to be molded. Either a gantry, Cartesian motion system, or both, moves the print bed (2) and the print head, in X/Y coordinates. After each layer is printed, the Z mechanism (3) lifts the print head or lower the print bed. By repeating this process, it is possible to form a 3D object of high complexity and many types of materials and properties.

Just in recent years, FDM machines have become able to use *Electrically Conductive Filaments (ECF)* to embed electronics features such as: electric traces, antennas, heat sinks, resistors, and touch buttons as part of the manufacturing of the device itself.

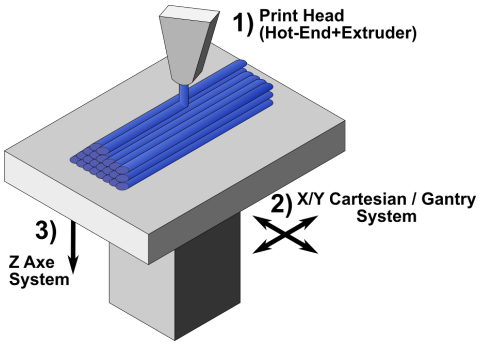

Figure 2.1: Filament Deposition Modeling (FDM)

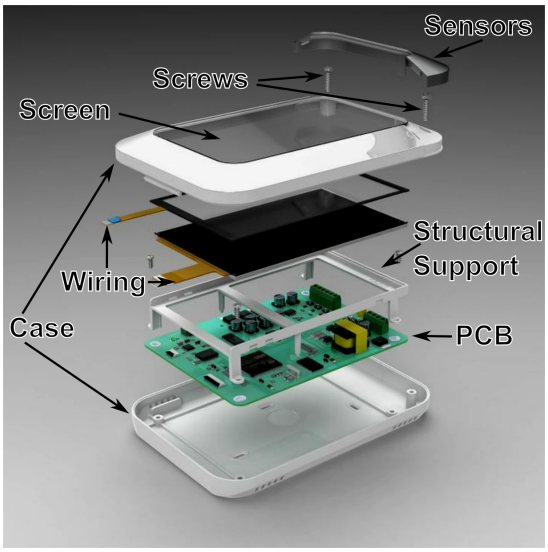

(a) Common electronic device components

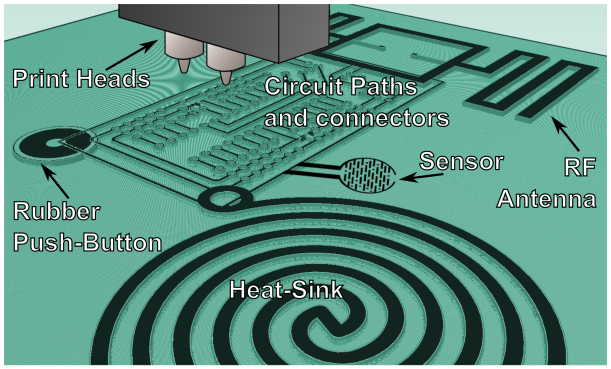

(b) FDM printed electronics features

Figure 2.2: Current embedded electronic devices, compared to 3D printed embedded electronics

2.2 Embedded Electronics

Embedded Electronics devices integrate electronic and mechanical components into a single unit. Cell phones, TV sets and microwaves are examples of embedded electronics devices. Figure 2.2a presents typical components of an electronic devices. The manufacturing of electronic device uses large amounts of energy and requires extensive time and high level skills, which implies a high-cost infrastructure[14]. The manufacturing of PCB boards requires conductive traces, component placement and soldering. These steps are energy-demanding processes. The cases and enclosure are made by injection molding or subtractive technologies such as CNC or laser cutting, which are also high energy consuming technologies. In addition, components require an assembly process using elements such as: bolts, nuts, and many tools (screw drivers, pliers, holders) [15]. However, remote locations (arctic pole bases, outer space or underwater exploration), have fixed supply, energy and space constraints. Since demand for new devices and spare parts would be limited in these cases, this type of electronic manufacturing technology would not be possible here [16, 17, 18].

Recent advances in additive manufacturing, have allowed researchers to develop new technologies for embedded electronics [19]. Development of Aerosol Jet printing, micro extrusion

and composite filaments, allow a user to print very fine electric features, even on curved surfaces. This technique could potentially replace traditional circuit board manufacturing by integrating the electronics directly on the parts [20]. Voxel8 is a company that uses these new advances in one of the machines they produce, where embedded electronics can be printed along with structural elements [21].

Composite semi-conductive materials have become available in form of filaments for *Fusion Deposition Modeling (FDM)* technologies. Potential development areas for these materials are: conductive traces, sensors, RF antennas and Shields, Heat-Sinks, among others. These electronic features can be built as part of the normal FDM additive manufacturing process [22, 23, 24, 25].

The FDM machine uses a high-performance thermoplastic as substrate, providing necessary structural support. When specified, the machine changes to a conductive filament to draw electronics features in one or several layers. After that, it can continue with a rubber-type filament to incorporate flexible features like buttons and handles. The print process can also pause at intervals for operators to add components that cannot be printed (motors, ICs, etc.). The build finishes with an impact resistant plastic to enclose the object, all done by a single unmodified FDM printer in a single low-cost process. After the printing, the battery, screen and other components can snap-in to printed connectors. Figure 2.2b shows a conceptual diagram of an FDM machine printing electronic features a long with the support structures.

Electronics features integrated with high performance thermoplastics during the same process will produce devices that are ready to use with plug-and-play features (not requiring any wiring, soldering or assembly) reducing significantly the number of machines, skills, time and energy involved in the manufacturing of embedded electronics.

Five manufacturers offering variants of ECF for FDM have been selected. They provide a different mix of binder and conductive material, resulting on different resistivity (table 2.1). Due to the FDM process, the printed samples of ECF material present two anisotropy axes. On the X/Y print bed plane, the material is distributed as a continuous flow (direction A). On the Z print axis direction, the material is stocked layer by layer (direction B). Therefore, ECF printed samples present different resistivity/resistance values according to the direction

of placing the electrodes. The values shown in table 2.1 correspond to measurements in the anisotropic direction A (perpendicular to layers). Just few manufacturers provide information on the resistivity/resistance of raw material in the anisotropic direction B.

Brand	**Origin**	**Product**	**Resistivity** ($\Omega - cm$)	**Composition**
Multi3D [26]	US	Electrifi	0.006	unknown
Functionalize [27]	US	F-Electric	0.75	Carbon nano-tube, PLA
Black Magic 3D [28]	US	Conductive Graphene PLA	0.6	Graphene, PLA
PMG3D [29]	China	GraphenePLA (GPLA-C/Z2W ZY)	1	Graphene, PLA
Proto-Pasta [30]	US	Composite PLA	30	Graphite, PLA
*Resistivity correspond to printed samples in the anisotropic direction where is measured perpendicular to layers.				

Table 2.1: Electrically Conductive Filaments (ECF) for FDM

2.3 Experimental Techniques for Measuring Resistivity

The electrical resistance of an object is the measure of its opposition to the flow of electric current. The volume resistivity is the measure of a material resistance to electricity within a cubic centimeter of material.

Measurements below $1k\Omega$ are typically considered low level resistance [31]. Test leads and contact points resistance between electrodes (probes) and the test specimen can introduce measurement errors. In addition, voltages across the test specimen produced by thermal emfs at the junctions between different metals may induce more errors. Therefore, it is important to use a proper equipment to minimize these measurement errors at low resistances levels.

Two techniques, two-point and four-point, for measuring resistivity are presented in literature [8, 7.3]. The techniques can be used to measure resistivity and resistance on raw filament samples and test specimens produced by FDM.

2.3.1 Two-Point Technique

Resistivity can be obtained by measuring the resistance on a specimen with known dimensions. Figure 2.3a, shows a rectangular shape, where length l, height h, and width w are known values. Both ends of the sample are connected to a voltage source V. The voltage source causes a current to flow through the bar. The amount of current that flows through the bar is

measured by the ammeter that is connected in series between the sample and voltage source. The voltage drop across the ammeter is considered negligible. Is also possible to force a current to flow through the sample using a current source. In this case a voltmeter in parallel with the current source measures the induced voltage on the sample.

The resistance R of the sample is given by Equation 2.1

$$R = \frac{V}{I} \tag{2.1}$$

where

R = Resistance in Ohms (Ω)

V = Voltage in volts

I = Current in amps

The physical dimensions of the specimen can be measured with a micrometer, or other appropriate instrument. The two-point resistivity of the material is then:

$$\rho = \frac{Rwh}{l} \tag{2.2}$$

where

ρ = Resistivity in Ohms meter ($\Omega - m$)

R = Measured Resistance in Ohms (Ω)

w = Specimen Width in meters (m)

h = Specimen Height in meters (m)

l = Specimen Length in meters (m)

In equation 2.2, R is multiplied by the cross-sectional area of the specimen. The case of a rectangular bar is $w * h$.

For a cylindrical sample, the cross-sectional area is calculated as in equation 2.3.

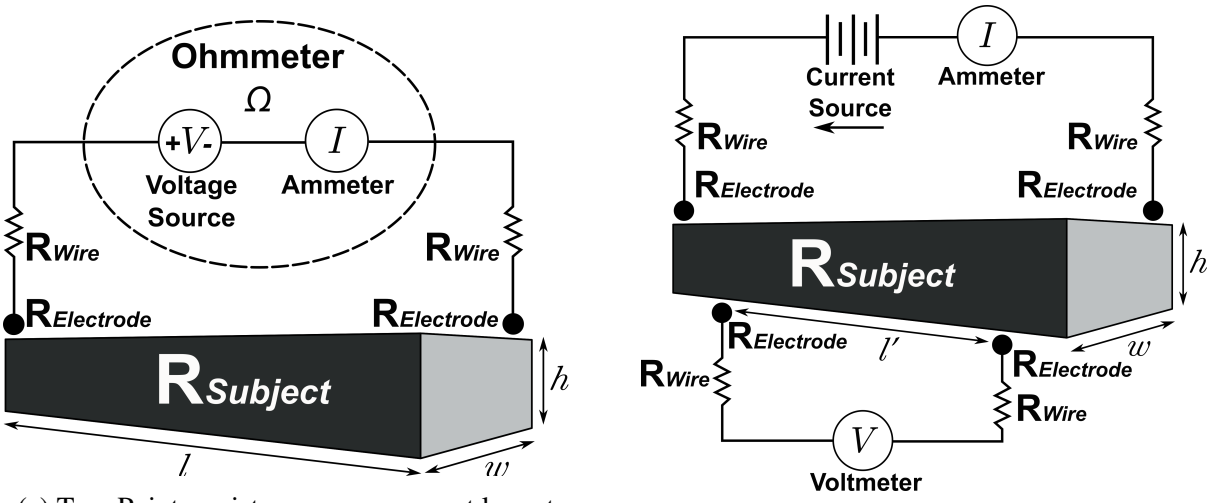

(a) Two-Points resistance measurement layout

(b) Four-Points resistivity measurement layout

Figure 2.3: Resistivity/Resistance measurement techniques

$$A = \pi \times r^2 \tag{2.3}$$

where

A = Circumference Area in meter square (m^2)

r = Circumference radius in meters (m)

Figure 2.3a shows that $ohmmeter$ performs as a voltage and ammeter source, all in one, presenting calculated R. The same functionality applies to equipment 2.4a, 2.4b and 2.4c.

Literature present issues that the two-point technique can encounter [9, 17-23], among them:

In [9, 17-23] have been pointed out that the two-point technique presents some issues:

- Resistances between the contact wires and the sample and with the measuring equipment could provide a higher resistivity than the real value.
- In semi-conducting materials, the applied current could modulate the sample resistivity.
- Contacts between metal electrodes and the semi-conducting sample tend to have other electrical properties which provide wrong measures of the actual sample resistivity.

The four-point measurement technique can overcome these issues.

2.3.2 Four-Point Technique

The four-point measurement technique is illustrated in figure 2.3b. In this technique, four wires are attached to the specimen. A current source is used to force a constant current to flow through the specimen. A separate ammeter, connected in series with the current source, measures the amount of current I passing through. Simultaneously, a voltmeter connected in parallel, measures the voltage V produced across the inner part of the specimen. Another option is to use a voltage source to apply a voltage across the outer contacts, at the same time, the ammeter and voltmeter in series measures the current and voltage. Although this technique may introduce resistance components ($R_{Wire}, R_{Electrode}$), the voltmeter wires carry a low current. The connecting wires between the instrument and the subject resistance may drop insignificant amounts of voltage, giving a measurement close to as if it was connected directly to the sample. Due to the position of the voltmeter electrodes, any drop on the voltage of the electric current wires is not be measured, hence not taken into account in the resistance calculation [8, 7.3].

The four-point resistivity of the material is then:

$$\rho = \frac{Vwh}{Il'} \tag{2.4}$$

where

ρ = Resistivity in Ohms meter (Ωm)

V = Voltage measured by the voltmeter in volts

w = Specimen Width in meters (m)

h = Specimen Height in meters (m)

I = Current the ammeter measures flowing through the sample in amperes

l' = Distance between the two points where the voltmeter wires make contact to the sample, measured in meters (m)

The total length l of the specimen is not used to calculate the four-point resistivity. Instead, the inner length l' between the voltmeter contact points is used.

For cylindrical specimens, the cross-sectional area is calculated as in equation 2.3.

2.4 Instrumentation

The combination of resistivity/resistance measuring technique (two or four points), equipment and electrodes produce different "Metrology Systems". Table 2.2 presents a summary of potential metrology systems found in electrical conductivity literature that can be applied to resistivity/resistance measurements of ECF materials [8, 9, 10, 11, 12].

System	Technique	Equipment	Electrodes/Fixture
1	Two-Points	Manual Handheld Multimeter (Fig.2.4a)	Tip Probe (Fig.2.5a)
2	Two-Points	Manual Handheld Multimeter	Alligator clip test lead (Fig.2.5b)
3	Two-Points	Automatic Handheld Multimeter (Fig.2.4b)	Tip Probe
4	Two-Points	Automatic Handheld Multimeter	Alligator clip test lead
5	Two-Points	Benchtop Digital Multimeter (Fig.2.4c)	Tip Probe
6	Two-Points	Benchtop Digital Multimeter	Alligator clip test lead
7	Four-Points	Benchtop Digital Multimeter	Alligator clip test lead
8	Four-Points	Benchtop Digital Multimeter	Pressure Cell (Fig.2.5c)
9	Four-Points	Constant Current (Fig.2.4d)	Alligator clip test lead
10	Four-Points	Constant Current	Pressure Cell

Table 2.2: Metrology Systems for Electrically Conductive Filaments (ECF) Resistivity/Resistance Measurement

In [10, 11, 12], the resistivity of samples produced by FDM additive manufacturing technologies using ECF material were measured using the metrology systems 1 through 6.

In Table 2.2, the first four systems use the two-point technique available for handheld instrument (2.4a, 2.4b). The two types of electrodes commonly used in these systems are tip probe 2.5a and alligator clip 2.5b. In the electrical conductivity literature, more precise equipment is suggested [8, 9]. Systems 5 to 8 correspond to a laboratory benchtop digital multimeter (2.4c). This instrument offers two and four point connection techniques with higher precision and calibration. Systems 9 and 10 are more complex setup of four-point (2.4c). The instrument produces a constant current source while an ammeter and voltmeter obtain independent measures of current and voltage, respectively. Systems 9 and 10 are different to

System 7 and 8 because the two instruments are integrated into one equipment. Systems 9 and 10 also include the use of alligator clip test leads and the pressure cell.

(a) CenTech P37772, Manual Handheld Multimeter

(b) Klein Tools MM200, Automatic Handheld Multimeter

(c) Keithley 2000, Benchtop Multimeter

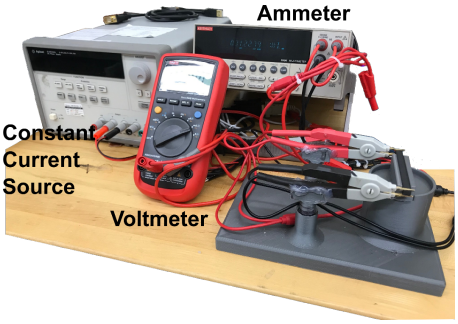

(d) Constant Current 4-Point setup

Figure 2.4: Selected resistance/resistivity measurement instruments.

2.4.1 Electrodes

The tip probe and alligator clip test leads (figure 2.5a and 2.5b) are commonly used in electronic measurements literature [8, 9], and found in commercial products documentation [32, 33, 34, 35, 36]. The resistivity cell fixture (2.5c) is specially designed for this research and uses the four- point technique. The literature and user manuals of electronic measurement equipment [8, 9], indicate the importance of electrode placement and pressure, and the maximum time per reading (no more than one minute). Variations in these factors can introduce a significant amount of noise on the measurements. Precautions must be taken during the experiment to firmly attach the electrodes to the test specimens and ensure that they are placed at the same location at each measurement within a maximum of one minute. The objective is to obtain

(a) Tip Probe

(b) Alligator clip test lead

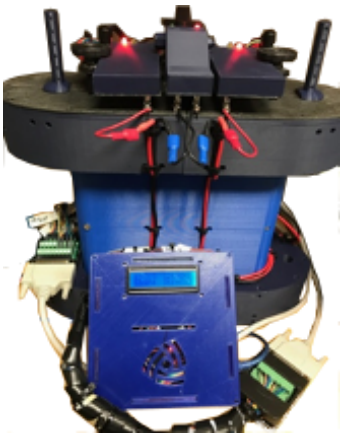

(c) Resistivity Cell

Figure 2.5: Electrodes and Fixture used in metrology systems

a stable and accurate measurement. In addition, for proper insulation and wire flexibility, all electrode connections to the equipment should use a double insulated "Banana" plug connector with a security mask and silicon wire coating.

2.4.1.1 Kelvin Probes

The Kelvin probes are a way to facilitate the measurement of resistivity when using the four-point technique. They are usually shaped like common alligator test probes. But instead of having both halves of the jaw connected at the hinge (electrically common wire for both), they provide an independent wire for each jaw. In this way, the C (current) jaw halves do not go through the P (potential, or voltage) jaw halves, avoiding any voltage drop that could be produced by the length of the wires [31]. Figure 2.6 presents the differences between a normal alligator type of test lead (left) and a Kelvin version (right). While it is completely possible to accomplish a 4-point connection, the position and distance between the pairs of potential and current electrodes are fixed by the jaw hinge.

2.4.1.2 Resistivity Cell

Standard Test Method for D-C Resistance or Conductance of Moderately Conductive Materials, ASTM D4496-13 [13, p. 2], describes the method that applies to the materials that exhibit volume resistivity in the range of 10^0 to $10^7\Omega - cm$ or surface resistivity in the range of 10^3

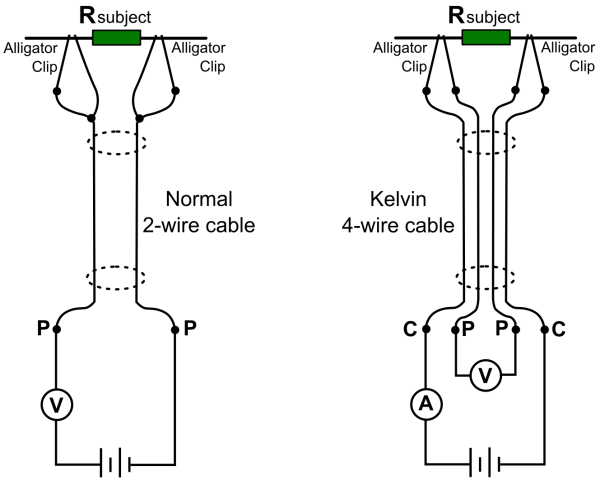

Figure 2.6: Normal (left) and Kelvin (right) type of alligator test probes

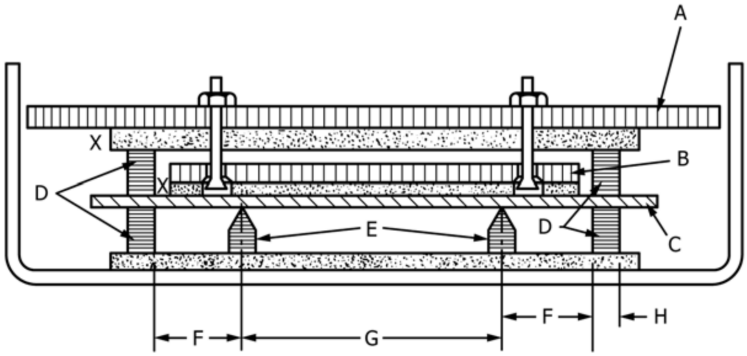

Figure 2.7: Electrode assembly for Resistivity Cell (test cell)[1]

to 10^7 (per square). It also describes a special fixture called "Test Cell", also known as "Resistivity Cell" [13, p. 3], that have been found be satisfactory for measurements in these types of moderately conductive materials. The main purpose of this fixture is to standardize electrode placement and pressure along different operator readings.

The Standard Test Method for D-C Resistance or Conductance of Moderately Conductive Materials, ASTM D4496-13 [13, p. 2] describes the method for materials that exhibit volume resistivity in the range of 10^0 to $10^7\Omega - cm$ or surface resistivity in the range of 10^3 to 10^7 (per square). It also describes a special fixture called "Test Cell", also known as "Resistivity Cell" [13, p. 3]. This Test Cell has been proven satisfactory for measuring moderately conductive materials. The main purpose of this fixture is to standardize the electrode placement and pressure along different operator readings.

Figure 2.7 presents the most important characteristics that form the electrode platform. These are:

A = Mass for applying contact force between current electrodes and the specimen ($300N/m$ times the specimen width in meters). For a specimen $150mm$ wide, mass is approximately $4.5kg$

B = Mass for applying contact force between potential electrodes and the specimen ($60N/m$ times the specimen width in meters). For a specimen $150mm$ wide, mass is approximately $09kg$

C = The specimen

D = Current electrodes

E = Potential electrodes

F = Distance between the current and potential electrodes ($20mm$ minimum)

G = Distance between potential electrodes depends on specimen size

H = Width of current electrode, 5 to $8mm$

X = Electrical insulating material (10 tera Ωcm volume minimum resistivity

Additional descriptions is provided in ASTM D991-89 [1, p. 1] where t is stated:

> "The electrode assembly (Fig. 2.7) shall consist of a rigid base made from an electrical insulating material having a volume resistivity greater than $10T\Omega cm$ (for example, hard rubber, polyethylene, polystyrene, etc.) to which a pair of potential electrodes are fastened in such a manner that the four electrodes are parallel and their top surfaces are in the same horizontal plane. Another pair of current electrodes identical with the first pair shall be fastened to a second piece of insulating material so that they can be superimposed on the specimen directly above the first pair. The current electrodes shall have a length at least $10mm$ greater than the

specimen width, a width between 5 and $8mm$, and a height uniform with $0.05mm$ between 10 and $15mm$. The potential electrodes shall have a length and height equal to the current electrodes, and shall be tapered to an edge having a radius of $0.5mm$ maximum at the top surface. The distance between the potential electrodes shall be not less than $10mm$ nor more than $66mm$ and shall be known within $+2\%$. The current electrodes shall be equidistant outside the potential electrodes by at least 20 mm (0.8 in.). The electrodes shall be made from a corrosion-resistant metal such as brass, nickel, stainless steel, etc. Insulation resistance between electrodes shall be greater than $1T\Omega$"

Chapter 3

Gage Repeatability and Reproducibility Study

Measuring systems could add significant errors to measurements. Therefore, conclusions could be inaccurate and misleading. It is important to assess the accuracy of the measuring system at the start of the study since all conclusions drawn from the statistical methods rely on the accuracy of the measurements. Before any attempt to understand the behavior of ECF materials and to produce useful comparisons between brands and types, a correct way to measure the electric resistance property must be developed and evaluated. The measurement system analysis commonly known as Crossed Gage Repeatability and Reproducibility (Crossed Gage R&R) study is used in this chapter. The purpose of a Crossed Gage R&R study is to determine the sources of variation present in the measurements and it is used for non-destructive testing where the operator measures each part multiple times on each batch [7, 37]. In this chapter, a set of Crossed Gage R&R studies are developed to ensure the correct measurements of the resistivity/resistance of samples of raw ECF material and printed specimens using FDM technology.

3.1 Measuring Systems

A total of ten measurement systems are considered. They cover a wide range of equipment commonly referred in the electrical conductivity literature [8, 9, 10, 11, 12]. Their characteristics are described in Section 2.4. Crossed Gage R&R studies are independently conducted for the ten measurement systems. Each combination of technique, instrument and electrode listed in table 2.2, is accompanied by the proper selection of samples, operators and training according to the way of use of each measurement system. Measuring systems 1 to 4 use standard

manual and automatic handheld multimeter devices with tip point or alligator type of electrodes (two-point resistance measurement technique). Measuring systems 5 and 6 use a benchtop laboratory equipment with the two-point measurement technique and tip point and alligator type of electrodes, respectively. Measuring systems 7 and 8 use the same laboratory equipment but employs the four-point measurement technique. Measuring system 9 and 10 represent a manual setup where the constant current is used for the calculation of resistivity as shown in equation 2.4. In these two systems, an independent equipment measures the voltage and current on the sample. Measuring systems 8 and 10 use the resistivity cell custom fixture. All equipment are calibrated before conducting the experiments and specific instructions are given for the proper use (startup time, reset, and environment conditions). Only non-destructive electrode probes are considered. Figure 2.5 shows the selected electrodes for the experiments.

3.2 Crossed Gage R&R Layouts

Three Crossed Gage R&R studies using different set of samples are conducted for each of the measurement systems listed in table 2.2:

Non-ECF Samples : Correspond to five common elements (non-composite and non-ECF materials) with known resistance values. The purpose is to validate the measurement systems under normal conditions.

Raw-ECF Samples : Correspond to six samples of raw ECF material. Two samples from three ECF manufacturers (Functionalize, Black Magic and PGM3D). The purpose is to assess the capabilities of the measurement systems on ECF materials. This study allows the comparison with manufacturer data.

Printed-ECF Samples : Correspond to six 3D-printed specimen of ECF material using the FDM technology. Two samples from each of the three ECF manufacturers. The purpose is to assess the capabilities of the measurement systems on printed specimens. This study allows the comparison before and after the FDM process.

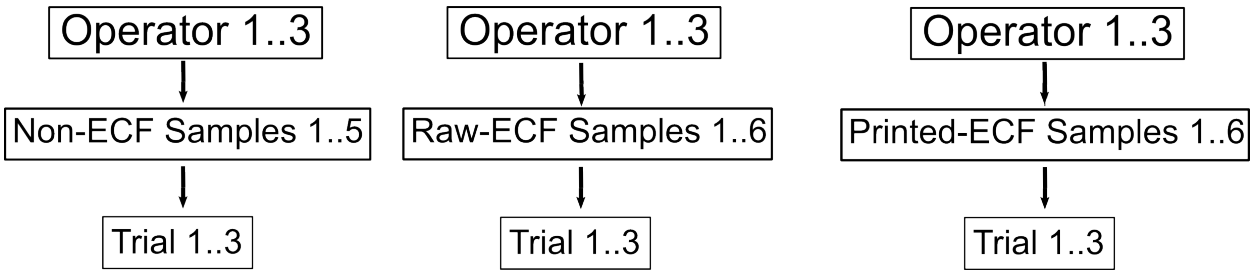

Figure 3.1: Crossed Gage R&R experiment layout for Non-ECF Reference samples (left), Raw-ECF samples (middle) and Printed-ECF Samples (right)

The layouts of the three Crossed Gage R&R experiments conducted over each the measurement systems are shown in Figure 3.1. In the left layout, three operators randomly select three samples from a pool of five Non-ECF samples. Each operator measures the resistance of each sample at three different times. The resistances are previously known and the purpose of this experiment is to ensure that under normal circumstances the measurement systems perform with high repeatability and reproducibility. In the middle layout, the same three operators measure specimens randomly selected from a pool of six raw-ECF material specimens. Similarly, each operator measures the specimens at three different times. In the right layout, the process is similar but using the printed-ECF specimens. The results of these experiments allow for the selection of the most suitable measurement system and the comparison before and after the FDM process. A total of thirty independent Crossed Gage R&R experiments are conducted.

3.2.1 Source of Variation

In the Crossed Gage R&R experiment, the sources of variation of the response variable are grouped into three categories [38]:

- Variation due to different operators (reproducibility)
- Variation due to the measuring/measurement system (repeatability)
- Variation due to the parts

These three components of variation compose the total process variance σ^2, calculated by equation 3.1:

$$\sigma^2 = \sigma_p^2 + \sigma_o^2 + \sigma_{ms}^2 \tag{3.1}$$

Where σ_p^2 is the part variance; σ_o^2 is the operator variance (reproducibility) and σ_{ms}^2 is the measurement system variance (repeatability).

We are interested in the repeatability of the measuring system. Repeatability is the capacity of the measuring system to obtain the same measurements on the same sample under identical conditions.

3.3 Test Samples

As specified in Section 3.2, there are three types of samples: Reference Samples, Raw ECF Samples and FDM Printed ECF Samples. Each set is used to ensure the suitability of the measurement systems under different scenarios.

There are three types of samples. There are Non-ECF, Raw-ECF and Printed-ECF samples. Figure 3.2 illustrates the shape and dimensions.

3.3.1 Non-ECF Samples

Five samples of non-ECF materials are used to ensure the measurement systems operate to equipment specifications. These samples are non-composite materials with known resistance. They cover the range of expected values of raw and printed ECF specimens. The five samples are referred as $RV1 - RV5$. Table 3.1 lists the values arbitrarily assigned:

Sample	**Element**	**Value** (Ω)
RV1	Electronic Resistance	1000
RV2	Bronze Extrusion $5x10x100mm$	0.05
RV3	Electronic Resistance	2000
RV4	Cooper Sheet $0.3x5x100mm$	0.06
RV5	Electronic Resistance	220

Table 3.1: Non-ECF Samples

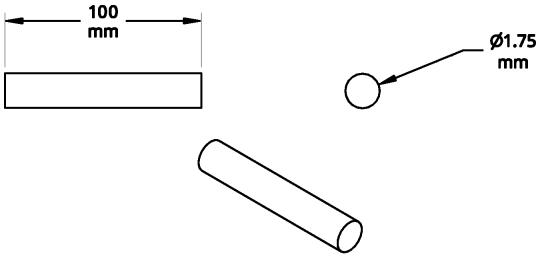

(a) Raw-ECF filament specimen dimensions

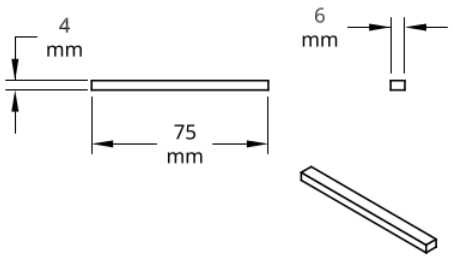

(b) Printed-ECF specimen dimensions

Figure 3.2: Raw-ECF and Printed-ECF specimens

3.3.2 Raw-ECF Specimens

Three manufacturers of ECF material Functionalize, Black Magic and PGM3D are chosen. Six specimens of raw filament, two specimens for each manufacturer, are obtained. One specimen is from the first half of the roll and the second specimen is from the second half. The six specimens are referred as $RS1 - RS6$ and they are shown in table 3.2. Figure 3.2a shows the dimension of the specimens.

Specimen	Material	Code	Roll Section
RS1	PMG3D GPLA-C/Z2W ZY	PG-S2	2nd half
RS2	Functionalize F-Electric	FF-S2	2nd half
RS3	PMG3D GPLA-C/Z2W ZY	PG-S1	1st half
RS4	Black Magic Graphene PLA	BG-S1	1st half
RS5	Black Magic Graphene PLA	BG-S2	2nd half
RS6	Functionalize F-Electric	FF-S1	1st half

Table 3.2: Raw-ECF specimens

3.3.3 Printed-ECF Samples

The standard ASTM B193-16 [39, p. 2] defines the test specimen with a length of at least $300mm$. Due to printing size limitations, the test specimens are downsized to a quarter of the suggested length, $75x6x4mm(long, width, height)$. Figure 3.2b presents the dimension of the printed specimens. Six specimens are randomly selected from a pool of samples from the three selected ECF manufacturers, two per manufacturer. One specimen is from the first half of the

roll and the second sample from the second half. The printing parameters are given in table 4.1. The six specimens are referred as $PS1 - PS6$ and shown in table 1.3. Details about the 3D printing process and environment conditions for the ECF specimens are given in 4.1, 4.2.1 and 4.2.

Specimen	Material	Code	Roll Section
PS1	Black Magic Graphene PLA	BG-SH3-I100-PR-OH-S1	1st half
PS2	PMG3D GPLA-C/Z2W ZY	PG-SH3-I100-PR-OH-S1	1st half
PS3	Black Magic Graphene PLA	BG-SH3-I100-PR-OH-S2	2nd half
PS4	Functionalize F-Electric	FF-SH3-I100-PR-OH-S1	1st half
PS5	PMG3D GPLA-C/Z2W ZY	PG-SH3-I100-PR-OH-S2	2nd half
PS6	Functionalize F-Electric	FF-SH3-I100-PR-OH-S2	2nd half

Table 3.3: Printed-ECF specimens

As described in [40, p. 2], prior to testing, the specimen must reach an equilibrium condition in a standard laboratory atmosphere. Most materials require less than $24h$. Equilibrium under standard laboratory conditions is obtained if two consecutive volume resistance measurements on the same specimen are within $\pm 1\%$. The two consecutive measurements are taken with an interval of at least $4h$. Using the ASTM 618-13 nomenclature, conditioning of the test specimens is designated as:

Condition 96/24/40.

Which means $96h$, at $24°C$ and 40% relative humidity.

3.4 Operators

Three operators are arbitrary selected and trained in the use of each individual measurement system. Printed material is provided and on-site training sessions scheduled, ensuring that each operator fully understands the procedure of correct electrode positioning and equipment readings. During measurements, the operators used visual aids to check the correct steps involved. Operators used nitrile gloves at all times.

Literature and user manuals for electronic measurement equipment [8, 9, 32, 35], indicate the importance of electrode placement and pressure, and the recommended maximum time per reading. Variations in these factors can introduce significant noise on the readings. Precautions were taken in each measurement system to firmly attach the electrodes to the specimen and at the same location on each reading within a maximum of one minute.

The operator placed the sample under the electrodes of the equipment, set the electrodes at the same location in each reading, and applied the same pressure perpendicular in the case of tip point electrodes. The operator set the proper mode of the equipment and enabled the reading. While reading, the operator checks a visual timer to not exceed sixty seconds. During this time, the operator obtains the most stable reading by pressing the hold function on the instrument to retain the reading on the screen. For the measurement systems 8 and 10, a custom software was written in C lenguage, using the "Standard Commands for Programmable Instruments" (SCPI). Using a computer, the operator can enable all equipment at once to hold the reading at the different screens simultaneously so to obtain accurate readings. The procedure used by the operators is explained in Section 3.2.

3.5 Resistivity Cell

The standard ASTM D4496-13 describes a special fixture called "Test Cell", also known as "Resistivity Cell" [13, p. 3]. The Test Cell has been satisfactory used for measuring conductance of moderately conductive materials. The main purpose of the fixture is to standardize the placement and pressure of the electrodes when using the four-point technique. In this research, a custom resistivity cell has been designed and built using two vises manufactured by "PanaVise" [41, 42]. The vises pressure the specimen on a surface. Two PanaVise 366 vises support the two current electrodes, while a smaller PanaVise Body Jr 207 supports the two voltage electrodes. The reason to choose a smaller size for the voltage electrodes is that according to ASTM D4496-13 the force applied to the voltage electrodes is considerably lower than for the current electrodes.

Figure 3.3 presents the overall design of the resistivity cell and figure 3.4 shows an exploded view of the fixture. For insulation, the PLA and TPU are selected since they present a

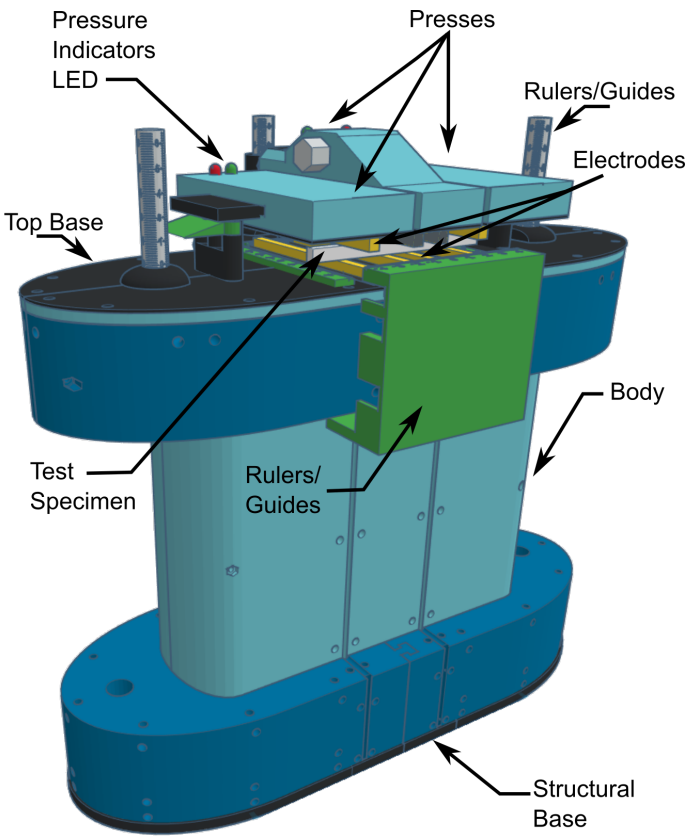

Figure 3.3: Resistivity Cell

.

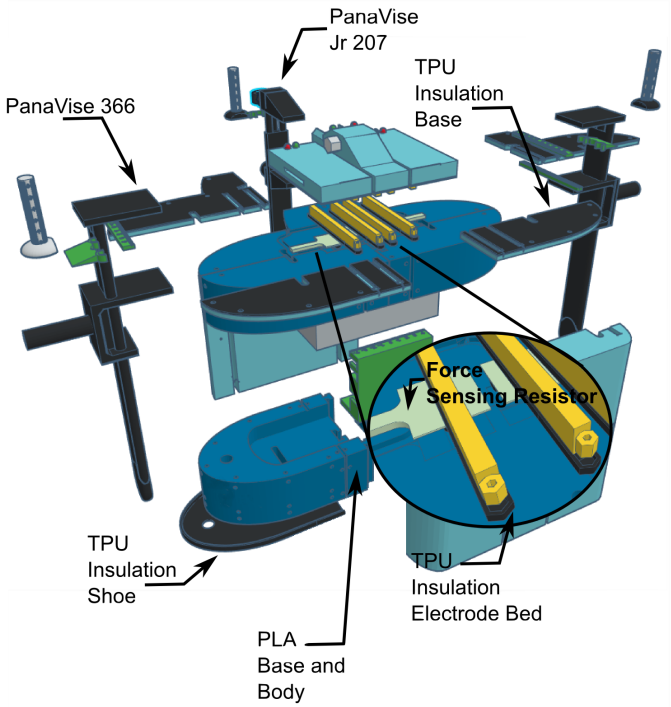

Figure 3.4: Resistivity Cell explode view

.

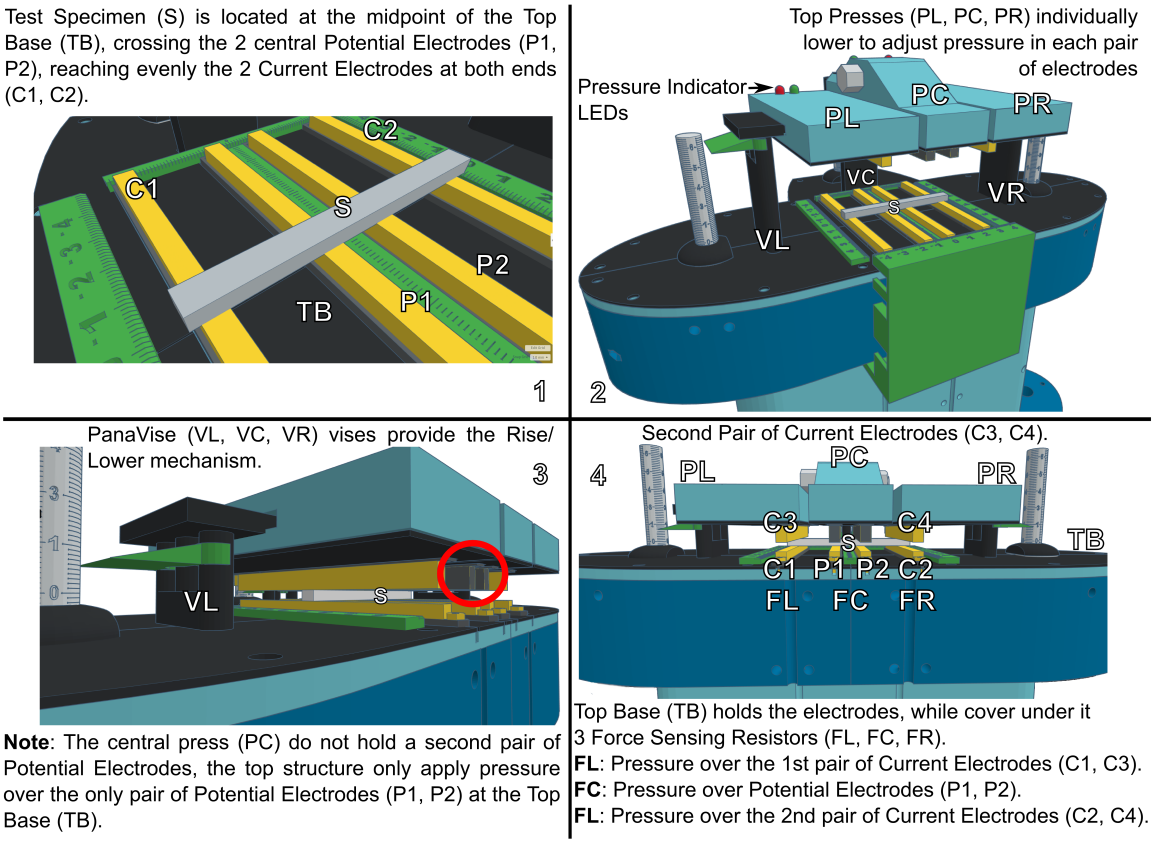

Figure 3.5: Resistivity Cell use procedure

.

resistivity of $10^{16}\Omega m$ [43] and between $10^{7}\Omega m$ and $10^{15}\Omega m$ [44], respectively. Both materials meet the ATSM D4991-89 specification for insulation levels. All parts are printed using the standard PLA and TPU parameters which are already included in the slicer software. All parts are printed 100% infill. According to the electrode layout and dimensions described in [1], one pair of voltage electrodes is located at the center and two pairs of current electrodes are located at each side of the top base of the fixture. Two presses, one in each side, align the second pair of current electrodes. The middle press only applies pressure to the pair of voltage electrodes on the center of the top base. The voltage electrodes are tampered according to the description provided.

Figure 3.5, the procedure for setting up the test specimen and the electrodes is explained. In step 1, the test specimen is centered on the top base. In steps 2 and 3, the vises are used to raise or lower the top presses. Once all electrodes have been correctly aligned, the pressure is adjusted until the force sensors under the electrodes read the recommended pressure [13, p. 3],

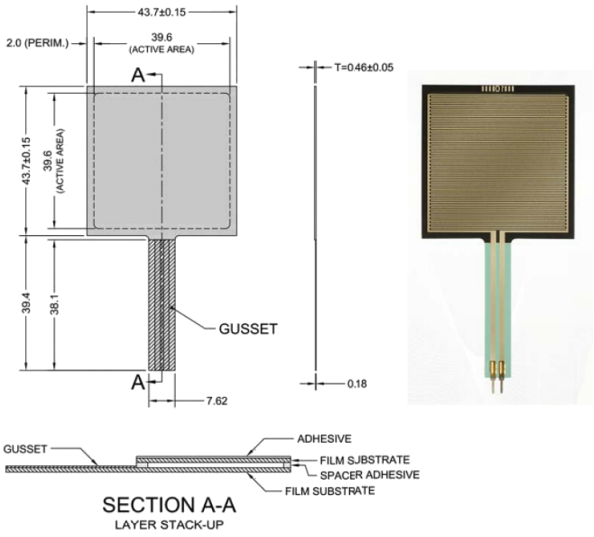

Figure 3.6: Force Sensing Resistor (FSR) model 406 [2]

.

indicated by turning on the green LED. If the pressure is over 10% of the recommended value, the red LED turns on. If the pressure is under 10% of the recommended value, no LED is on. All three LEDs must be green to take a measurement.

The sensor chosen was a FSR 406 of the Interlink Electronics company [2]. Figure 3.6 shows the main dimensions. Important characteristics of the sensor are:

The pressure sensor Interlink Electronics FSR 406 was used [2]. Figure 3.6 shows its dimensions. Important characteristics of the sensor are:

- Actuation Force ˜0.2Nmin
- Force Sensitivity Range ˜0.2N - 20N
- Force Resolution Continuous (analog)
- Force Repeatability Part to Part $\pm 6\%$ (Single Batch)
- Non-Actuated Resistance $> 10M\Omega$
- Hysteresis $+10\%$ Average
- Device Rise Time < 3 Microseconds

- Long Term Drift $1kg$ load, 35 days $< 5\%$

The Resistivity Cell includes a TPU rubber cushion pad under the sensor to allow for flexion when the electrodes are pushed down by the upper press. The amplified zone in Figure 3.4 shows the location of these sensors. Since there is a single pair of voltage electrodes at the center of the top base, only one sensor is required to measure the total load over this electrode pair. Two other separated pairs of current electrodes are located at each side of the central press. In addition, two independent sensors are located left and right for each pair of the potential electrodes. The design allows a maximum size of the specimen of $75x150x35mm$ (w, l, h).

3.5.1 Resistivity Cell - Micro-controller

An Arduino Mega 2560 micro-controlled [45] is programed to control, read, check the thresholds of the amount of pressure over the sensors. When the pressure is within the threshold range, a green LED is turned on. When the pressure is over the range a red LED is turned on and the green LED is turned off. When the pressure is below the range, no LED is on. Figure 3.7 shows the complete electronic diagram of the pressure cell micro-controller and the LCD display.

To calibrate the resistivity cell, two known weights are used, $2.25kg$ for the current electrodes and $0.5kg$ for the voltage electrode pair. Since the test specimens ($RV1 - RV5$ $RS1 - RS6$, $PS1 - PS6$) are half their recommended dimensions [13, p. 3], half of the weight is used. After three consecutive readings, the mean of each sensor is calculated. The mean $\pm 10\%$ is used as the threshold range. This way, the adjustable presses at the center and at each side trigger the acceptable range notification when the pressure applied over the specimen is equivalent to the known weights.

List 3.1 presents the pseudo-code in Arduino Sketch language for the resistivity cell micro-controller algorithm.

Listing 3.1: Resistivity Cell Micro-controller Pseudo-Code

```
void loop() {
  //For each pressure sensor (3)
  for (int i=0; i < PSENSORS; i++){
    analog[i].update(); //Update last value from hardware
```

```
    potvalue[i] = analog[i].getValue(); //Move value to local variable
    //Filter data...
    //Calculate if the current value is greater to the normal drift of
    //the sensor, it will filter smaller variation from the sensor.
        difftmp = potvalue[i] - curvalue[i];
    if (abs(difftmp) > diffvalue[i]) {
      force[i] = potvalue[i];} //Force value is updated...
    curvalue[i] = potvalue[i];

    //Check if the value is in range, if Ok it turn ON the Gren LED
    //and OFF the Red one.
    if ((minPressure[i] <= force[i]) && (maxPressure[i] > force[i])) {
      digitalWrite(psRedLED[i], LOW);    //Correct pressure, Red LED OFF,
      digitalWrite(psGreenLED[i], HIGH); //Green LED ON
    } else if (minPressure[i] > force[i]) {
      digitalWrite(psRedLED[i], LOW);    //Under-pressure,
      digitalWrite(psGreenLED[i], LOW);  //both LEDs OFF
    } else if (maxPressure[i] <= force[i]) {
      digitalWrite(psRedLED[i], HIGH);   //Over-pressure, Red LED ON,
      digitalWrite(psGreenLED[i], LOW);  //Green LED OFF
    }
  }
  //Display data and status in LCD screen and send it through serial port
}
```

3.6 Statistical Analyses

The analysis of variance (ANOVA) of the crossed Gage R&R experiments is conducted using the Minitab 18 software [46]. The statistical studies include Non-ECF, Raw-ECF and Printed-ECF specimens. The response variable is resistivity and resistance. Several charts are used:

- Component of Variation Chart: Graphically represents the resulting Crossed Gage R&R ANOVA results. Each cluster of bars represents a source of variation. In a suitable measurement system, the largest component of variation is expected to be the part-to-part variation. The repeatability factor represents the variability of the equipment (gage) and the reproducibility factor represents the variability of the operators.

- R Chart: Graphically displays operator consistency. If the operators measure consistently, the ranges would be small relative to the measurements.

- Xbar Chart: Compares the part-to-part variation to the repeatability component.

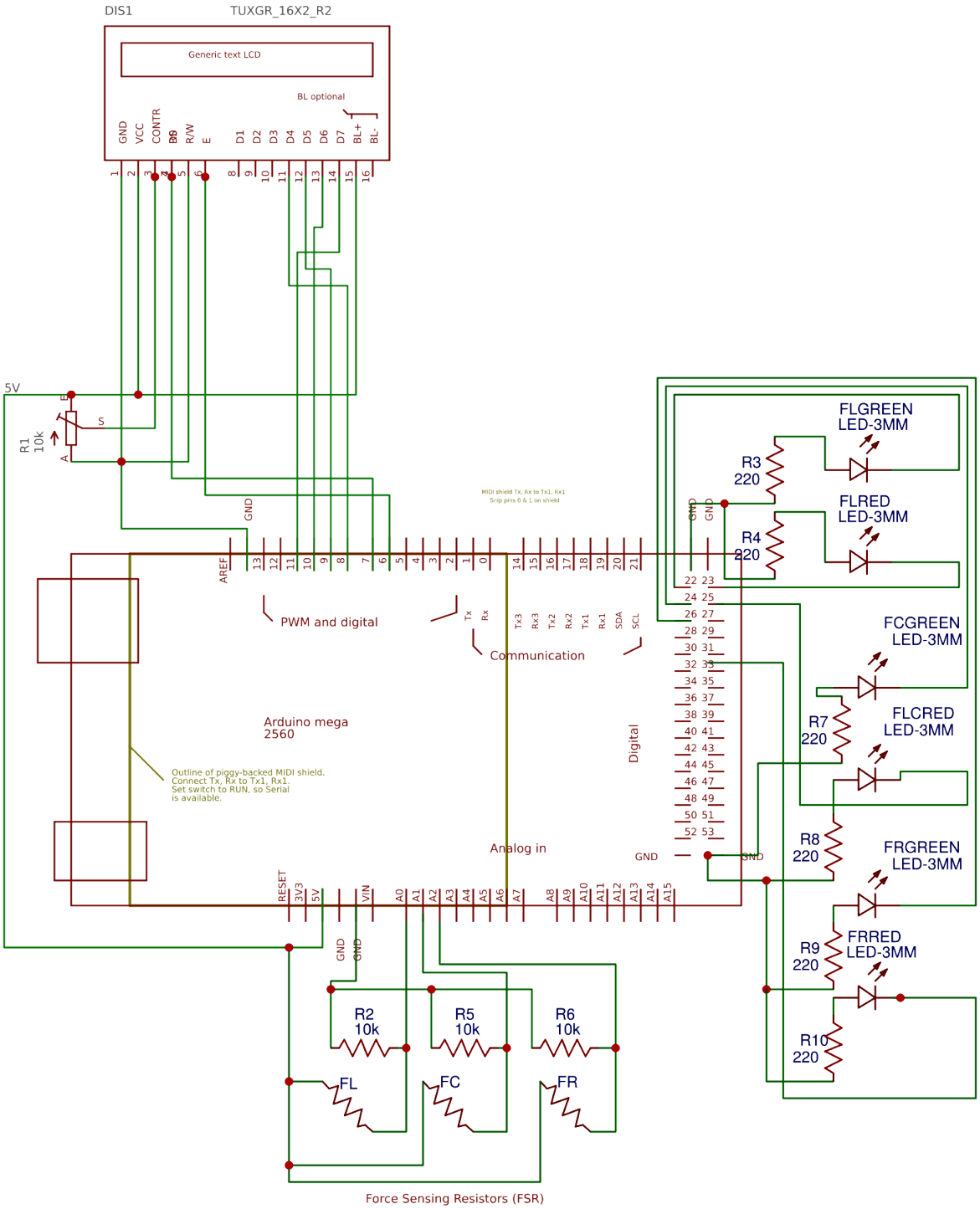

Figure 3.7: Resistivity Cell electronic schematic

.

- By Operator Chart: The By Operator chart helps to determine whether the measurements and variability are consistent across operators.

3.7 Results

Ten independent Crossed Gage R&R experiments, each representing a measurement system (see Table 2.2), are conducted using five Non-ECF ($RV1 - RV5$), six Raw-ECF ($RS1 - RS6$) and six Printed-ECF ($PS1 - PS6$) specimens. The Crossed Gage R&R experiments, using the Non-ECF samples, ensures the correct functioning of the measurement system and the correct training of the operators. The experiments that use the raw material specimens help to compare measured data with information provided by the manufacturers. Finally, the experiments using the printed samples provide useful information about the behavior of the material after the FDM process.

3.7.1 Crossed Gage R&R using Non-ECF Specimens

Figures 3.8, 3.9 and 3.10 present a summary of the ten Crossed Gage R&R experiments using the Non-ECF samples. The source of variation is displayed in the X axis and the percentage variation in the Y axis. The interaction term was removed with confidence level $\alpha = 0.05$. Each measurement system shows two bars corresponding to the percentage Contribution and StudyVar. The bar graphs are grouped by the resistance measuring technique and type of electrodes. Figure 3.8 shows the three measurement systems where the two-point resistivity/resistance measuring technique and tip point electrodes are used. Figure 3.9 presents the next three measurement systems where the two-point measuring technique and alligator electrodes are used. Figure 3.10 includes the last four measurement systems, where a four-point resistivity/resistance measuring technique is used with alligator electrodes or the custom pressure cell fixture. A summary of the Part-to-Part contributions for each measurement system are shown in Table 3.4.

Table 3.4 presents the measurement systems tested with Non-ECF samples. We can observe that all measurement systems have a Part-to-Part percentage contribution of 99.97% or higher. Meaning that the other factors, repeatability and reproducibility, account for no more

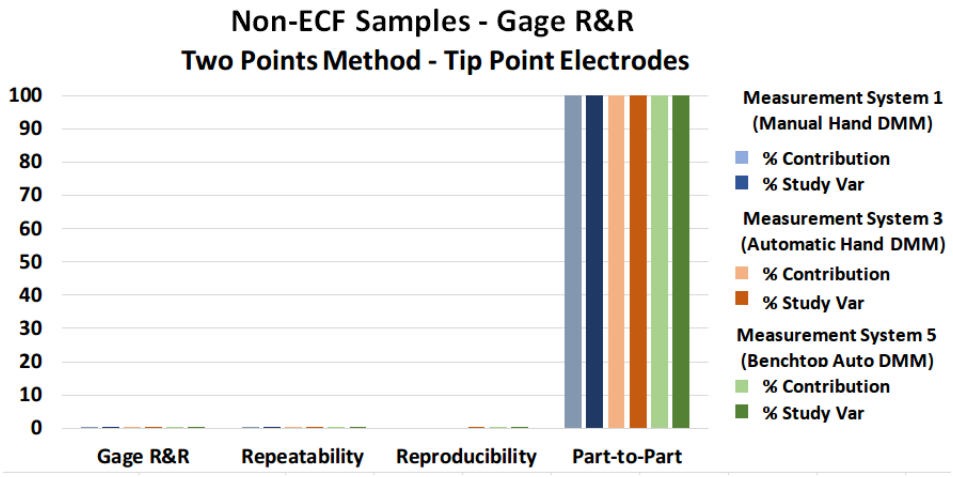

Figure 3.8: Two Points Methods - Tip Point Electrodes. Crossed Gage R&R components of variation, Non-ECF samples

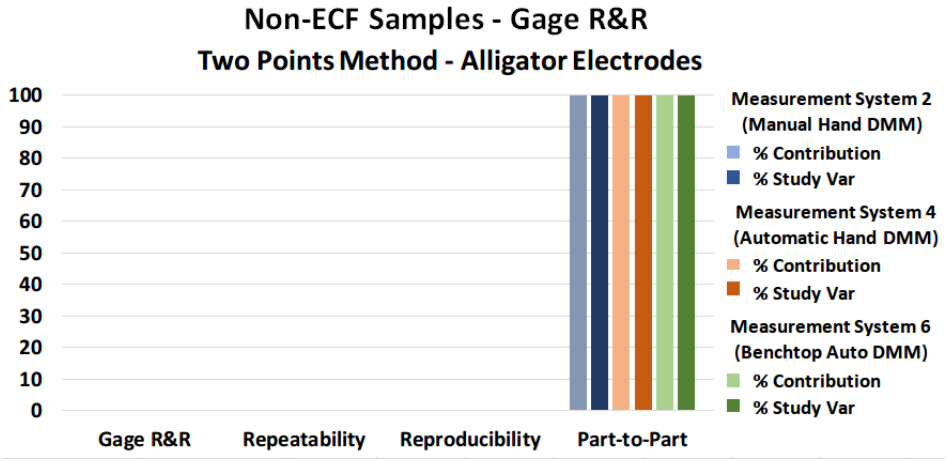

Figure 3.9: Two Points Methods - Alligator Electrodes. Crossed Gage R&R components of variation, Non-ECF samples

Measuring System	Technique	Equipment	Electrodes/Fixture	Part-to-Part %Contribution
1	Two-Points	Manual Handheld Multimeter	Tip Probe	99.97
4	Two-Points	Automatic Handheld Multimeter	Alligator clip test lead	99.97
2	Two-Points	Manual Handheld Multimeter	Alligator clip test lead	99.98
3	Two-Points	Automatic Handheld Multimeter	Tip Probe	99.98
5	Two-Points	Benchtop Digital Multimeter	Tip Probe	99.99
6	Two-Points	Benchtop Digital Multimeter	Alligator clip test lead	99.99
7	Four-Points	Benchtop Digital Multimeter	Alligator clip test lead	99.99
8	Four-Points	Benchtop Digital Multimeter	Resistivity Cell	99.99
9	Four-Points	Constant Current	Alligator clip test lead	99.99
10	Four-Points	Constant Current	Resistivity Cell	99.99

Table 3.4: Part-to-Part contribution for Non-ECF samples

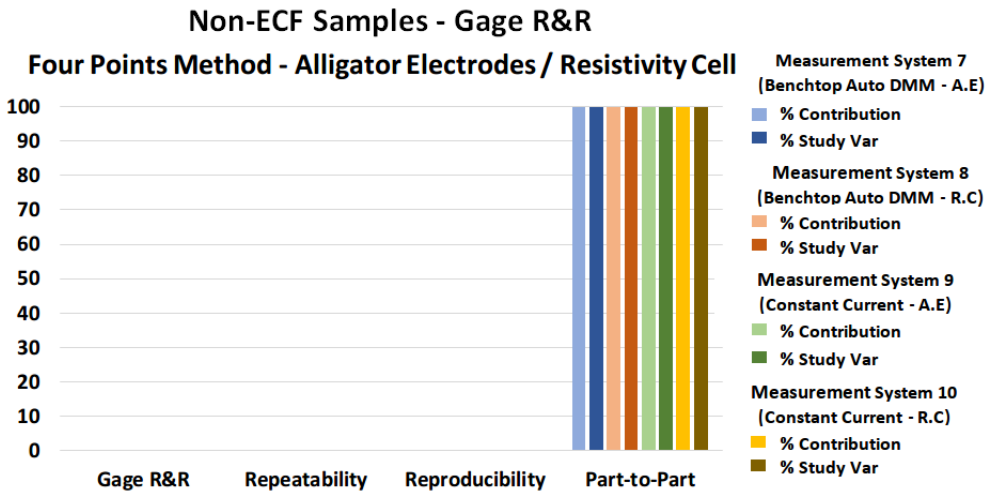

Figure 3.10: Four Points Methods - Alligator Probes/Resistivity Cell. Crossed Gage R&R components of variation, Non-ECF samples

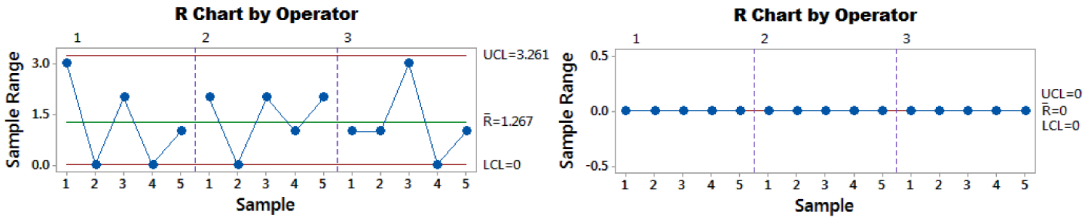

Figure 3.11: R-Chart for Non-ECF samples, worse on the left (measurement system 1), best on the right (measurement system 10)

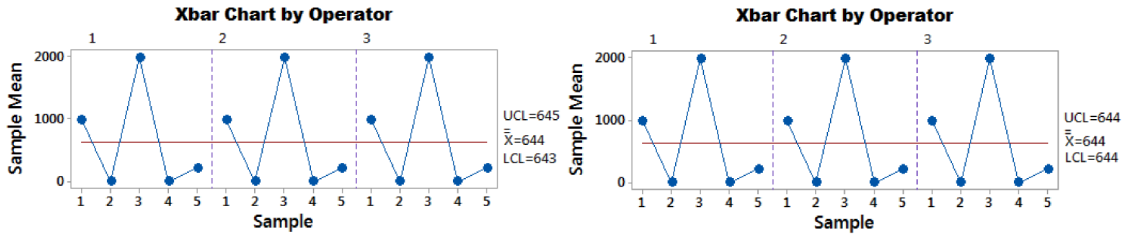

Figure 3.12: X-Chart for Non-ECF samples, worse on the left (measurement system 1), best on the right (measurement system 10)

.

than a 0.03% of the system variation. These results indicate of a consistent setup system and operators.

Figure 3.11 presents the R-Chart for the worst (left) and best (right) measurement systems for Non-ECF samples (measurement system 1 and 10 respectively). Plotted points represent, for each operator, the difference between the largest and smallest measurements of each part. If the measurements are the same, then $range = 0$ (right case). Both R-Charts for Non-ECF samples (fig. 3.11) show that operator measurements fall inside the upper and lower control limits (UCL and LCL respectively), meaning that the operators are consistently measuring the parts. In both cases, the measurements are close to the center line (grand average of the ranges).

Figure 3.12 presents the X-Chart for the worst (left) and best (right) measurement systems for Non-ECF samples (measurement system 1 and 10 respectively). Plotted points represent the average measurement of each part for each operator. Center line is the overall average for all part measurements by all operators. Control limits (UCL and LCL) are based on the number of measurements in each average and the repeatability estimate. It is desirable to observe more variation between part averages than what is expected from repeatability variations alone. In both X-Charts of the Non-ECF samples (fig. 3.12) we can see that many points are above or below the control limits. These results indicate that the part-to-part variation is much greater than the measurement device variation.

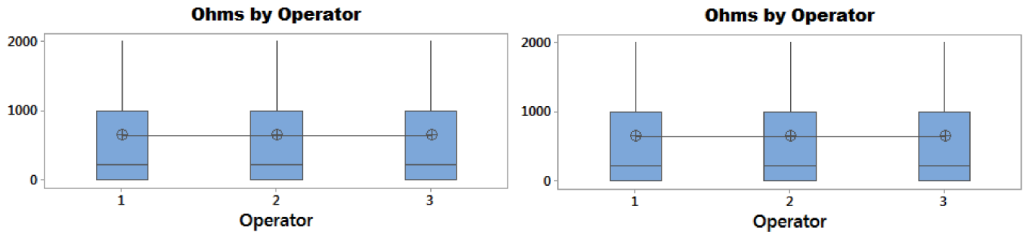

Figure 3.13: Ohms by operator for Non-ECF samples, worse on the left (measurement system 1), best on the right (measurement system 10)

.

Figure 3.13 presents the "Measurement by operator" plot for the worst (left) and best (right) measurement systems for Non-ECF samples (measurement system 1 and 10 respectively). The Ohms by operator graph shows all of the study measurements, arranged by operator. Parallel lines mean that operators obtain the same measurements on average. The box plots do not present spread in the measurements of the Non-ECF samples.

3.7.2 Crossed Gage R&R using Raw-ECF Specimens

Figures 3.14, 3.15 and 3.16 present a summary of the ten Gage R&R experiments performed using the six raw ECF samples. Each source of variation is displayed in X axis. The Y axis presents the percentage amount of variation for that factor. The interaction term is removed with $\alpha = 0.05$. Each measurement system has two bars that corresponds to percentage Contribution and StudyVar. The bar graphs are grouped by the resistance measuring technique and electrodes. Figure 3.14 shows the three measurement systems where the two-point resistivity/resistance measuring technique is used, along with tip point electrodes. Figure 3.15 presents the next three measurement systems where alligator electrodes are used with the two-point measuring technique. Figure 3.16 includes the last four measurement systems, where a four- point resistivity/resistance measuring technique and alligator electrodes or the custom pressure cell are used. In each measurement system (Table 2.2) a different type of equipment and electrodes (gage) are used.

A summary of the Part-to-Part contributions for each measurement system can be found in Table 3.5

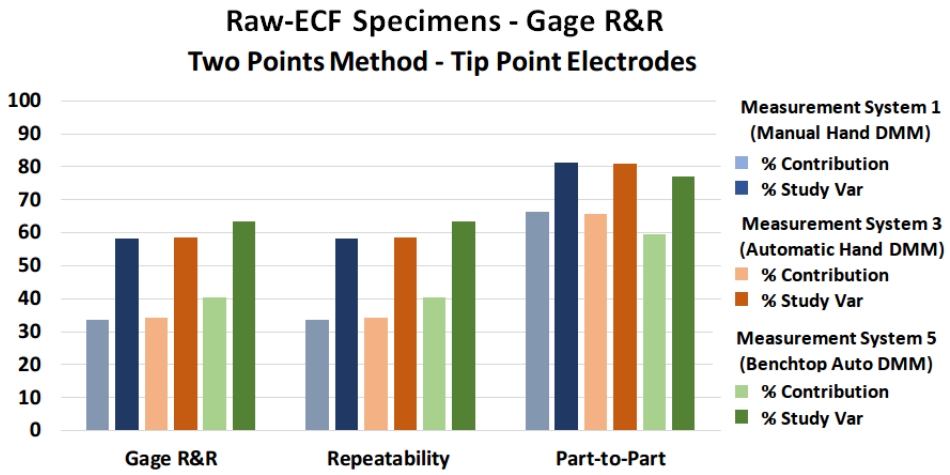

Figure 3.14: Two Points Methods - Tip Point Electrodes. Crossed Gage R&R components of variation, Raw-ECF specimens

.

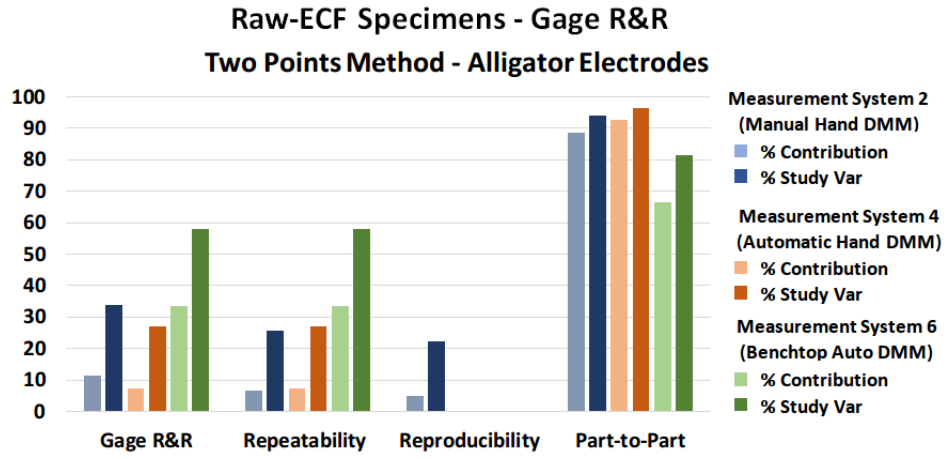

Figure 3.15: Two Points Methods - Alligator Electrodes. Crossed Gage R&R components of variation, Raw-ECF specimens

.

Measuring System	Technique	Equipment	Electrodes/Fixture	Part-to-Part %Contribution
5	Two-Points	Benchtop Digital Multimeter	Tip Probe	59.56
3	Two-Points	Automatic Handheld Multimeter	Tip Probe	65.69
1	Two-Points	Manual Handheld Multimeter	Tip Probe	66.25
6	Two-Points	Benchtop Digital Multimeter	Alligator clip test lead	66.55
2	Two-Points	Manual Handheld Multimeter	Alligator clip test lead	88.47
4	Two-Points	Automatic Handheld Multimeter	Alligator clip test lead	92.65
9	Four-Points	Constant Current	Alligator clip test lead	97.05
10	Four-Points	Constant Current	Resistivity Cell	98.10
7	Four-Points	Benchtop Digital Multimeter	Alligator clip test lead	99.25
8	Four-Points	Benchtop Digital Multimeter	Resistivity Cell	99.45

Table 3.5: Part-to-Part contribution for Raw-ECF specimens

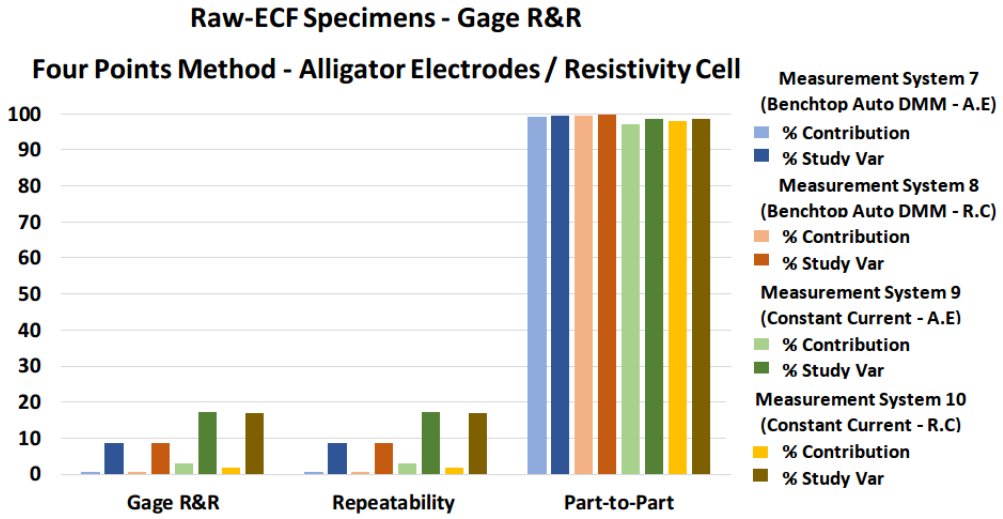

Figure 3.16: Four Points Methods - Alligator Probes/Resistivity Cell. Crossed Gage R&R components of variation, Raw-ECF specimens

.

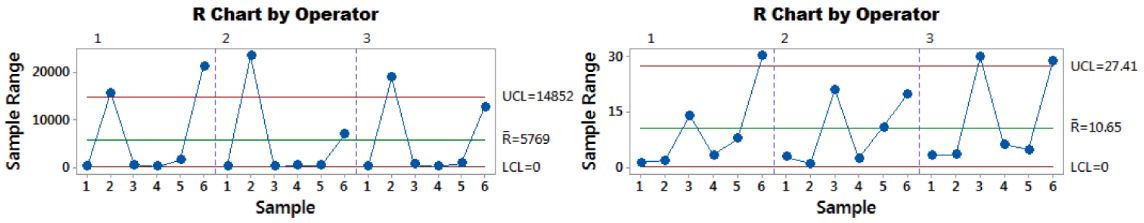

Figure 3.17: R-Chart for Raw-ECF specimens, worse on the left (measurement system 5), best on the right (measurement system 8)

.

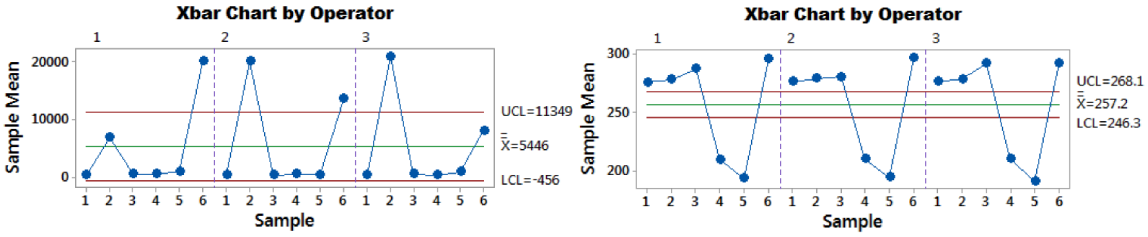

Figure 3.18: X-Chart for Raw-ECF specimens, worse on the left (measurement system 5), best on the right (measurement system 8)

.

Table 3.5 shows that the best results for ECF raw material samples correspond to measurement system 8 (four-points, benchtop digital multimeter and pressure cell fixture), with a Part-to-Part percentage contribution of 99.45%. Measuring system 5 (two-points, benchtop digital multimeter and tip probe electrodes) with a Part-to-Part percentage contribution of 59.56% is the one with the lower results. Notice that the measurement systems with higher variability in the Part-to-Part factor are the last four systems that use a four-point measuring technique. Measuring system 4 is the only that use a two-point measuring technique that produces a relatively high variability on the Part-to-Part factor of 92.65%.

Figure 3.17 presents the R-Chart for the worst (left) and best (right) measurement systems for the raw ECF samples (measurement system 5 and 8 respectively). Plotted points represent, for each operator, the difference between the largest and smallest measurements of each part.

Left R-Chart for ECF raw material samples (fig. 3.17) presents a big range between the LCL and the UCL control limits, an indication of high variability due to the gage (repeatability factor). On the right chart, we observe that the values fall into a more close range and the measurements are closer to the central line, an indication of a higher influence of the Part-to-Part factor.

Figure 3.18 presents the X-Chart for the worst (left) and best (right) measurement systems for raw ECF samples (measurement system 5 and 8 respectively). Plotted points represent the average measurement of each part for each operator. The center line is the overall average for all part measurements and by all operators. Control limits UCL and LCL are based on the number of measurements on each average and the repeatability estimate. It is desirable to observe more variation between part averages than what is expected from repeatability variation alone. In the

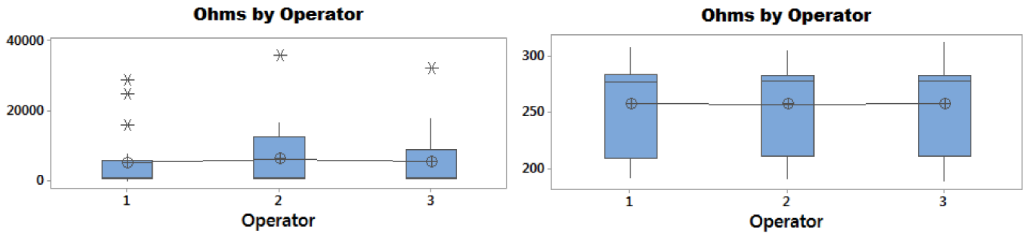

Figure 3.19: Ohms by operator for Raw-ECF specimens, worse on the left (measurement system 5), best on the right (measurement system 8)

.

left X-Chart for the raw ECF samples (3.18) we observe that most measurements fall inside the upper and lower control limits (UCL and LCL), meaning that the variability of the system (gage) do not allow correct differentiation from the part-to-part variation factor (measurement system 5). On the contrary, the plot on the right shows that most of the measurements fall outside upper and lower limits, an indication that the that part-to-part variation is much greater than the measurement device variation (measurement system 8).

Figure 3.19 presents the "Measurement by operator" plot for the worst (left) and best (right) measurement systems for raw ECF samples (measurement system 5 and 8 respectively). The Ohms by operator graph shows all of the study measurements, arranged by operator. Box plots show that on average the operators are measuring the parts similarly (measurement system 8). They also show that there is no spread in the measurements 3.19. The left side of figure 3.19 presents the worse-case (measurement system 5), where important difference between mean by different operators are presented as non-parallel connecting lines between the box.

3.7.3 Crossed Gage R&R using Printed-ECF Specimens

Figure 3.20, 3.21 and 3.22, present a summary of the 10 Gage R&R experiments performed using the six printed ECF samples. Each source of variation is displayed in X axis. The Y axis presents the percentage amount of variation for that factor. The interaction term is removed with $\alpha = 0.05$. Each measurement system has two bars that corresponds to percentage Contribution and StudyVar.

The bar graphs are grouped by the resistance measuring technique and type of electrodes. Figure 3.20 shows the three measurement systems, where the two-point resistivity/resistance

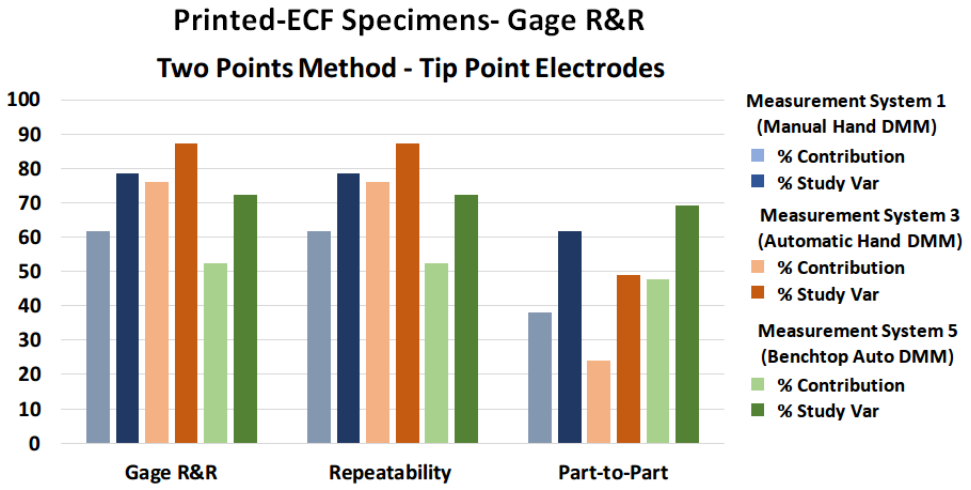

Figure 3.20: Two Points Methods - Tip Point Electrodes. Crossed Gage R&R components of variation, Printed-ECF specimens

.

Measuring System	Technique	Equipment	Electrodes/Fixture	Part-to-Part %Contribution
3	Two-Points	Automatic Handheld Multimeter	Tip Probe	24.06
1	Two-Points	Manual Handheld Multimeter	Tip Probe	38.15
5	Two-Points	Benchtop Digital Multimeter	Tip Probe	47.68
2	Two-Points	Manual Handheld Multimeter	Alligator clip test lead	60.77
6	Two-Points	Benchtop Digital Multimeter	Alligator clip test lead	69.87
4	Two-Points	Automatic Handheld Multimeter	Alligator clip test lead	86.05
9	Four-Points	Constant Current	Alligator clip test lead	96.91
10	Four-Points	Constant Current	Resistivity Cell	98.30
7	Four-Points	Benchtop Digital Multimeter	Alligator clip test lead	98.93
8	Four-Points	Benchtop Digital Multimeter	Resistivity Cell	98.98

Table 3.6: Part-to-Part contribution for Printed-ECF specimens

measuring technique is used, along with tip point electrodes. Figure 3.21 presents the next three measurement systems where alligator electrodes are used with the two-point measuring technique. Figure 3.22 includes the last four measurement systems under test, where a four-point resistivity/resistance measuring technique and alligator electrodes or the custom pressure cell are used. In each measurement system a different type of equipment and electrodes are used.

A summary of the Part-to-Part contributions for each measurement system are shown in Table 3.6.

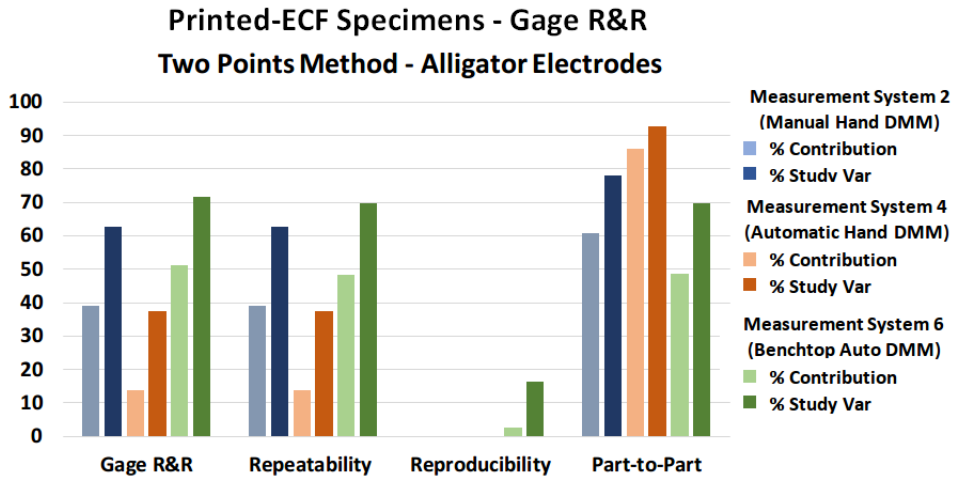

Figure 3.21: Two Points Methods - Alligator Electrodes. Crossed Gage R&R components of variation, Printed-ECF specimens

.

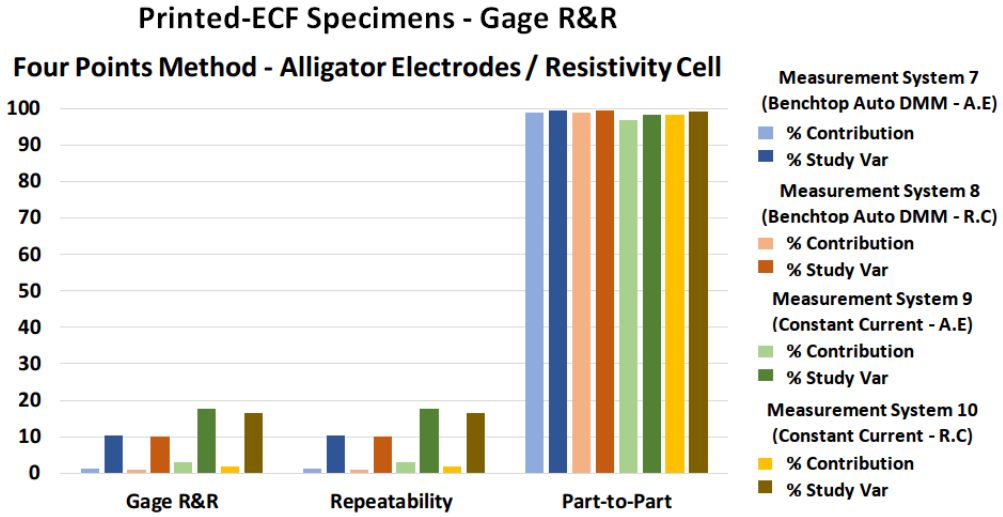

Figure 3.22: Four Points Methods - Alligator Probes/Resistivity Cell. Crossed Gage R&R components of variation, Printed-ECF specimens

.

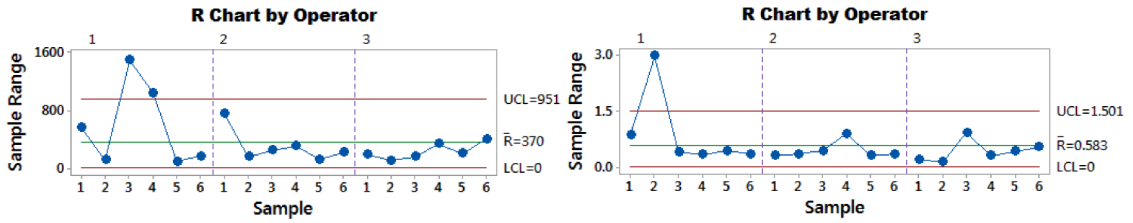

Figure 3.23: R-Chart for Printed-ECF specimens, worse on the left (measurement system 3), best on the right (measurement system 8)

.

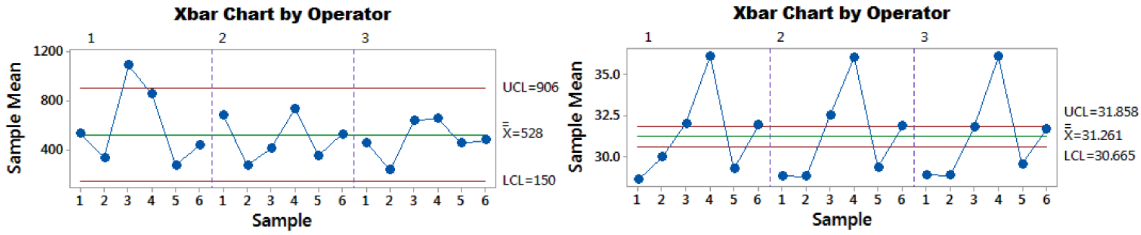

Figure 3.24: X-Chart for Printed-ECF specimens, worse on the left (measurement system 3), best on the right (measurement system 8)

.

Table 3.6 shows that the best results for ECF printed specimens correspond to measurement system 8, width a Part-to-Part percentage contribution of 99.98%. Measuring system 3, width a Part-to-Part percentage contribution of 24.06% is the one with the lower results. Notice that the measurement systems with higher variability in the Part-to-Part factor are the last four systems that use a four-point measuring technique. These four measurement systems are the same with higher percentage contribution in the part-to-part factor for the raw ECF samples.

Figure 3.23 presents the R-Chart for the worst (left) and best (right) measurement systems for the printed ECF samples (measurement system 3 and 8 respectively). Plotted points represent, for each operator, the difference between the largest and smallest measurements of each part. For ECF printed samples, left R-Chart (fig. 3.23) presents a big range between the LCL and the UCL control limits, an indication of high variability due the gage (repeatability factor). On the right, we observe that the values fall into a more close range and measurements are closer to the central line, an indication of a higher influence of the Part-to-Part factor.

Figure 3.24 presents the X-Chart for the worst (left) and best (right) measurement systems for printed ECF samples (measurement system 3 and 8 respectively). Plotted points represent

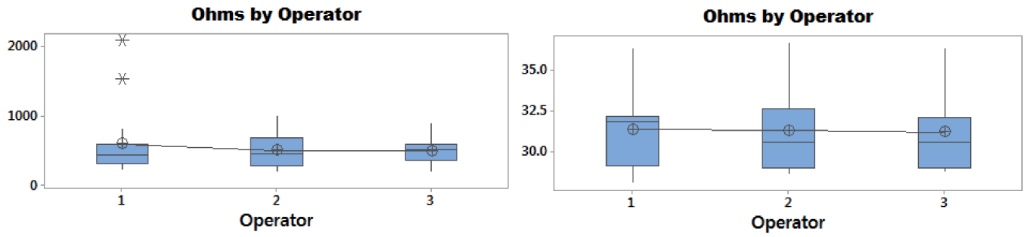

Figure 3.25: Ohms by operator for Printed-ECF specimens, worse on the left (measurement system 3), best on the right (measurement system 8)

.

the average measurement of each part for each operator. The center line is the overall average for all part measurements by all operators. Control limits (UCL and LCL) are based on the number of measurements in each average and the repeatability estimate. It is desirable to observe more variation between part averages than what is expected from repeatability variations alone. In the left X-Chart of the ECF printed samples (fig. 3.24), we observe that most measurements fall inside the upper and lower control limits (UCL and LCL), meaning that the variability of the system (gage) do not allow correct differentiation from the part-to-part variation factor (measurement system 3). On the contrary, the plot on the right shows that most of the measurements falls outside upper and lower limits, an indication that the part-to-part variation is much greater than the measurement device variation (measurement system 8).

Figure 3.25 presents the "Measurement by operator" plot for the worst (left) and best (right) measurement systems for printed ECF samples (measurement system 3 and 8 respectively). The Ohms by operator graph shows all of the study measurements, arranged by operator. Parallel lines means that the operators are on average measuring the parts similarly (measurement system 8). The box plot shows no spread in the measurements. This is not the case for measurement system 3 (fig. 3.25, left), where connecting lines are not parallel, meaning that there are important difference between the average means from each operator.

3.8 Conclusions

To develop embedded electronics that use ECF materials, it is critical to have a measurement system capable of providing resistivity/resistance readings with high repeatability and reproducibility. Otherwise, the design of electronic features and their later functioning could become difficult to predict and prompt to fail. To evaluate the performance of ten measurement systems for Non-ECF samples, Raw-ECF and Printed-ECF specimens, ten Crossed Gage R&R studies were conducted. For the Non-ECF specimens, the statistical results showed that for all measurement systems the highest percentage of variation was due to the Part-to-Part factor. It ranged from 99.97% to 99.99%. This is the ideal scenario, where the equipment and the operator introduces no significant errors into the measurements. The best result for the Non-ECF specimens, a 99.99% Part-to-Part contribution, was provided by the measurement system that used four-points and the resistivity cell fixture. Measuring system that used two-points, manual handheld multimeter and tip probe electrodes provided the worst result, a 99.97% Part-to-Part contribution. In general, the ten measurement systems performed adequately when using the Non-ECF specimens. For the Raw-ECF specimens, the Part-to-Part factor had the highest percentage of variation for the ten measurement systems. The operator variability was negligible. The tip point electrodes were more difficult to fix at a specific location using a standard pressure. It was observed that the measurement systems that used a two-point technique with alligator electrodes, the Part-to-Part percentage variation increased while the repeatability factor decreased. The reason is that the alligator electrodes were easier to position at the same location and the pressure remained constant across measurements. It was also observed a higher percentage variation on the Part-to-Part factor for measurement systems that used the four-point technique and alligator electrodes or the resistivity cell. These measurement systems are ideal for resistivity/resistance measurements because both the equipment and the operator introduce negligible errors to the measurements. For the Printed-ECF specimens, the measurement systems that used a two-point technique and alligator electrodes had a tendency to increase the Part-to-Part percentage variation and decrease the repeatability factor, explained again by the

use of alligator electrodes. The measurement systems that used a four-point technique and alligator electrodes or the resistivity cell showed a higher percentage variation on the Part-to-Part factor. In summary, the ten tested measurement systems are acceptable for measuring resistivity/resistance of Non-ECF specimens. They produced measurements with high repeatability and reproducibility. When measuring resistivity/resistance of raw and printed ECF specimens, the electrode placement and pressure over the specimen become critical factors to accomplish high repeatability and reproducibility. The measurement systems that used tip electrode probes and handheld devices proved to be inadequate to produce accurate measurements. Improvements were obtained by using alligator probes and the four-point method technique. The resistance introduced by the wires, equipment and electrode contact points were significantly reduced. These measurement systems proved to produce the best results. The measurement systems which uses the Resistivity Cell produced high repeatability and reproducibility measurements due to the fact that the electrode placement and pressure were more stable. The fixture accommodates the position of the electrodes and alerts the operator when the proper pressure has been reached. The fixture becomes of special importance when no trained personnel take the measurements. For the experiments, although other methods can be used to improve the contact between electrodes and ECF specimens (screws or wires directly melted into the specimen), a non-destructive method was chosen. This research produced measurement systems with high repeatability and reproducibility for measuring resistivity/resistance of raw and printed ECF specimens in a non-destructive manner. In most of the cases, the measured resistivity was similar to the reported by manufacturers.

Chapter 4

ECF Specimen Characterization

A measuring system with high performance is selected from the Gage R&R study. The system is used to measure and report the electric resistivity and resistance of raw and printed ECF specimens according to the Standard Test Method for D-C Resistance of Moderately Conductive Materials ASTM D4496-13 [13]. The method is suggested for materials that exhibit volume resistivity in the range of 10^0 to $10^7\Omega - cm$. The standard also requires a manual setup of voltage and current. Therefore, the measuring system 10 is selected since the other nine measuring systems use no manual setup. The measuring system 10 provided a high percentage variation in the Part-to- Part factor, 98.1% for raw and 98.3% for printed ECF specimens. The electric resistivity and resistance of five raw and five printed specimens from different manufacturers are measured using the measuring system 10. An operator measures the specimens under a controlled laboratory condition and for printed specimens in the two major anisotropy directions. The measurements are aggregated and reported according to the ASTM D4496-13 standard. Figure 4.1 shows the two anisotropy directions when measuring resistivity in the ECF printed specimens. In the anisotropy direction A (left), the electric current i flows in the same orientation the material is deposited during the printing process (X/Y plane of the 3D printer). In the anisotropy direction B (right), the electric current i flows through all the layers that build the specimen (Z axis of the 3D printer).

4.1 Test Subjects for Resistivity Report

A roll of $200gr$ of raw filament material of $1.75mm$ diameter is available from five manufacturers. The product characteristics are listed in Table 2.1. Five raw specimens of $100mm$ length

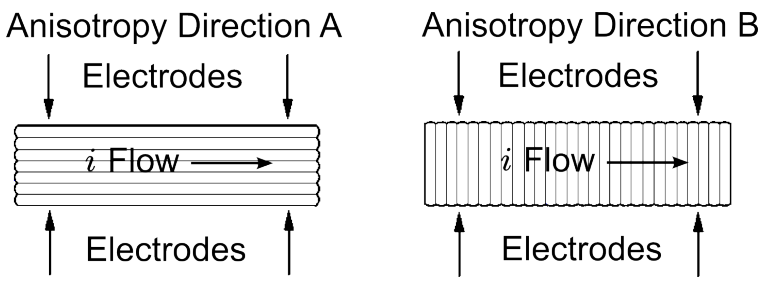

Figure 4.1: Two anisotropy directions for ECF printed specimens

.

are taken from each manufacturer roll. Two specimens are taken from the beginning of the roll, one specimen from the middle section, and two specimens from the second half of the roll. Five printed specimens are produced under identical conditions.

The raw specimens correspond to the shape in the left side of figure 3.2 (100mm length x 1.75mm diameter) and the printed specimens correspond to the shape in the right side of figure 3.2 (75mm length x 6mm width x 4mm height). The printed specimens are produced by a Prusa Mk2 FDM 3D Printer [47]. The printing parameters are presented in table 4.1.

Parameter	**Value**
Nozzle Temperature	Mid value from range suggested by manufacturer
Bed Temperature	Mid value from range suggested by manufacturer
Resolution	$0.2mm$
Infill	100%
Infill Pattern	Rectilinear
Shell	3 perimeter layers, 3 top layers, 3 bottom layers
Z-Offset	$-0.270mm$
Retraction Distance	$1.5mm$

Table 4.1: Common printing parameters

Other parameters such as retraction speed and coasting distance are set to their default values for PLA printing. No support material is required during the printing. Table 4.2 presents a summary of the most relevant printing parameters. The specimens are printed one at a time horizontally at a different location on the print bed, using the Simplify3D software [48]. A total of 25 specimens are printed in a random order and labeled for the experiment.

The printing parameter “Shell” means three bottom, top and perimeter layers.

The mass of the specimens is registered using an “Adventurer Pro” precision balance (Model AV114) [4]. The instrument has a resolution of $0.0001g$. The variation in the mass

Material	Nozzle Temp. ($^{\circ}C$)	Nozzle Heater P.I.D			Bed Temp. ($^{\circ}C$)	Bed Heater P.I.D			Print Speed (mm/s)	Cooling Fan (%)	Extrusion Multiplier
		P	I	D		P	I	D			
Multi3D Electrifi	145	17.98	1.42	56.69	Room	N	N	N	20	0	1.1
Functionalize F-Electric	235	19.77	1.58	61.95	50	43.98	1.69	285.58	40	0	1.0
Blac Magic Graphene PLA	220	16.96	1.29	55.58	53	53.29	1.99	356.87	33	100	1.1
PMG3D GPLA-C/Z2W ZY	205	19.77	1.58	61.95	Room	N	N	N	45	100	1.0
Proto-Pasta Composite PLA	215	18.83	1.5	59.01	50	56.71	2.20	364.66	40	100	1.0

Table 4.2: Printing parameters for ECF specimens (P.I.D: *Proportional Integral Derivative*)

is an indicator of potential under-extrusion or other issues while printing [49]. The distribution of material should be almost identical for specimens of the same material. Specimens with mass variation greater than $\pm 1\%$ should be inspected or reprinted.

4.2 Environment and Equipment

The 3D printer is calibrated to meet the nozzle and print bed temperatures suggested by each ECF manufacturer. These temperatures are controlled by software during the printing and external readings. A cleaning process is done after each print to ensure the elimination of material residues from previous printing.

4.2.1 3D Printer Temperature Calibration and Cleaning

Ensuring standard printing temperature of the nozzle and bed is important to avoid changes in material distribution or other issues while printing [50, 49, 51]. Since each manufacturer suggests a range of nozzle and print bed temperatures for the filament material, the center value is used in each case. The printer is then calibrated to those specific values to reduce temperature variation during printing. The 3D printer firmware provides commands for the internal calibration of the *Proportional Integral Derivative (PID)* controller, which is a control loop feedback mechanism keeping the nozzle and bed temperature on target. By default, the PID parameters are set to temperatures required by the use of PLA and ABS plastic [52]. By training the firmware to target specific temperatures, it is possible to obtain precise PID parameter values to control those temperatures while printing a filament. Table 4.2 lists the

PID parameter values for the nozzle and bed. The firmware is trained in a 5-loop cycle. After the training, the firmware reported the kP, kI and kD (PID) values to add to the Gcode script that is sent to the machine. For calibration, the firmware used the command:

$$M303\ E0\ S230\ C5$$

Where $M303$ represents the calibration command, $E0$ the tool (first extruder in this case), $S230$ the target temperature and $C5$ the number of calibration cycles. For the print-bed, $E0$ is replaced by $E-1$. The firmware reports calibration values for target temperatures as: kP, kI and kD. These values must be stored in the printer EEPROM or included at the beginning of the GCode script file to be sent to the printer. To do that, the $M301$ and $M304$ commands instruct the firmware to use specific calibration values for the nozzle (heat-block) and heat-bed respectively. The command to save the new calibration is as follows:

$$M301\ P19.77\ I1.58\ D61.95$$

$$M304\ P43.98\ I1.69\ D285.58$$

Where the values that the firmware reports after the calibration are those included in the P, I and D parameters, while $M301$ and $M304$ specify if those values are for the print head or print bed. The 3D Printer firmware was trained in a 5-loop cycle using the P.I.D feedback controlled algorithm [53]. After the training, target temperatures vary less than $\pm 2.5°C$ during printing.

Figure 4.2 shows a nozzle and print bed temperature summary chart. It compares the stability before and after the PID calibration. Top left and right plots are PLA prints before the PID calibration. ECF printed specimen chart illustrates the behavior after the PID calibration (only 2 printed specimens per chart). The range, mean, median, mode, variance, standard deviation and coefficient of variation are calculated over 180 readings of nozzle and print bed temperatures during approximately 10 minutes, which is the time it takes to print a specimen.

Previous to the 3D printer PID firmware calibration, the temperature of the nozzle and print bed could vary up to $6°C$. After the calibration, with the exception of one of the Proto-Pasta and Black Magic specimens, both temperatures varied by less than $\pm 3°C$. In some materials, the

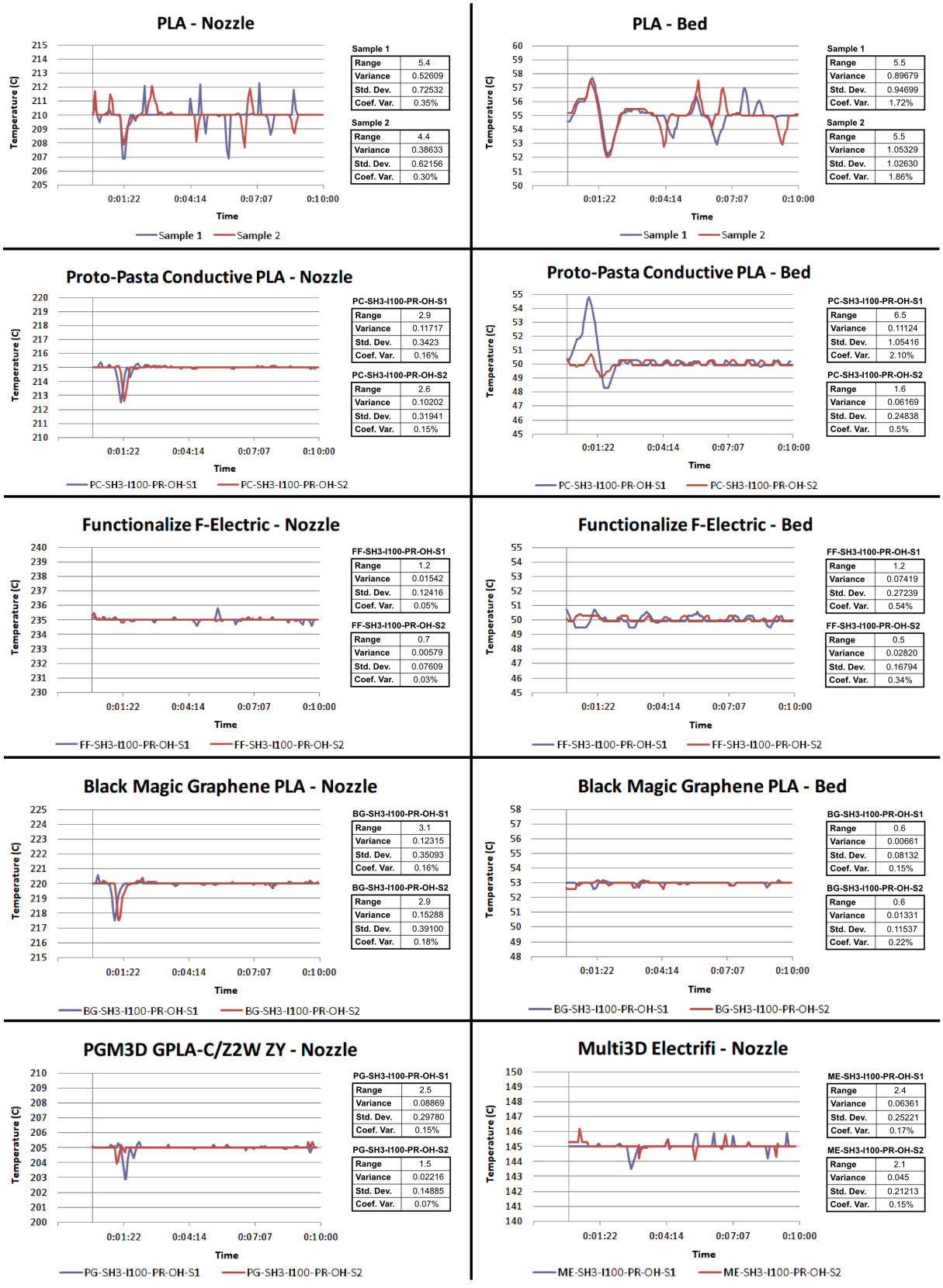

Figure 4.2: Summary comparison of nozzle and print bed temperatures before and after P.I.D calibration

.

	Nozzle Temperature (C)	Print Bed Temperature (C)	Nozzle Temperature Coefficient of Variation	Print Bed Temperature Coefficient of Variation
Proto-Pasta Conductive PLA	221	52.507	1.50%	3.74%
Functionalize F-Electric	216.433	52.690	1.59%	4.35%
BlackMagic Graphene PLA	219.283	52.380	1.10%	3.36%
PMG3D GPLA-C/Z2W ZY	204.933	23	1.54%	0.00%
Multi3D Electrifi	146.267	23	1.07%	0.00%

Table 4.3: ECF specimen print, external temperature readings

.

high variation on nozzle temperature while printing can be explained by the PID algorithm still reaching equilibrium. After that, the fluctuation in temperatures noticeably decreases. After the calibration, the coefficient of variation is reduced on average by more than half compared to before the calibration, meaning that the temperature is more stable during printing. Figure 4.2 presents the variations in temperature before and after the PID calibration (only 2 specimens per brand are presented in each chart). Top left and right plots are PLA prints before the PID calibration. The ECF print graphs show the behavior after the PID calibration.

Using the infrared temperature gun equipment [54], three independent external temperature readings, while printing each specimen, were taken from each corner at the center of the print bed and at the nozzle location. Table 4.3 presents the average temperatures and coefficient of variation for each type of filament. From this table, it is observed no variation over 5% on the print bed or the nozzle temperature during printing. The variation obtained by this method is higher than the internally reported data of the machine, but this can be explained by the motion of the print bed and nozzle while taking the external readings. Also, the proper perpendicularity and distance of the gun is important because they could introduce noise to the readings. The main goal of an external temperature measuring method is to ensure that the internal reported data by the machine is within the expected range. An internal miss calibration of the machine firmware could report a false temperature. Also, the gun allows for independent readings in each corner and center of the print bed, making sure that the temperature is even throughout

Figure 4.3: DynaPurge [3], cleaning filament for FDM 3D printers

.

the bed. There is no corner with a difference higher than 10% from the target bed temperature. Nozzle external readings also varied around 10% from the target temperature. Both coefficients of variation were under 5%.

The print bed is covered by a sheet of PEI (Polyetherimide), which is cleaned with isopropyl alcohol ($CH_3CH_0HCH_3$) after each print to avoid contamination due to residues on the build platform. The print-head/extrusion mechanism is purged after each change of filament using "Dyna-Purge", a cleaning product for 3D printers. It comes in the form of a straw of filament of $1.75mm$ diameter by $200mm$ length. It passes through the extruder and heat-block system as any regular print filament. The manufacturer specifies the temperature and other parameters for the cleaning. Figure 4.3 shows this product. Figure 4.4 shows the importance of the cleaning process. From left to right, it can be observed the residue inside the extrusion mechanism. This residue could mix with the next printed specimen and contaminate the specimen. When the cleaning filament passes through the system, all previous material is removed. Two straws of Dyna-Purge are use in each cleaning. Printing with Multi3D Electrifi material requires a layer of blue paper tape (masking painter's tape) on top of the PEI sheet to avoid too much adhesion that could scratch the print surface or damage the specimen during removal. This was observed in preliminary experiments. Figure 4.5 shows the process of printing specimens.

4.2.2 Enviromental Conditions

As stated in [39, p. 2], test specimens must be free of surface cracks, defects and substantially free from surface oxide, dirt, and grease. The experiment was conducted under laboratory controlled environmental conditions (handling, temperature, humidity and storage) at the *Center for Advanced Science, Innovation and Commerce (CASIC)* of Auburn University. For the

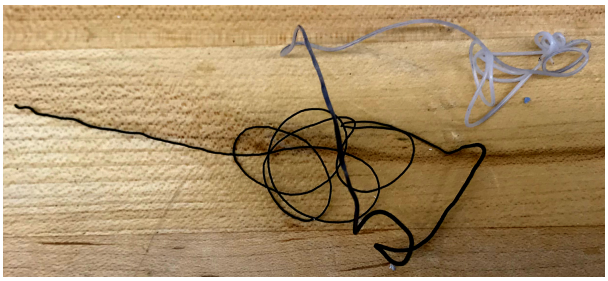

Figure 4.4: Extrusion mechanism residues following cleaning

.

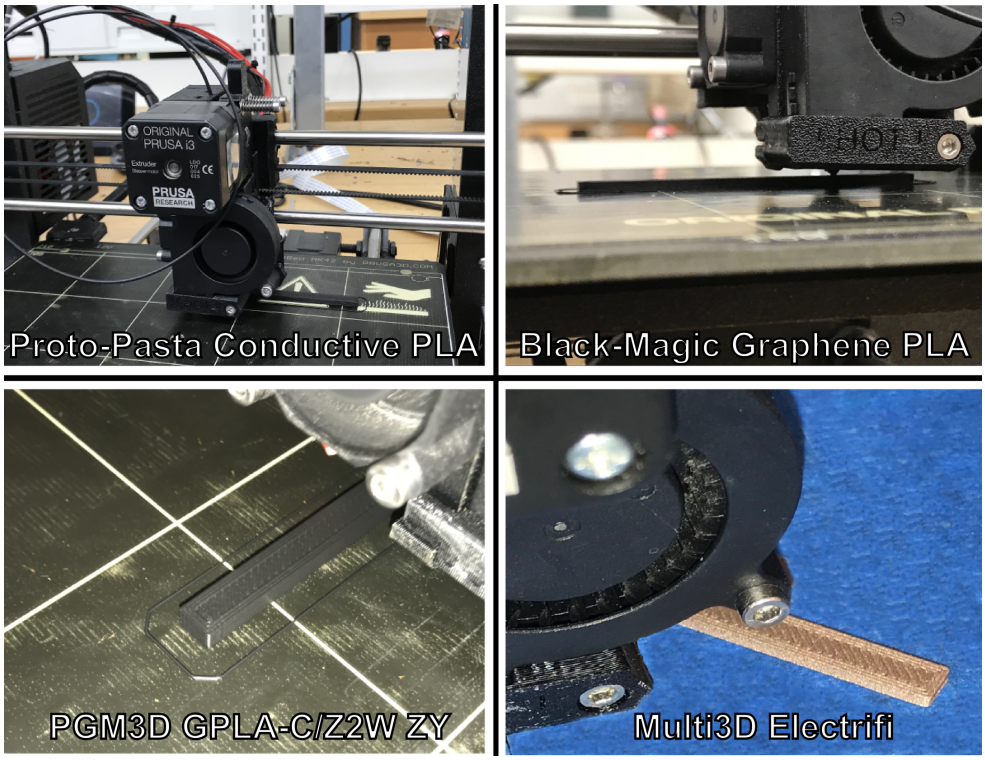

Figure 4.5: Printing of Specimens

.

composite materials listed in table 2.1, the polylactic acid (PLA) was used as binder. PLA is known as highly hygroscopic [55, 56, 57]. Hence, the water molecule concentration can alter the material properties, including its electric conductivity. The test specimens were labeled and stored independently in anti-static ESD bags and in a sealed container with controlled humidity 40% ($\pm 2\%$) and temperature of $24°C$ ($\pm 1°C$). The raw material and specimens were handled with nitrile gloves. ASTM D4496-13 standard discusses factors that affect the observed electric resistance (or conductance) in moderately conductive materials [13, p. 5]. The laboratory temperature and humidity were registered daily before and after the specimens were printed. The averages of the registered humidity and temperature were analyzed to determine their variation during the experiment. Less than $\pm 1\%$ and $\pm 2°C$ variation of laboratory humidity and temperature were measured, respectively.

Images of specimens, during and after printing, were taken and examined to search for defects such as readings gaps, under-extrusion, fractures, overflowing material and over-extrusion that could change the electric resistance of the material. Figure 4.5 shows a specimen of these images.

It is not realistic to expect that FDM will always produce perfect printed parts. Figure 4.6 shows some issues in FDM printed parts: gaps (fig. 4.6 d, f), under-extrusion (fig. 4.6 c, e), scratches (fig. 4.6 a), over-extrusion (fig. 4.6 b). The frequency of occurrence is highly dependent on the machine calibration, material quality and ambient conditions. Currently there is no specific data about the degree of occurrence of these issues in ECF materials. Moreover, there is currently no a standard *Verification and validation (V&V)* process for FDM produced parts. For the current experiment, printed specimens with alterations over 1% of the total surface area were rejected. All issues were detected by visual inspection of images during and after the printing process. All measurements were obtained using a digital caliper.

4.3 Resistivity Report

Resistivity measurements were taken on the five raw and printed specimens of each ECF material manufacturer (table 2.1). The same measurements are taken to the five printed ECF

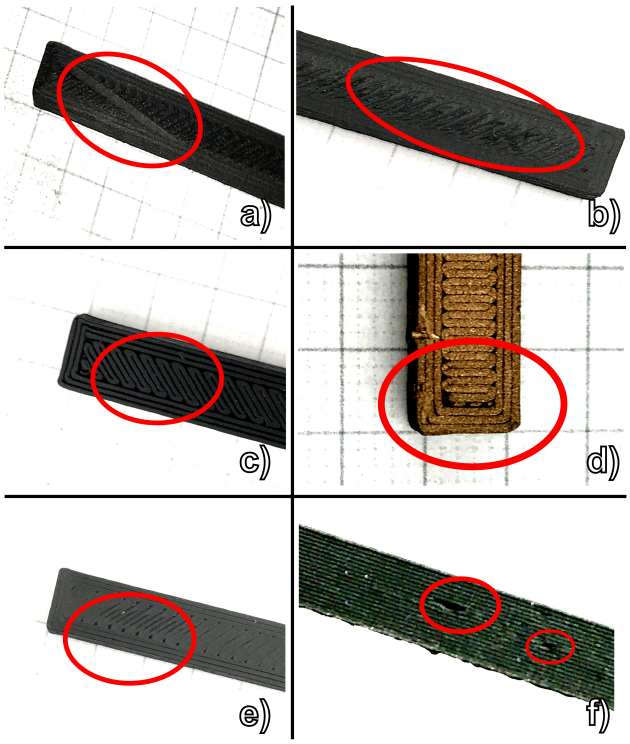

Figure 4.6: Imperfections on printed specimens (image contrast altered for visualization purposes)

.

specimens of each manufacturer over the two main anisotropy directions (figure 4.1). All measurements were taken using the measuring system 10 (table 2.2).

Resistivity calculations were done using the equation 2.4. In this equation is possible to use the exact distance between electrodes and compensate for the correct physical dimensions of each specimen.

There is a lack of resistivity data reported in standard form from ECF material manufacturers. In this chapter, resistivity data are reported following the ASTM D4496-13 standard. The resistivity data include raw and printed specimens in both anisotropy directions. The data presented allows for the selection of ECF materials not only by their resistivity property, but also select the manufacturer that provides higher accurate resistivity values. The cost associate to ECF materials has an inverse relationship between resistivity and price, the lower the resistivity the higher the price per grams. For a simple on/off detection, where no high conductivity is required, the selection of a material with high resistivity can bring the cost down while keeping the desired functionality.

Proto-Pasta Conductive PLA	Raw Specimens											
	Dimensions											
Specimen	Length (mm)	Diam. (mm)	Cross Area (mm2)	Mass (gr)	Constant Current (mA)	Drop Current (mA)	Drop Voltage (V)	Electrode Distance (mm)	Resistivity (Ohm-cm)	Specimen Resistance (Ohms)	Lab. Temp. (C)	Lab. Humdity (%)
PC-RS1	100.01667	1.73000	2.35062	0.31410	5.00000	3.55200	1.73500	29.98000	3.82981	1,629.54842	23.00	41.00
PC-RS2	100.01333	1.73667	2.36877	0.31360	10.00000	9.76600	4.95800	30.05000	4.00192	1,689.67519	22.00	41.00
PC-RS3	100.06472	1.74020	2.37842	0.31580	5.00000	3.40000	1.76000	30.65000	4.01690	1,689.99047	24.00	40.00
PC-RS4	99.98760	1.73650	2.36831	0.31380	10.00000	9.80000	5.24000	29.87000	4.23945	1,789.84793	24.00	40.00
PC-RS5	101.08740	1.74210	2.38361	0.31750	7.00000	6.70000	3.48500	30.02000	4.13003	1,751.51684	22.00	40.00
Avg	**100.23394**	**1.73709**						**Avg**	**4.04362**	**1,710.11577**	**23.00000**	**40.40000**

Table 4.4: Proto-Pasta conductive PLA raw specimens

Proto-Pasta Conductive PLA	Printed Specimens															
Anisotropy Direction A	Dimensions															
Specimen	Length (mm)	Width (mm)	Height (mm)	Total Area (mm2)	Cross Area (mm2)	Mass (gr)	Constant Current (mA)	Drop Current (mA)	Drop Voltage (V)	Electrode Distance (mm)	Resistivity (Ohm-cm)	Specimen Resistance (Ohms)	Lab. Temp. (C)	Lab. Humdity (%)	Nozzle Temp. (C)	Bed Temp. (C)
PC-PS1	74.96333	5.99667	3.98333	1,544.04158	23.88672	2.14200	5.00000	4.90600	0.58800	29.90000	9.57492	300.48824	24.00	41.00	214.94545	50.30248
PC-PS2	74.94000	5.98667	3.98667	1,542.53689	23.86684	2.14540	10.00000	8.90900	1.03100	29.90000	9.23748	290.04956	23.00	41.00	214.95041	49.99256
PC-PS3	75.04000	6.18660	3.78500	1,543.37029	23.41628	2.13560	15.00000	14.60000	1.77500	30.20000	9.42663	302.08655	24.00	40.00	214.75650	49.69641
PC-PS4	75.24000	6.08667	3.88600	1,547.99251	23.65279	2.10500	20.00000	19.70000	2.19000	30.20000	8.70669	276.96171	23.00	40.00	214.65087	49.49254
PC-PS5	75.26000	5.98668	3.98100	1,548.00114	23.83297	2.08500	5.00000	3.30000	0.39000	30.00000	9.38875	296.47879	24.00	40.00	214.85471	49.39224
Avg	**75.08867**	**6.04866**	**3.92440**							**Avg**	**9.26689**	**293.21297**	**23.60000**	**40.40000**	**214.83159**	**49.77525**

Table 4.5: Proto-Pasta conductive PLA printed specimens, anisotropy direction A

4.3.1 Proto-Pasta Conductive PLA

Tables 4.4, 4.5 (direction A) and 4.6 (direction B) present the descriptive statistics for the Raw-ECF and Printed-ECF specimens of Proto-Pasta material. The main physical characteristics of the specimens and environment conditions during measurements are also included.

4.3.2 PGM3D GPLA-C/Z2W ZY

Tables 4.7, 4.8 (direction A) and 4.9 (direction B) present the descriptive statistics for the Raw-ECF and Printed-ECF specimens of PGM3D GPLA-C material. The main physical characteristics of the specimens and environment conditions during measurements are also included.

Proto-Pasta Conductive PLA	Printed Specimens															
Anisotropy Direction B	Dimensions															
Specimen	Length (mm)	Width (mm)	Height (mm)	Total Area (mm2)	Cross Area (mm2)	Mass (gr)	Constant Current (mA)	Drop Current (mA)	Drop Voltage (V)	Electrode Distance (mm)	Resistivity (Ohm-cm)	Specimen Resistance (Ohms)	Lab. Temp. (C)	Lab. Humdity (%)	Nozzle Temp. (C)	Bed Temp. (C)
PC-PS1	74.96333	5.99667	3.98333	1,544.04158	449.53012	2.14200	5.00000	4.87000	0.09	30.05000	170.78910	461.01808	24.00	41.00	214.94545	50.30248
PC-PS2	74.94000	5.98667	3.98667	1,542.53689	448.64080	2.14540	10.00000	9.87000	0.2	31.40000	148.38016	483.61179	23.00	41.00	214.95041	49.99256
PC-PS3	75.04000	6.18660	3.78500	1,543.37029	464.24246	2.13560	15.00000	13.50000	0.25	29.80000	218.56207	466.31867	24.00	40.00	214.75650	49.69641
PC-PS4	75.24000	6.08667	3.88600	1,547.99251	457.96083	2.10500	20.00000	19.30000	0.35000	29.90000	186.49522	456.33979	23.00	40.00	214.65087	49.49254
PC-PS5	75.26000	5.98668	3.98100	1,548.00114	450.55754	2.08500	5.00000	3.30000	0.06	30.10000	176.44909	454.60586	24.00	40.00	214.85471	49.39224
Avg	**75.08867**	**6.04866**	**3.92440**							**Avg**	**180.13513**	**2,974.15299**	**23.60000**	**40.40000**	**214.83159**	**49.77525**

Table 4.6: Proto-Pasta conductive PLA printed specimens, anisotropy direction B

PGM3D GPLA-C/Z2W ZY	Raw Specimens											
	Dimensions											
Specimen	**Length (mm)**	**Diam. (mm)**	**Cross Area (mm2)**	**Mass (gr)**	**Constant Current (mA)**	**Drop Current (mA)**	**Drop Voltage (mV)**	**Electrode Distance (mm)**	**Resistivity (Ohm-cm)**	**Specimen Resistance (Ohms)**	**Lab. Temp. (C)**	**Lab. Humdity (%)**
PG-RS1	100.02000	1.73000	2.35062	0.30470	5.00000	3.59000	29.70000	30.05000	0.64714	275.36223	22.00	39.00
PG-RS2	100.01667	1.71000	2.29658	0.29880	10.00000	9.60400	81.50000	30.40000	0.64108	279.19282	24.00	40.00
PG-RS3	100.03470	1.73000	2.35062	0.31000	5.00000	3.30000	31.00000	30.06000	0.73458	312.61474	23.00	40.00
PG-RS4	99.99870	1.72000	2.32352	0.30870	10.00000	8.40000	75.80000	30.14000	0.69565	299.39258	23.00	40.00
PG-RS5	101.01220	1.72000	2.32352	0.31220	15.00000	13.50000	120.70000	29.95000	0.69362	301.54387	22.00	41.00
Avg	**100.21645**	**1.72200**						**Avg**	**0.68242**	**293.62125**	**22.80000**	**40.00000**

Table 4.7: PGM3D GPLA-C raw specimens

PGM3D GPLA-C/Z2W	Printed Specimens																
Anisotropy Direction A	Dimensions																
Specimen	**Length (mm)**	**Width (mm)**	**Height (mm)**	**Total Area (mm2)**	**Cross Area (mm2)**	**Mass (gr)**	**Constant Current (mA)**	**Drop Current (mA)**	**Drop Voltage (mV)**	**Electrode Distance (mm)**	**Resistivity (Ohm-cm)**	**Specimen Resistance (Ohms)**	**Lab. Temp. (C)**	**Lab. Humdity (%)**	**Nozzle Temp. (C)**	**Bed Temp. (C)**
PG-PS1	75.27000	6.22000	4.09667	1,604.03353	25.48127	2.24000	5.00000	3.68500	42.6000000	30.02000	0.98126	28.98567	24.00	39.20	204.94959	24.0
PG-PS2	75.43000	6.41667	3.96667	1,617.33522	25.45278	2.24970	10.00000	10.61000	123.00000	29.97000	0.98455	29.17743	23.00	40.90	204.99669	23.0
PG-PS3	74.58000	5.98000	3.89400	1,519.37808	23.28612	2.24877	15.00000	13.60000	160.00000	30.05000	0.91166	29.19839	23.00	40.20	204.95478	23.0
PG-PS4	75.04000	6.13000	3.97700	1,565.61658	24.37901	2.24940	20.00000	18.90000	208.00000	28.05000	0.95650	29.44161	23.00	39.70	204.91873	23.0
PG-PS5	74.97000	6.08000	4.25700	1,601.69490	25.88256	2.24410	5.00000	3.50000	43.00000	30.58000	1.03985	30.11969	24.00	40.30	204.89971	24.0
Avg	**75.05800**	**6.16533**	**4.03827**							**Avg**	**0.97476**	**29.38456**	**23.400**	**40.060**	**204.94390**	**23.4**

Table 4.8: PGM3D GPLA-C printed specimens, anisotropy direction A

PGM3D GPLA-C/Z2W	Printed Specimens															
Anisotropy Direction B	Dimensions															
Specimen	**Length (mm)**	**Width (mm)**	**Heigth (mm)**	**Total Area (mm2)**	**Cross Area (mm2)**	**Mass (gr)**	**Constant Current (mA)**	**Drop Current (mA)**	**Drop Voltage (mV)**	**Electrode Distance (mm)**	**Resistivity (Ohm-cm)**	**Specimen Resistance (Ohms)**	**Lab. Temp. (C)**	**Lab. Humdity (%)**	**Nozzle Temp. (C)**	**Bed Temp. (C)**
PG-PS1	74.96333	5.99667	3.98333	1,544.04158	449.53012	2.14200	5.00000	3.78000	41.9700000	31.06000	16.07	267.97520	24.00	39.20	214.94545	50.30248
PG-PS2	74.94000	5.98667	3.98667	1,542.53689	448.64080	2.14540	10.00000	10.96000	122.90000	30.04000	16.75	279.74033	23.00	40.90	214.95041	49.99256
PG-PS3	75.04000	6.18660	3.78500	1,543.37029	464.24246	2.13560	15.00000	13.80000	161.05000	31.07000	17.44	281.85985	23.00	40.20	214.75650	49.69641
PG-PS4	75.24000	6.08667	3.88600	1,547.99251	457.96083	2.10500	20.00000	18.76000	207.90000	29.94000	16.95	278.49580	23.00	39.70	214.65087	49.49254
PG-PS5	75.26000	5.98668	3.98100	1,548.00114	450.55754	2.08500	5.00000	3.54000	42.96000	30.20000	18.11	302.42541	24.00	40.30	214.85471	49.39224
Avg	**75.08867**	**6.04866**	**3.92440**							**Avg**	**17.06212**	**282.09932**	**23.40000**	**40.06000**	**214.83159**	**49.77525**

Table 4.9: PGM3D GPLA-C printed specimens, anisotropy direction B

Black Magic Graphene PLA	Raw Specimens											
	Dimensions											
Specimen	Length (mm)	Diam. (mm)	Cross Area (mm2)	Mass (gr)	Constant Current (mA)	Drop Current (mA)	Drop Voltage (mV)	Electrode Distance (mm)	Resistivity (Ohm-cm)	Specimen Resistance (Ohms)	Lab. Temp. (C)	Lab. Humdity (%)
BG-RS1	100.01333	1.76333	2.44207	0.32750	5.00000	4.57000	29.10000	29.95000	0.51920	212.63652	23.00	40.00
BG-RS2	100.01333	1.77333	2.46985	0.31690	10.00000	9.62800	55.40000	30.03000	0.47325	191.63563	24.00	41.00
BG-RS3	100.02400	1.77333	2.46984	0.31856	5.00000	4.57000	27.70000	31.01000	0.48276	195.50867	22.00	39.00
BG-RS4	100.06200	1.76330	2.44198	0.32410	10.00000	9.78800	62.30000	30.04000	0.51741	212.01341	22.00	40.00
BG-RS5	100.05500	1.77000	2.46057	0.31740	15.00000	14.73400	83.60000	29.97000	0.46584	189.42516	24.00	40.00
Avg	**100.03353**	**1.76866**						**Avg**	**0.49169**	**200.24388**	**23.00000**	**40.00000**

Table 4.10: Black Magic Graphene PLA raw specimens

Black Magic Graphene PLA	Printed Specimens															
Anisotropy Direction A	Dimensions															
Specimen	Length (mm)	Width (mm)	Height (mm)	Total Area (mm2)	Cross Area (mm2)	Mass (gr)	Constant Current (mA)	Drop Current (mA)	Drop Voltage (mV)	Electrode Distance (mm)	Resistivity (Ohm-cm)	Specimen Resistance (Ohms)	Lab. Temp. (C)	Lab. Humdity (%)	Nozzle Temp. (C)	Bed Temp. (C)
BG-PS1	75.62000	6.44667	4.27667	1,676.93742	27.57024	2.43800	5.00000	3.74400	41.8000000	30.05000	1.02432	28.09523	23.00	40.20	219.94380	52.98264
BG-PS2	75.32000	6.59000	4.35333	1,705.88067	28.68847	2.50630	10.00000	9.96900	128.00000	31.02000	1.18747	31.17647	24.00	40.40	219.92479	52.96446
BG-PS3	75.54000	6.45000	4.21800	1,666.13364	27.20610	2.56300	5.00000	3.72300	46.50000	30.15000	1.12704	31.29317	24.00	39.80	219.99870	52.97666
BG-PS4	75.06000	6.31000	4.34500	1,654.36250	27.41695	2.33800	10.00000	9.849	113.42000	29.97000	1.05349	28.84160	24.00	41.00	219.93340	52.74400
BG-PS5	74.85000	6.41000	4.26400	1,652.56228	27.33224	2.48600	15.00000	14.862	171.00000	31.01000	1.01413	27.77211	23.00	41.40	219.88700	52.99200
Avg	75.27800	6.44133	4.29140							**Avg**	**1.08129**	**29.43572**	**23.60000**	**40.56000**	**219.93754**	**52.93195**

Table 4.11: Black Magic Graphene PLA printed specimens, anisotropy direction A

4.3.3 Black Magic Graphene PLA

Tables 4.10, 4.11 (direction A) and 4.12 (direction B) present the descriptive statistics for the Raw-ECF and Printed-ECF specimens of Black Magic Graphene PLA material. The main physical characteristics of the specimens and environment conditions during measurements are also included.

4.3.4 Functionalize F-Electric

Tables 4.13, 4.14 (direction A) and 4.15 (direction B) present the descriptive statistics for the Raw-ECF and Printed-ECF specimens of Functionalize F-Electric. The main physical characteristics of the specimens and environment conditions during measurements are also included.

Black Magic Graphene PLA	Printed Specimens															
Anisotropy Direction B	Dimensions															
Specimen	Length (mm)	Width (mm)	Height (mm)	Total Area (mm2)	Cross Area (mm2)	Mass (gr)	Constant Current (mA)	Drop Current (mA)	Drop Voltage (mV)	Electrode Distance (mm)	Resistivity (Ohm-cm)	Specimen Resistance (Ohms)	Lab. Temp. (C)	Lab. Humdity (%)	Nozzle Temp. (C)	Bed Temp. (C)
BG-PS1	75.62000	6.44667	4.27667	1,676.93742	487.49693	2.43800	5.00000	3.66000	55.0000000	29.85000	18.65	380.69217	23.00	40.20	219.94380	52.98264
BG-PS2	75.32000	6.59000	4.35333	1,705.88067	496.35880	2.50630	10.00000	9.86700	170.00000	31.03000	20.75	418.20799	24.00	40.40	219.92479	52.96446
BG-PS3	75.54000	6.45000	4.21800	1,666.13364	487.23300	2.56300	5.00000	3.69000	60.00000	30.12000	20.38	407.79970	24.00	39.80	219.99870	52.97666
BG-PS4	75.06000	6.31000	4.34500	1,654.36250	473.62860	2.33800	10.00000	9.79	170.00000	30.03000	18.27	434.02971	24.00	41.00	219.93340	52.74400
BG-PS5	74.85000	6.41000	4.26400	1,652.56228	479.78850	2.48600	15.00000	14.83	270.00000	30.11000	18.37	452.58865	23.00	41.40	219.88700	52.99200
Avg	**75.27800**	**6.44133**	**4.29140**							**Avg**	**19.28670**	**299.29414**	**23.60000**	**40.56000**	**219.93754**	**52.93195**

Table 4.12: Black Magic Graphene PLA printed specimens, anisotropy direction B

Functionalize F-Electric	Raw Specimens											
	Dimensions											
Specimen	Length (mm)	Diam. (mm)	Cross Area (mm2)	Mass (gr)	Constant Current (mA)	Drop Current (mA)	Drop Voltage (mV)	Electrode Distance (mm)	Resistivity (Ohm-cm)	Specimen Resistance (Ohms)	Lab. Temp. (C)	Lab. Humdity (%)
FF-RS1	100.01333	1.69333	2.25203	0.31410	5.00000	4.63000	38.60000	30.01000	0.62563	277.84221	24.00	41.00
FF-RS2	100.01333	1.69667	2.26091	0.31360	10.00000	9.77900	89.10000	29.98000	0.68712	303.95517	24.00	42.00
FF-RS3	100.01333	1.69667	2.26092	0.31288	5.00000	3.50000	29.80000	30.02000	0.64124	283.65825	23.00	40.00
FF-RS4	100.02500	1.69255	2.24995	0.32000	10.00000	8.60000	71.40000	30.01500	0.62235	276.67503	22.00	39.00
FF-RS5	100.06700	1.69333	2.25202	0.30988	15.00000	13.70000	113.20000	29.97000	0.62089	275.88621	23.00	40.00
Avg	**100.02640**	**1.69451**						**Avg**	**0.63945**	**283.60337**	**23.20000**	**40.40000**

Table 4.13: Functionalize F-Electric raw specimens

Functionalize F-Electric	Printed Specimens															
Anisotropy Direction A	Dimensions															
Specimen	Length (mm)	Width (mm)	Height (mm)	Total Area (mm2)	Cross Area (mm2)	Mass (gr)	Constant Current (mA)	Drop Current (mA)	Drop Voltage (mV)	Electrode Distance (mm)	Resistivity (Ohm-cm)	Specimen Resistance (Ohms)	Lab. Temp. (C)	Lab. Humdity (%)	Nozzle Temp. (C)	Bed Temp. (C)
FF-PS1	74.91667	5.95667	3.98667	1,537.33727	23.74724	1.96120	5.00000	3.76200	54.1800000	31.08000	1.10040	34.71504	23.00	40.70	234.99917	49.99256
FF-PS2	75.05000	5.99000	3.95000	1,539.31500	23.66050	2.03550	10.00000	9.95000	126.00000	29.98000	0.99940	31.70053	24.00	40.50	235.00661	50.03223
FF-PS3	74.88000	6.02000	3.94000	1,539.04720	23.71880	2.02100	5.00000	4.50000	63.00000	31.20000	1.06431	33.60000	24.00	40.30	235.00240	50.04330
FF-PS4	75.01900	5.98000	3.96000	1,538.73932	23.68080	1.99800	10.00000	9.60000	132.00000	31.03000	1.04934	33.24239	23.00	39.90	234.99800	49.88900
FF-PS5	74.98000	5.99800	3.97400	1,543.07322	23.83605	1.99600	15.00000	14.60000	226.00000	32.56000	1.13320	35.64648	24.00	40.10	235.00300	50.02430
Avg	**74.96913**	**5.98893**	**3.96213**							**Avg**	**1.06933**	**33.78089**	**23.60000**	**40.30000**	**235.00184**	**49.99628**

Table 4.14: Functionalize F-Electric printed specimens, anisotropy direction A

Functionalize F-Electric	Printed Specimens															
Anisotropy Direction B	Dimensions															
Specimen	Length (mm)	Width (mm)	Height (mm)	Total Area (mm2)	Cross Area (mm2)	Mass (gr)	Constant Current (mA)	Drop Current (mA)	Drop Voltage (mV)	Electrode Distance (mm)	Resistivity (Ohm-cm)	Specimen Resistance (Ohms)	Lab. Temp. (C)	Lab. Humdity (%)	Nozzle Temp. (C)	Bed Temp. (C)
FF-PS1	74.91667	5.95667	3.98667	1,537.33727	446.25361	1.96120	5.00000	3.67800	45.0000000	30.30000	21.61	302.50782	23.00	40.70	234.99917	49.99256
FF-PS2	75.05000	5.99000	3.95000	1,539.31500	449.54950	2.03550	10.00000	9.98000	115.00000	31.02000	18.28	278.78936	24.00	40.50	235.00661	50.03223
FF-PS3	74.88000	6.02000	3.94000	1,539.04720	450.77760	2.02100	5.00000	4.49000	57.00000	30.16000	21.04	315.18317	24.00	40.30	235.00240	50.04330
FF-PS4	75.01900	5.98000	3.96000	1,538.73932	448.61362	1.99800	10.00000	9.59000	120.900000	30.01500	20.56	312.74874	23.00	39.90	234.99800	49.88900
FF-PS5	74.98000	5.99800	3.97400	1,543.07322	449.73004	1.99600	15.00000	14.30000	160.050000	30.13000	23.60	278.43912	24.00	40.10	235.00300	50.02430
Avg	**74.96913**	**5.98893**	**3.96213**							**Avg**	**21.01670**	**350.92659**	**23.60000**	**40.30000**	**235.00184**	**49.99628**

Table 4.15: Functionalize F-Electric printed specimens, anisotropy direction B

Multi3D Electrifi	Raw Specimens											
	Dimensions											
Specimen	Length (mm)	Diam. (mm)	Cross Area (mm2)	Mass (gr)	Constant Current (mA)	Drop Current (mA)	Drop Voltage (mV)	Electrode Distance (mm)	Resistivity (Ohm-cm)	Specimen Resistance (Ohms)	Lab. Temp. (C)	Lab. Humdity (%)
ME-RS1	100.01333	1.77333	2.46985	0.29880	5.00000	4.59300	48.90000	30.03000	0.87564	354.58061	23.00	42.00
ME-RS2	100.01333	1.77333	2.46985	0.30470	10.00000	9.58200	91.50000	30.05000	0.78486	317.81790	22.00	41.00
ME-RS3	100.03100	1.77288	2.46859	0.30210	5.00000	4.55700	49.30000	30.01000	0.88992	360.60895	24.00	40.00
ME-RS4	100.02330	1.77312	2.46926	0.29970	10.00000	9.59300	83.10000	30.40000	0.70362	285.01924	24.00	39.00
ME-RS5	100.01250	1.77298	2.46887	3.05100	15.00000	14.59500	93.80000	30.08000	0.52750	213.68557	24.00	41.00
Avg	**100.01869**	**1.77313**						**Avg**	**0.75631**	**306.34245**	**23.40000**	**40.60000**

Table 4.16: Multi3D Electrifi raw specimens

Multi3D Electrifi	Printed Specimens															
Anisotropy Direction A	Dimensions															
Specimen	Length (mm)	Width (mm)	Height (mm)	Total Area (mm2)	Cross Area (mm2)	Mass (gr)	Constant Current (mA)	Drop Current (mA)	Drop Voltage (mV)	Electrode Distance (mm)	Resistivity (Ohm-cm)	Specimen Resistance (Ohms)	Lab. Temp. (C)	Lab. Humdity (%)	Nozzle Temp. (C)	Bed Temp. (C)
ME-PS1	74.91667	5.95667	3.98667	1,537.33727	23.74724	1.96120	5.00000	3.752	2.0200000	30.05000	0.04255	1.34222	23.00	40.80	145.01488	23.00000
ME-PS2	75.05000	5.99000	3.95000	1,539.31500	23.66050	2.03550	10.00000	8.841	4.30000	30.01000	0.03835	1.21633	24.00	40.50	145.02727	23.00000
ME-PS3	75.06870	5.98800	3.96400	1,541.64027	23.73643	2.03560	5.00000	3.705	1.86000	30.03000	0.03968	1.25496	24.00	40.10	145.03188	23.00000
ME-PS4	74.94500	5.92100	3.97800	1,530.86859	23.55374	1.97800	10.00000	9.83400	5.42000	30.02000	0.04324	1.37594	23.00	40.30	145.01880	23.00000
ME-PS5	75.03650	5.96470	3.54600	1,469.60093	21.15083	1.98700	15.00000	14.926	8.11000	29.99000	0.03832	1.35948	22.00	40.40	145.04560	23.00000
Avg	**75.00337**	**5.96407**	**3.88493**							**Avg**	**0.04043**	**1.30979**	**23.20000**	**40.42000**	**145.02769**	**23.00000**

Table 4.17: Multi3D Electrifi printed specimens, anisotropy direction A

4.3.5 Multi3D Electrifi

Tables 4.16, 4.17 (direction A) and 4.18 (direction B) present the descriptive statistics for the Raw-ECF and Printed-ECF specimens of Multi3D Electrifi. The main physical characteristics of the specimens and environment conditions during measurements are also included.

4.3.6 Summary

A summary of the descriptive statistics for raw specimens is provided in table 4.19. With the exception of Multi3D Electrifi, all specimens presented a coefficient of variation of 5% or less, meaning that all readings were consistent. Almost all materials presented a lower resistivity

Multi3D Electrifi	Printed Specimens															
Anisotropy Direction B	Dimensions															
Specimen	Length (mm)	Width (mm)	Height (mm)	Total Area (mm2)	Cross Area (mm2)	Mass (gr)	Constant Current (mA)	Drop Current (mA)	Drop Voltage (mV)	Electrode Distance (mm)	Resistivity (Ohm-cm)	Specimen Resistance (Ohms)	Lab. Temp. (C)	Lab. Humdity (%)	Nozzle Temp. (C)	Bed Temp. (C)
ME-PS1	74.91667	5.95667	3.98667	1,537.33727	446.25361	1.96120	5.00000	3.832	1.9900000	30.03000	0.77	12.95540	23.00	40.80	145.01488	23.00000
ME-PS2	75.05000	5.99000	3.95000	1,539.31500	449.54950	2.03550	10.00000	8.781	4.56000	31.01000	0.75	12.56810	24.00	40.50	145.02727	23.00000
ME-PS3	75.06870	5.98800	3.96400	1,541.64027	449.51138	2.03560	5.00000	3.699	1.76000	30.02000	0.71	11.89807	24.00	40.10	145.03188	23.00000
ME-PS4	74.94500	5.92100	3.97800	1,530.86859	443.74935	1.97800	10.00000	9.91500	5.62000	31.01000	0.81	13.69886	23.00	40.30	145.01880	23.00000
ME-PS5	75.03650	5.96470	3.54600	1,469.60093	447.57021	1.98700	15.00000	14.877	7.99800	30.15000	0.80	13.37985	22.00	40.40	145.04560	23.00000
Avg	**75.00337**	**5.96407**	**3.88493**							**Avg**	**0.76923**	**12.90006**	**23.20000**	**40.42000**	**145.02769**	**23.00000**

Table 4.18: Multi3D Electrifi printed specimens, anisotropy direction B

Raw Specimens	Resistivity (Ohm-cm)								
	Central Tendency		Dispersion						
Material	Mean	Median	Min	Max	Range	Variance	Std. Dev.	Coeff. Variation	Mean Specimen Resistance (Ohms)
Proto-Pasta Conductive PLA (Graphite based)	4.04362	4.01690	3.82981	4.23945	0.40964	0.02350	0.15328	3.79077%	1,710.11577
PGM3D GPLA-C/Z2W ZY (Graphene based)	0.682417	0.6936229	0.6410826	0.734583	0.0935	0.0014937	0.038649	5.66353%	293.62125
Black Magic Graphene PLA (Graphene based)	0.4916926	0.4827595	0.4658384	0.519205	0.053366	0.0006267	0.025034	5.09143%	200.24388
Functionalize F-Electric (Graphene based)	0.6394456	0.6256265	0.6208865	0.687123	0.066237	0.000776	0.027857	4.35644%	283.60337
Multi3D Electrifi	0.7563076	0.784858	0.5274951	0.889919	0.362424	0.0220098	0.148357	19.61598%	306.34245

Table 4.19: ECF raw specimens descriptive statistics summary

Printed Specimens	Resistivity (Ohm-cm)								
Anisotropy Direction A	Central Tendency		Dispersion						
Material	Mean	Median	Min	Max	Range	Variance	Std. Dev.	Coeff Variation	Mean Specimen Resistance (Ohms)
Proto-Pasta Conductive PLA (Graphite based)	9.26689	9.38875	8.70669	9.57492	0.86823	0.11248	0.33539	3.61918%	293.21297
PGM3D GPLA-C/Z2W ZY (Graphene based)	0.97476	0.98126	0.91166	1.03985	0.12819	0.00217	0.04661	4.78153%	29.38456
Black Magic Graphene PLA (Graphene based)	1.08129	1.05349	1.01413	1.18747	0.17335	0.00547	0.07399	6.84258%	29.43572
Functionalize F-Electric (Graphene based)	1.06933	1.06431	0.99940	1.13320	0.13380	0.00259	0.05089	4.75913%	33.78089
Multi3D Electrifi	0.04043	0.03968	0.03832	0.04324	0.00492	0.00001	0.00233	5.76721%	1.30979

Table 4.20: ECF printed specimens descriptive statistics summary, anisotropy direction A

than the provided by the manufacturer. The exception was Multi3D Electrifi that showed a higher resistivity than the one provided by the manufacturer.

Similarly, table 4.20 presents a summary of the descriptive statistics of the printed specimens. In the anisotropy direction A, the printed specimens show, in some cases, resistivity values close to the ones provided by the manufacturers. The measured resistivity of PGM3D GPLA-C is only 2.5% lower than the reported resistivity by the manufacturer. In the case of Proto-Pasta, it is about 70% lower, and for Black Magic Graphene PLA approximately 80% higher, and Functionalize F-Electric a 40% higher. However, for Multi3D Electrifi, the measured resistivity is several times higher than the provided by the manufacturer. Notices that the resistivity values reported by the manufacturers correspond to printed specimens in the anisotropy direction A. The consistency of the measured resistivity and the provided by the manufacturers is critical to ensure the desired electric resistance after printing.

Printed Specimens	Resistivity (Ohm-cm)								
Anisotropy Direction B	Central Tendency		Dispersion						
Material	Mean	Median	Min	Max	Range	Variance	Std. Dev.	Coeff. Variation	Mean Specimen Resistance (Ohms)
Proto-Pasta Conductive PLA (Graphite based)	28.08778	27.77588	27.21580	28.95223	1.73643	0.59505	0.77139	2.75000%	464.37884
PGM3D GPLA-C/Z2W ZY (Graphene based)	17.06212	16.95111	16.06958	18.10524	2.03566	0.58143	0.76252	4.46906%	282.09932
Black Magic Graphene PLA (Graphene based)	26.96063	27.38727	24.54196	29.01093	4.46898	2.75681	1.66037	6.16000%	418.66364
Functionalize F-Electric (Graphene based)	17.81921	18.01938	16.69948	18.97403	2.27454	1.16458	1.07916	6.06000%	297.53364
Multi3D Electrifi	0.76923	0.77171	0.71246	0.81111	0.09865	0.00152	0.03900	5.06993%	12.90006

Table 4.21: ECF printed specimens descriptive statistics summary, anisotropy direction B

Table 4.21 presents a summary of the descriptive statistics of printed specimens for the anisotropy direction B. As expected, the resistivity measurements on the anisotropy direction B are higher than the provided by all manufacturers. The reason is that the current must pass through all layers of the printed specimen, accumulating the resistivity of all layers.

4.4 Experiment Design

From the resistivity data and dimensions of ECF specimens printed with 100% infill, the property can be described by equation 2.2. The electric resistance can then be calculated by equation 4.1.

$$R = \frac{\rho l}{(wh)} \tag{4.1}$$

where

R = Measured Resistance in Ohms (Ω)

ρ = Resistivity in Ohms meter ($\Omega - m$)

w = Specimen Width in meters (m)

h = Specimen Height in meters (m)

l = Specimen Length in meters (m)

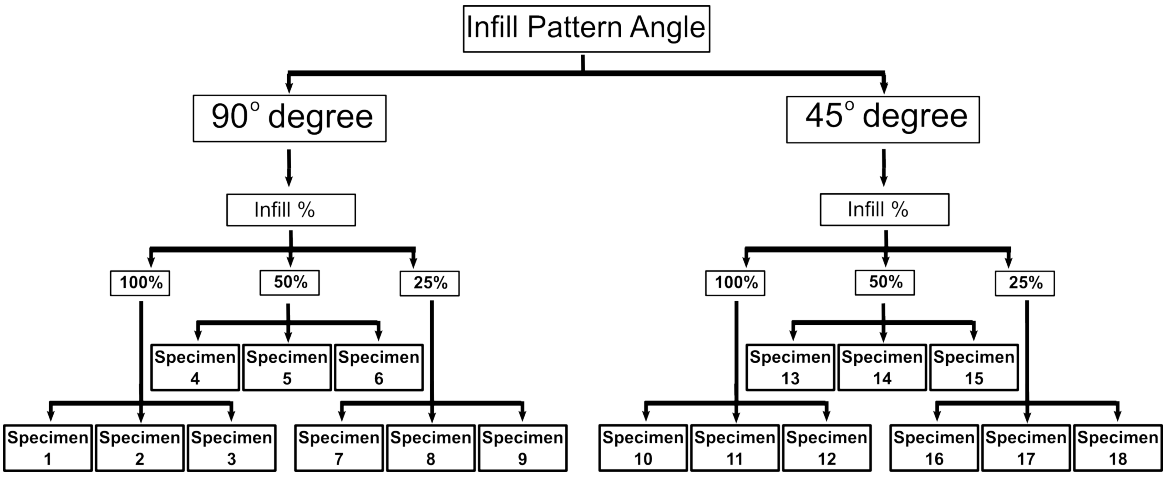

Figure 4.7: ECF characterization of infill/mass effects over electric resistance in printed specimens, study design.

.

Equation 4.1 is valid for ECF specimens printed with 100% infill. To understand the change of the electric resistance under different percentage of infill and pattern angles, a two-factor experiment was designed.

One factor is Infill Pattern Angle which indicates the angle of the infill line while printing the specimen. Figure 4.8 shows the pattern angle in the printed specimen. The $90°$infill pattern angle (fig. 4.8 a, b) switches between perpendicular lines of that angle at each layer. The infill pattern angle of $45°$also switches between perpendicular lines but diagonally compared with the orientation of the part (fig. 4.8 c, d). The infill pattern corresponds to the "Rectilinear" printing parameter. The second factor considered is the mass of the ECF printed specimen. The mass is represented by the $Infill\%$ print parameter. Three levels were selected: 100%, 50% and 25%. For each level, three specimens were printed (replicates). A total of nine specimens for each infill pattern angle.

The experiment was conducted independently for specimens of Proto-Pasta Conductive PLA and PGM3D GPLA-C/Z2W ZY. Notices that Proto-Pasta Conductive PLA presented a measured resistivity lower than the one reported by the manufacturer ($30\Omega-cm$ manufacturer vs $9.26\Omega-cm$ measured). Conversely, the measured resistivity of PGM3D GPLA-C/Z2W ZY was close to the one reported by the manufacturer ($1\Omega-cm$ manufacturer vs $0.9747\Omega-cm$ measured). The data is presented in table 2.1 and table 4.20.

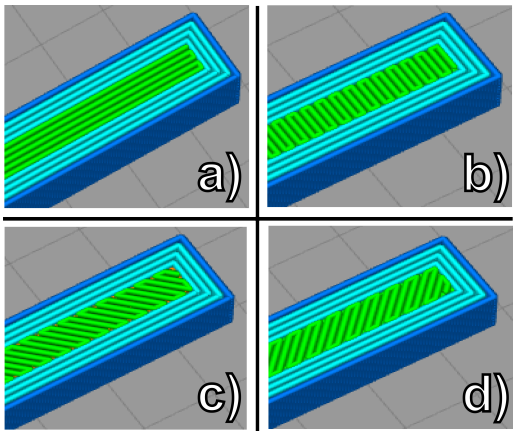

Figure 4.8: Infill Pattern Angle. Top left and right (a, b) represent a $90°$infill pattern angle. Bottom left and right (c, d) represent a $45°$infill pattern angle.

.

The statistical model of the experiment is expressed in equation 4.2.

$$Y_{ijk} = \mu + \tau_i + \beta_j + \gamma_{ij} + \epsilon_{ijk} \tag{4.2}$$

where

Y = Dependent variable. Response is measured as resistance (Ω)

μ = Overall mean response

τ = Infill pattern angle factor (independent variable), with $i = 1..2$ $(45$ or 90 $degrees)$

β = Infill % factor (independent variable), with $j = 1..3$ $(100\%, 50\%, 25\%)$

γ = Interaction factor between Infill Pattern Angle and Infill %

ϵ = Error

The null hypothesis for the experiment are:

- $H_{angle} : \tau_1 = \tau_1 = 0$;
- $H_{infill} : \beta_1 = \beta_2 = \beta_3 = 0$;

Figure 4.9: Ohaus Adventurer Pro precision weighing balance [4]

.

- $H_{interaction}$: $\gamma_{11} = \gamma_{12} = \gamma_{13} = \gamma_{21} = \gamma_{22} = \gamma_{23} = 0$;

With confidence level $\alpha = 0.05$, the experiment tests whether the infill pattern angle (H_{angle}) or the infill % (H_{infill}) and their interaction ($H_{interaction}$) have significant effects on the resistance of the specimens. The experiment was conducted using the anisotropy direction A of the specimens.

4.5 Test Subjects for Infill Experiment

Test subjects for this experiment consist of 3 replicates of each infill % per each of the infill pattern angles. Nine specimens were printed using Proto-Pasta Conductive PLA and nine specimens using PGM3D GPLA- C/Z2W. The geometry of the specimens corresponds to the shape at the right side of figure 3.2(75mm length x 6mm width x 4mm height). Specimens were printed as described in section 4.1. Printing parameters are listed in table 4.1, with the exception of "Shell width" (top and bottom layers and number of perimeter lines). The shell width was reduced from 4 ($100\% infill$) to 2 (50%) and then to 1 (25%) infill. The equipment calibration and ambient conditions were the same as described in section 4.2. The specimen handling and conditions were also the same as described in section 3.3. The geometry of each specimen was registered using a digital caliper. The mass of each specimen was recorded using a *Ohaus Adventurer Pro balance* (fig. 4.9). Three consecutive mass readings were taken and their averages calculated.

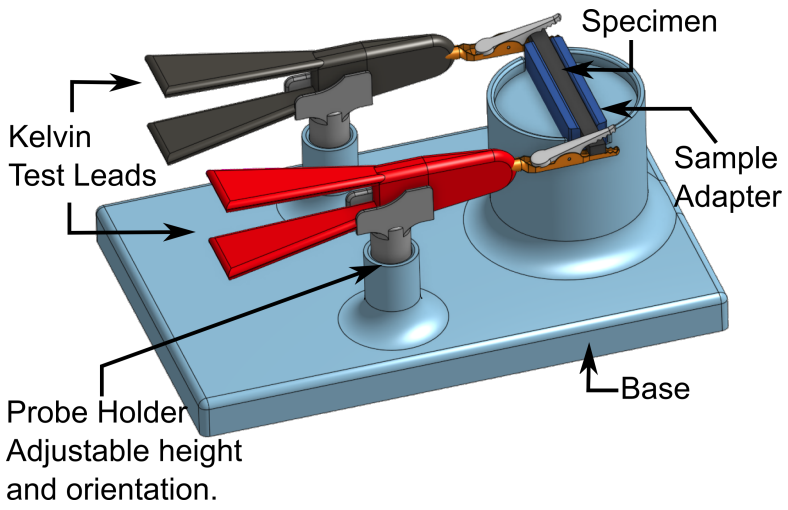

Figure 4.10: Custom 3D Printed fixture for electric resistance measurements

4.6 Methodology

All specimens were printed in a single session. First, all Proto-Pasta Conductive PLA specimens were printed followed by the printing of all PGM3D GPLA-C/Z2W specimens. Specimen combinations of infill pattern angle and infill % were printed randomly at different selected locations of the print bed (non-positioning pattern). Parts were coded and labeled. Before the experiment all specimens were masked and separated in containers for each material. Measuring System 7 was selected for this experiment. This system includes a *Keithley 2000 Benchtop Multimeter* (fig. fig.2.4c), Kelvin alligator probes for a 4-point electrode setup (fig. 2.6, right). Printed specimens were taken randomly and placed in a custom fixture for resistance measurement (fig. 4.10). Three consecutive electric resistance measurements were taken and their averages calculated. Data were aggregated in a spreadsheet. A custom fixture was designed and 3D printed for repeatability of electrode positioning. In the fixture described in figure 4.10, the visual markers allow for the specimen to be placed at the same location each time a measurement is taken. The Kelvin alligator test leads hook into holders to provide an adjustable height and orientation. Markers in the holders ensure that the test leads make contact with the specimen at the same location.

Proto-Pasta Conductive PLA								
90°Infill Angle Pattern								
Anisotropy Direction A								
Specimen	**Infill %**	**Length (mm)**	**Width (mm)**	**Height (mm)**	**Mass (gr) Avg**	**Specimen Resistance (Ohms)**	**Nozzle Temp. (C°)**	**Bed Temp. (C°)**
PC-MPS1	**100**	75.05000	6.07000	4.12000	2.12900	244.76300	230.35000	60.37000
PC-MPS2	**100**	74.98000	6.10000	4.14000	2.13433	236.70000	231.14000	60.02500
PC-MPS3	**100**	75.17000	6.40000	4.14000	2.13333	239.57667	231.58000	60.54000
PC-MPS4	**50**	74.89000	6.12000	4.09000	1.62400	323.96467	229.78400	60.15400
PC-MPS5	**50**	74.98000	6.11000	4.07000	1.62500	321.76700	230.59000	60.75100
PC-MPS6	**50**	74.99000	6.22000	4.03000	1.56167	325.44333	298.97800	59.70000
PC-MPS7	**25**	75.10000	6.15000	3.96000	1.09200	500.96833	229.68000	60.06870
PC-MPS8	**25**	75.08000	6.12000	3.98000	1.08900	500.68767	231.48000	59.89700
PC-MPS9	**25**	75.21000	6.11000	4.01000	1.09533	502.05237	230.45100	60.33000
	Avg	**75.01400**	**6.16000**	**4.11200**		**Avg**	**238.22589**	**60.20397**

Table 4.22: Proto-Pasta Conductive PLA specimens resistance for infill experiment (90°infill pattern angle)

4.7 Statistical Analysis

A two-factor analysis of variance (ANOVA) was performed using the Minitab 18 software [46]. Independent experiments were conducted with each of the two materials. The infill pattern angle factor had two levels ($90°$and $45°$) and the infill % had three levels (100%, 50% and 25%). A confidence level of 0.05 is considered significant. The analysis of the plots of the residuals was used to determine whether the model the assumption of normality.

4.8 Experimental Results

Tables 4.22 and 4.23 present the average electric resistance of the Proto-Pasta Conductive PLA specimens with 90°and 45°infill pattern angle respectively. Data about the geometry and mass of the specimens and the average temperature of the printer nozzle and print bed during printing are also displayed. Tables 4.22 and 4.23 show that the error of the machine to target specific dimensions was less than 1%. The temperature in the nozzle and in the print bed while printing also varied on average less than 1% from the target temperatures. The specimen resistance had a low variability of less than 3% for specimens of the same infill. Additional data showed that laboratory humidity varied less than 2% and laboratory temperature less than 2% while printing or handling the specimens.

Tables 4.24 and 4.25 present same data for the material PGM3D GPLA-C/Z2W ZY. These tables also show that the error of the machine to target specific dimensions is less than 1%.

Proto-Pasta Conductive PLA								
45°Infill Angle Pattern								
Anisotropy Direction A								
Specimen	**Infill %**	**Length (mm)**	**Width (mm)**	**Height (mm)**	**Mass (gr) Avg**	**Specimen Resistance (Ohms)**	**Nozzle Temp. (C°)**	**Bed Temp. (C°)**
PC-MPS10	**100**	75.11000	6.11000	4.03000	2.12967	242.72420	230.48000	59.47100
PC-MPS11	**100**	74.95000	6.13000	4.05000	2.13600	239.40700	230.56000	61.22500
PC-MPS12	**100**	74.98000	6.12000	4.10000	2.15133	238.47807	230.74000	60.17000
PC-MPS13	**50**	75.12000	6.07000	4.01000	1.62567	320.13317	230.19000	61.18774
PC-MPS14	**50**	75.06000	6.09000	4.08000	1.62700	322.32173	231.72000	59.32440
PC-MPS15	**50**	74.16000	6.03500	4.12000	1.62833	321.41757	231.49000	61.42500
PC-MPS16	**25**	75.04000	6.09000	4.07000	1.09533	500.23988	229.24700	60.32140
PC-MPS17	**25**	75.05000	6.15000	4.05000	1.09267	502.21997	229.22840	61.17200
PC-MPS18	**25**	75.82000	6.14000	4.05000	1.09133	503.27012	230.94000	60.27410
	Avg	**75.04400**	**6.10400**	**4.05400**		**Avg**	**230.51060**	**60.50785**

Table 4.23: Proto-Pasta Conductive PLA specimens resistance for infill experiment (45°infill pattern angle)

The nozzle and the print bed while printing varied in average less than 1% from the target temperatures. Specimen resistance had a low variability of less than 3% for specimens of the same infill. Laboratory conditions were also stable while printing or handling the specimens. The humidity had a variation of less than 2% and laboratory temperature less than 2%.

Tables 4.26 and 4.26 presents the ANOVA results of the infill % experiment for the Proto-Pasta Conductive PLA and PGM3D GPLA-C/Z2W ZY materials, respectively. With confidence level $\alpha = 0.05$, the results from both materials show a p-value for the $InfillPatternAngle$ factor greater than α supporting the null hypothesis for this factor. On the contrary, as expected, the $Infill\%$ factor presents a p-value lower than α, indicating that there is significant evidence to reject the null hypothesis for this factor. The interaction between $Infill\%$ and $InfillPatternAngle$ seems to be no significant, with a p-value higher than α. The null hypothesis for the interaction is supported.

The normal probability plots of the residuals for both experiments (top-left of fig. 4.11 and 4.12, respectively) verify the normality assumption of the model. The plot of the residuals versus fits confirms the assumption.

The histogram of the residuals can help to determine whether the data are skewed or include outliers. Although using less data points than the recommended 20 or more, the histogram of the residuals shows no skews on the data (bottom-left of fig. 4.11 and 4.12, respectively). The residuals versus order plot was used to verify that the residuals are independent. As showed

PGM3D GPLA-C/Z2W ZY 90°Infill Angle Pattern Anisotropy Direction A								
Specimen	**Infill %**	**Length (mm)**	**Width (mm)**	**Height (mm)**	**Mass (gr) (Avg)**	**Specimen Resistance (Ohms)**	**Nozzle Temp. (C°)**	**Bed Temp. (C°)**
PG-MPS1	**100**	75.05000	6.07000	4.12000	2.29667	22.33983	210.35000	27.00000
PG-MPS2	**100**	74.98000	6.10000	4.14000	2.29767	22.34518	210.12000	27.00000
PG-MPS3	**100**	75.08000	6.11000	4.14000	2.29633	21.60333	211.65000	27.00000
PG-MPS4	**50**	74.89000	6.12000	4.09000	1.81800	31.46533	209.97000	27.00000
PG-MPS5	**50**	74.98000	6.11000	4.07000	1.79833	31.28830	211.03000	27.00000
PG-MPS6	**50**	75.07000	0.17000	4.05000	1.81033	31.71450	210.65000	27.00000
PG-MPS7	**25**	75.30000	6.19000	4.26000	1.13733	61.92983	211.20000	27.00000
PG-MPS8	**25**	75.37000	6.32000	4.39000	1.16200	62.28907	210.50000	27.00000
PG-MPS9	**25**	75.85000	6.13000	4.29000	1.27133	63.30287	211.24000	27.00000
	Avg	**74.99600**	**6.10200**	**4.11200**		**Avg**	**210.62400**	**27.00000**

Table 4.24: PGM3D specimens resistance for infill experiment (90°infill pattern angle)

PGM3D GPLA-C/Z2W ZY 45°Infill Angle Pattern Anisotropy Direction A								
Specimen	**Infill %**	**Length (mm)**	**Width (mm)**	**Height (mm)**	**Mass (gr) Avg**	**Specimen Resistance (Ohms)**	**Nozzle Temp. (C°)**	**Bed Temp. (C°)**
PG-MPS10	100	75.63000	6.02000	4.15000	2.29767	21.80233	210.60000	27.00000
PG-MPS11	100	75.54000	6.11000	4.14000	2.29933	21.23790	210.58000	27.00000
PG-MPS12	100	75.45000	6.03800	4.14000	2.33767	22.07677	209.88000	27.00000
PG-MPS13	50	74.26000	6.12000	4.06000	1.92433	30.67267	209.69000	27.00000
PG-MPS14	50	75.43000	6.03000	4.09000	1.88667	31.47683	211.54000	27.00000
PG-MPS15	50	75.14000	6.08400	4.11000	1.90900	30.20260	210.36000	27.00000
PG-MPS16	25	74.89000	6.07000	4.11000	1.15567	59.79400	210.57000	27.00000
PG-MPS17	25	74.41000	6.10000	4.16000	1.15233	60.47467	210.67410	27.00000
PG-MPS18	25	75.12000	6.18000	4.15000	1.39000	61.87000	209.66000	27.00000
	Avg	**75.26200**	**6.06360**	**4.11600**		**Avg**	**210.45800**	**27.00000**

Table 4.25: PGM3D specimens resistance for infill experiment (45°infill pattern angle)

Analysis of Variance	**Proto-Pasta Conductive PLA**				
Source	**DF**	**Adj SS**	**Adj MS**	**F-Value**	**P-Value**
Infill %	2	214223	107112	22103.96	0.000
Infill Pattern Angle	1	2	2	0.36	0.557
Infill %*Infill Pattern Angle	2	8	4	0.81	0.469
Error	12	58	5		
Total	17	214291			

Table 4.26: Analysis of Variance (ANOVA) for infill pattern angle and infill % experiment using Proto-Pasta Conductive PLA material specimens

Analysis of Variance	PGM3D GPLA-C/Z2W ZY				
Source	**DF**	**Adj SS**	**Adj MS**	**F-Value**	**P-Value**
Infill %	2	5181.49	2590.75	6336.54	0.000
Infill Pattern Angle	1	4.18	4.18	10.22	0.008
Infill %*Infill Pattern Angle	2	1.63	0.81	1.99	0.179
Error	12	4.91	0.41		
Total	17	5192.20			

Table 4.27: Analysis of Variance (ANOVA) for infill pattern angle and infill % experiment using PGM3D GPLA-C/Z2W ZY material specimens

in the bottom-right of figure 4.11 and 4.12, the residuals present no trends or patterns when displayed in time order.

Since the infill % of the specimens is related to the mass (gr), a distribution plot is presented in figure 4.13 and 4.14 for each of the materials under experimentation. The plots show the relationship between the infill pattern angle factor (X axis) and the mass of each specimen (Y axis left), which corresponds with each level of the infill % factor (Y axis right).

The figures 4.15 and 4.16 show the relationship between the specimen resistance in Ohms (Y left axis) and the infill % factor levels in the X axis. Since the electric resistance of the specimens is related to their mass, the Y right axis displays the average weight in grams of the specimens of each infill % group.

For the computation of the resistance, the length of the specimen is multiplied by the resistivity of the material (equation 4.1). Keeping the width and height fixed, it is expected than the electric resistance double or be reduced by half according to the proportional length compared with the known values. To test this concept, four potential shapes or "Paths" were considered (figure 4.17). One simple application of ECF materials is the construction of connected traces where components are later placed along these lines forming circuits. Figure 4.17 describes four simple paths that were tested with the same materials used in the previous experiment. The top-left path corresponds to the same shape and dimensions of the specimens used before (75mm length x 6mm width x 4mm height). Path 02 doubles the length of path 01 doing an "L" shape (figure 4.17, top-right). Path 03 has a length of 1.5 times the length of path 01, also designed as an "L" shape. A more complex path is Path 04 shown in the bottom-right of figures 4.17. In Path 04 an "S" shape doubles the length of path 01. All paths remain with a

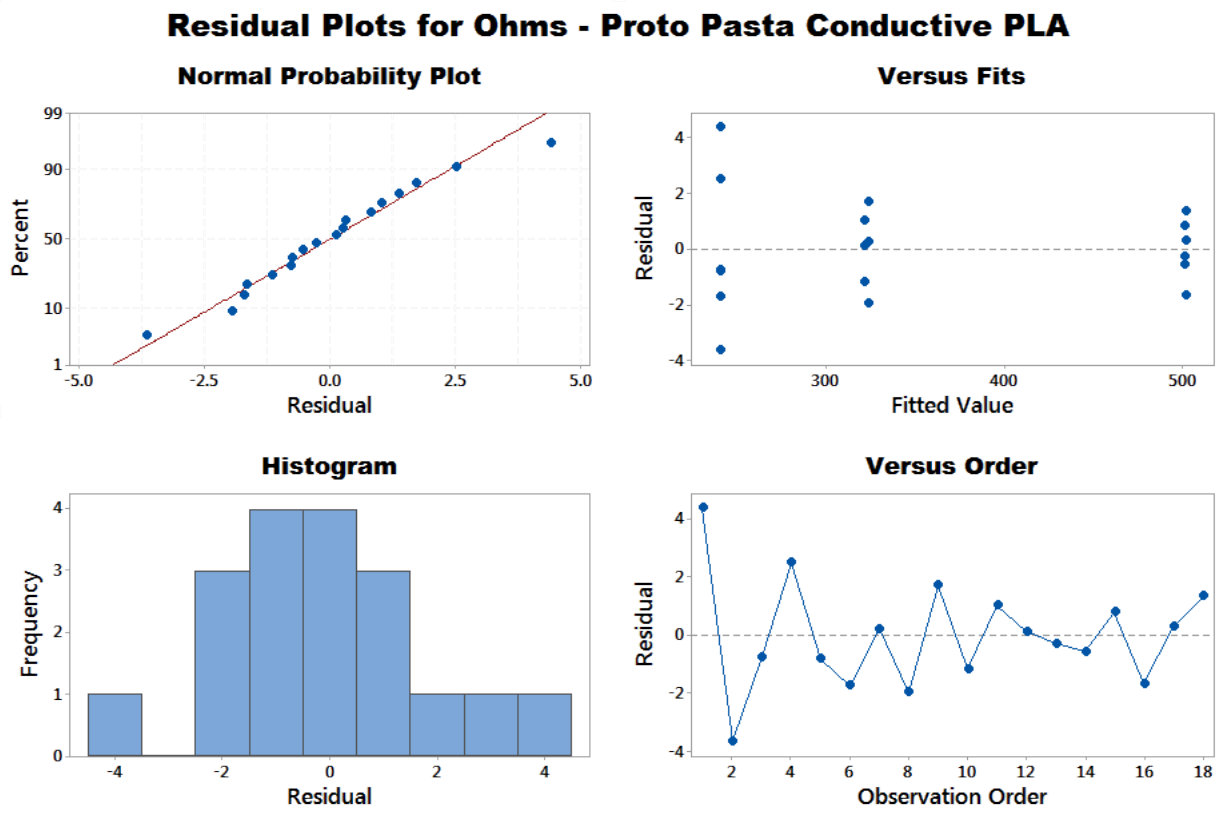

Figure 4.11: Residuals plots for Ohms, Proto-Pasta Conductive PLA

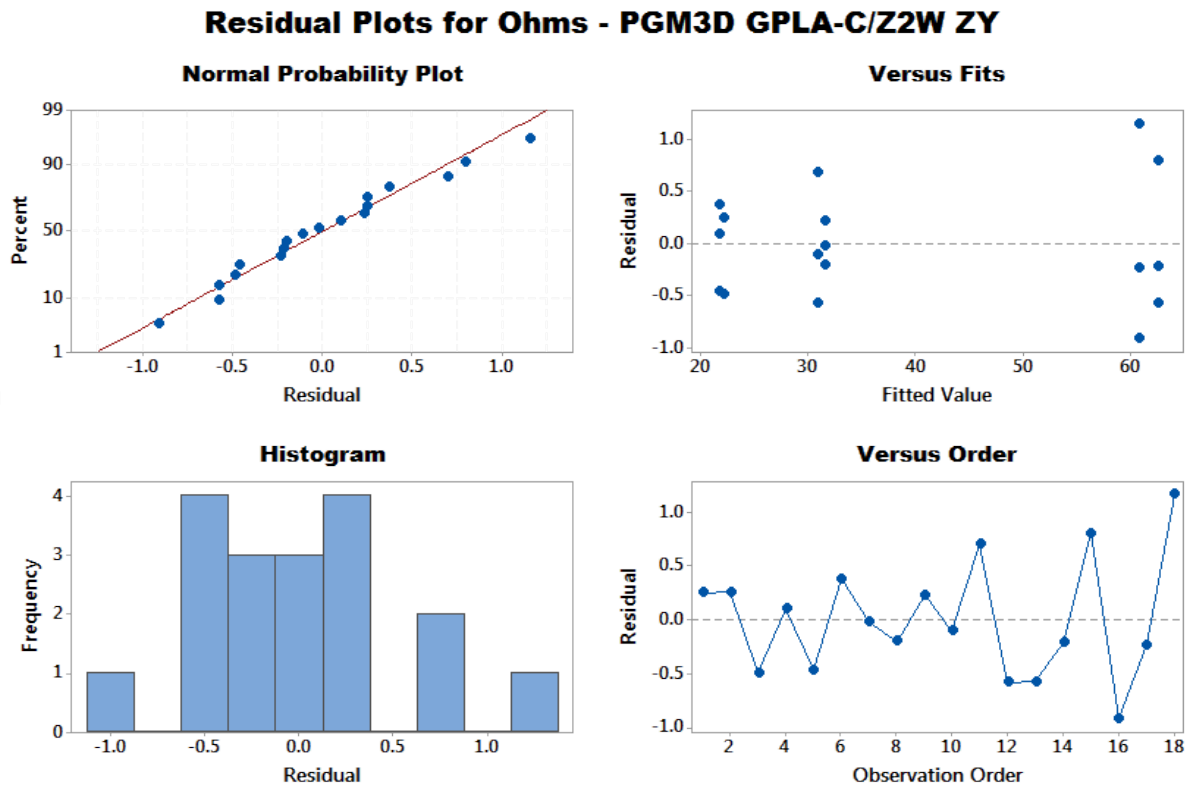

Figure 4.12: Residuals plots for Ohms, PGM3D GPLA-C/Z2W ZY

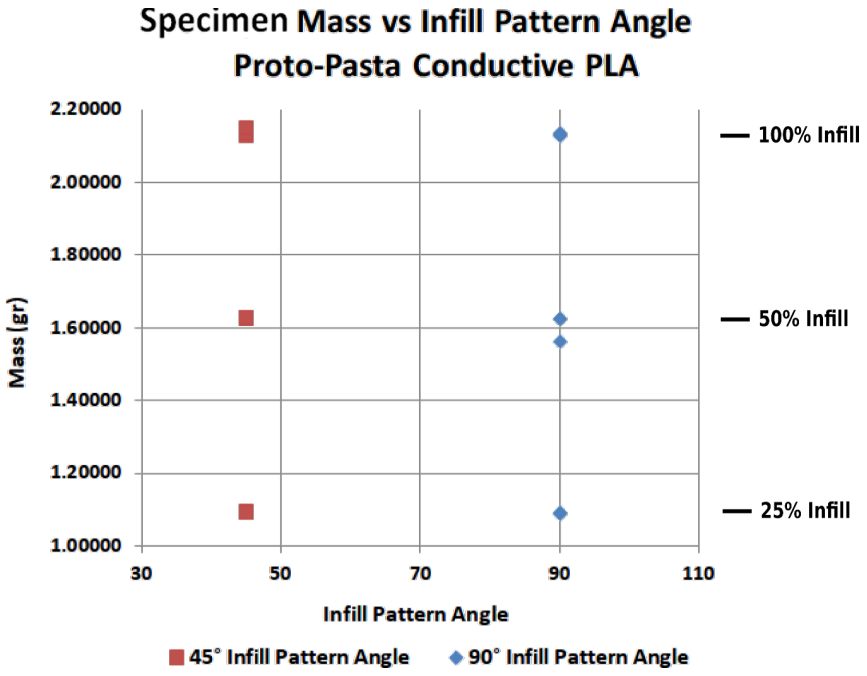

Figure 4.13: Mass vs infill pattern angle, Proto-Pasta Conductive PLA specimens

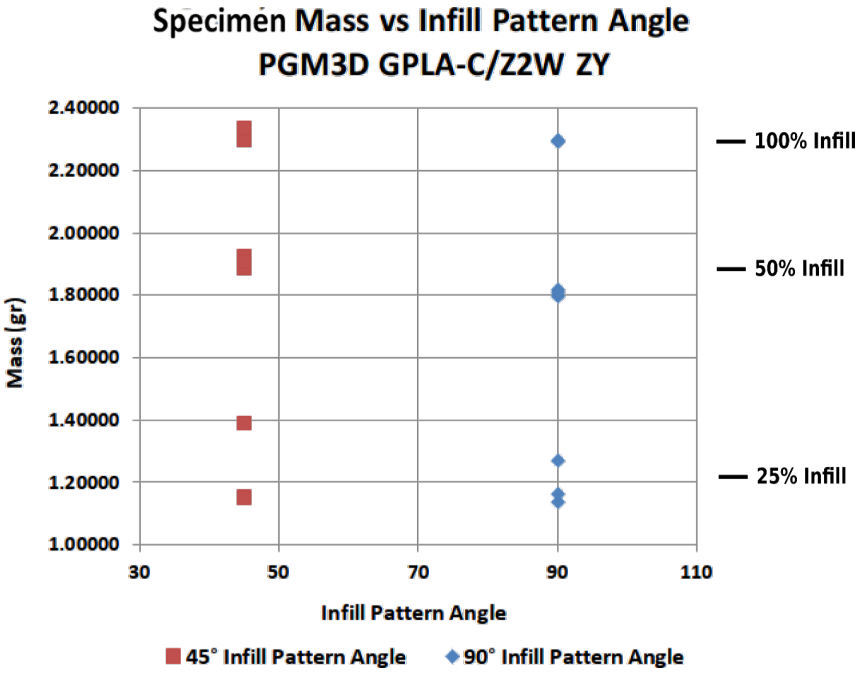

Figure 4.14: Mass vs infill pattern angle, PGM3D GPLA-C/Z2W ZY specimens

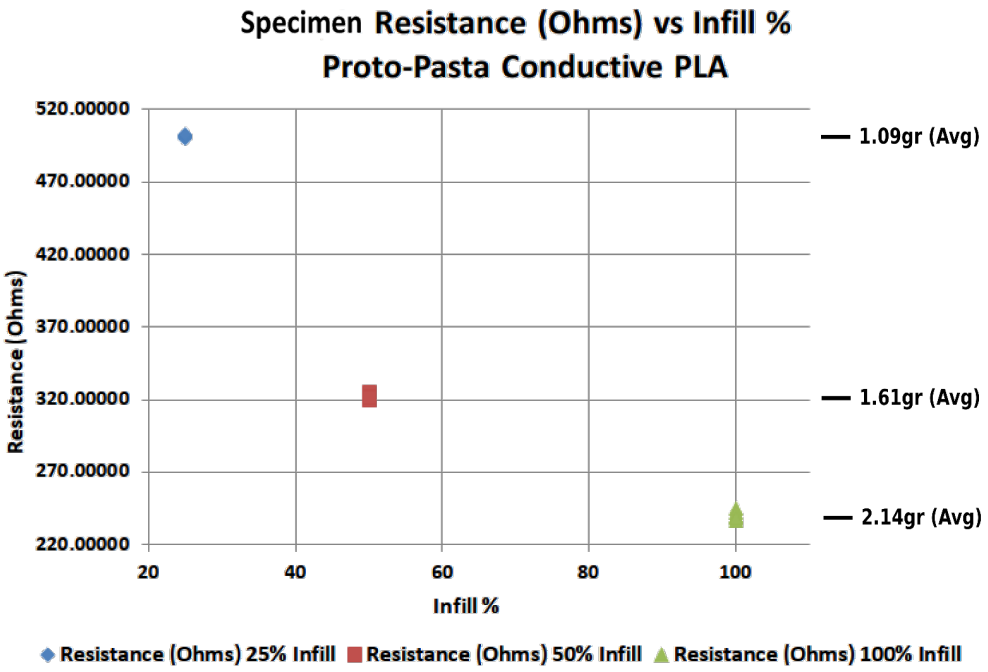

Figure 4.15: Mass vs infill %, Proto-Pasta Conductive PLA specimens

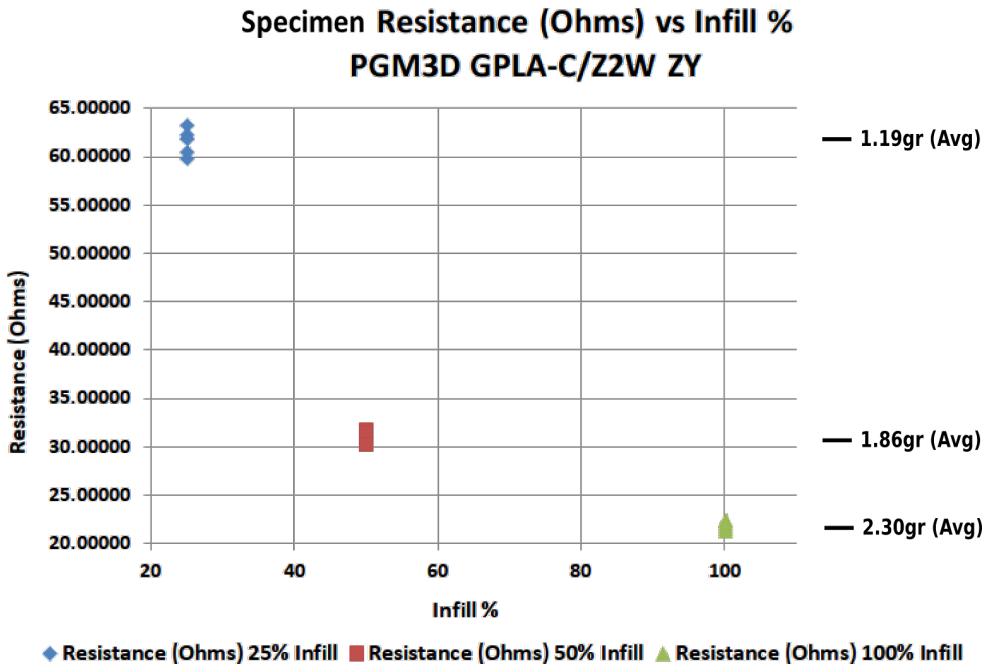

Figure 4.16: Mass vs infill %, PGM3D GPLA-C/Z2W ZY specimens

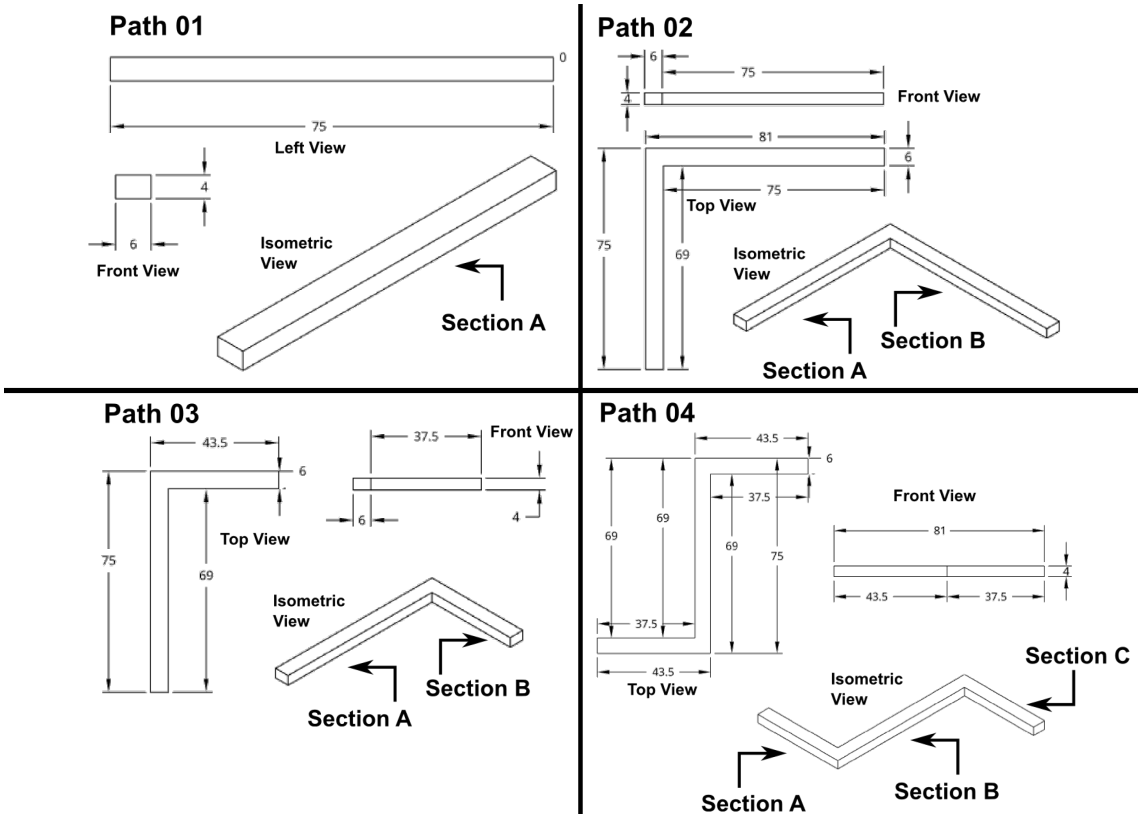

Figure 4.17: ECF 3D Printed paths

	Proto-Pasta Conductive PLA							
Path 02	**Anisotropy Direction A**							
Specimen	**Section**	**Length (mm)**	**Width (mm)**	**Height (mm)**	**Mass (gr) Avg**	**Specimen Resistance (Ohms)**	**Calc. Specimen Resistance (Ohms)**	**Total Read Specimen Resistance (Ohms)**
PC-PA2-PS1	**A**	75.35000	6.12000	4.08000		259.51607	279.644242	
	B	75.56000	6.12000	4.08000		270.88433	280.423609	
	SubTotal	**150.91000**			**4.16333**	**530.40040**	**560.067851**	**525.986**
PC-PA2-PS2	**A**	75.27000	6.14000	4.06000		260.46900	279.809027	
	B	75.65000	6.14000	4.06000		270.71223	281.221641	
	SubTotal	**150.92000**			**4.16667**	**531.18123**	**561.030668**	**536.784**
	Avg	**150.91500**	**6.13000**	**4.07000**	**4.16500**	**530.79082**	**560.54926**	**531.38500**

Table 4.28: Specimens of printed path 02 of Proto-Pasta Conductive PLA material

width of 6mm and 4mm height. Sections were labeled to help with the identification of specific geometry and electric resistance measurements. All specimens were 100% infill, 4 layers shell (perimeter, bottom and top layers), and rectilinear infill pattern with 90°infill pattern angle. Printing parameters are given in table 4.1.

Two specimens of each path and materials are printed. The geometry of the specimens was registered by a digital caliper and electric resistance measured using Measuring System 7. Three electric resistance measurements were taken and averages calculated per each section and for the total length of the printed path specimens. Also, three total mass measurements of the specimens were taken and averages calculated using a precision balance [4].

According to equation 4.1, the electric resistance is calculated knowing only the resistivity of the material and the geometry of the specimen. Therefore, using the electric resistivity of the materials reported in table 4.20 ($9.2668\Omega-cm$ and $0.9747\Omega-cm$), the expected electric of the path specimens and the total path resistance were calculated.

Results corresponding to path 01 are presented in 4.22 and 4.24 (first two specimens of each table). Data corresponding to path 02 are presented in tables 4.28 and 4.31. Tables 4.29 and 4.32 show results corresponding to path 03 and tables 4.30 and 4.33 present the data for path 04.

In figures 4.18 and 4.19, distribution plots show the relationship between the mass (Y left axis) and the total path length (X axis) for the two materials. Since the electric resistance is affected by the total mass of the specimen, the Y right axis presents the averages Ohms for each length group.

	Proto-Pasta Conductive PLA							
Path 03	**Anisotropy Direction A**							
Specimen	**Section**	**Length (mm)**	**Width (mm)**	**Height (mm)**	**Mass (gr) Avg**	**Specimen Resistance (Ohms)**	**Calc. Specimen Resistance (Ohms)**	**Total Read Specimen Resistance (Ohms)**
PC-PA3-PS1	**A**	75.28000	6.14000	4.11000		252.34300	276.441746	
	B	37.58000	6.14000	4.11000		131.29267	138.000542	
	SubTotal	**112.86000**			**3.12067**	**383.63567**	**414.442289**	**376.25**
PC-PA3-PS2	**A**	75.27000	6.18000	4.13000		254.08467	273.286136	
	B	37.42000	6.18000	4.13000		132.79400	135.862458	
	SubTotal	**112.69000**			**3.10333**	**386.87867**	**409.148594**	**378.68**
	Avg	**112.77500**	**6.16000**	**4.12000**	**3.11200**	**385.25717**	**411.79544**	**377.46500**

Table 4.29: Specimens of printed path 03 of Proto-Pasta Conductive PLA material

	Proto-Pasta Conductive PLA							
Path 04	**Anisotropy Direction A**							
Specimen	**Section**	**Length (mm)**	**Width (mm)**	**Height (mm)**	**Mass (gr) Avg**	**Specimen Resistance (Ohms)**	**Calc. Specimen Resistance (Ohms)**	**Total Read Specimen Resistance (Ohms)**
PC-PA4-PS1	**A**	37.68000	6.08000	4.14000		140.49800	138.720672	
	B	75.56000	6.08000	4.14000		244.51567	278.177653	
	C	37.12000	6.08000	4.14000		134.06067	136.659006	
	SubTotal	**113.24000**			**4.23667**	**519.07433**	**553.557332**	**505.75**
PC-PA4-PS2	**A**	37.38000	6.16000	4.07000		139.96633	138.16511	
	B	75.63000	6.16000	4.07000		246.23463	279.54594	
	C	36.59000	6.16000	4.07000		136.03333	135.245087	
	SubTotal	**113.01000**			**4.22333**	**522.23430**	**552.956137**	**503.685**
	Avg	**113.12500**	**6.12000**	**4.10500**	**4.23000**	**520.65432**	**553.25673**	**504.71750**

Table 4.30: Specimens of printed path 04 of Proto-Pasta Conductive PLA material

	PGM3D GPLA-C/Z2W ZY							
Path 02	**Anisotropy Direction A**							
Specimen	**Section**	**Length (mm)**	**Width (mm)**	**Height (mm)**	**Mass (gr) Avg**	**Specimen Resistance (Ohms)**	**Calc. Specimen Resistance (Ohms)**	**Total Read Specimen Resistance (Ohms)**
PG-PA2-PS1	**A**	74.82000	6.08000	4.16000		26.19767	28.8350038	
	B	74.82000	6.08000	4.16000		27.11860	28.8350038	
	SubTotal	**149.64000**			**4.12667**	**53.31627**	**57.6700076**	**51.687**
PG-PA2-PS2	**A**	74.93000	6.17000	4.09000		27.87534	28.9431956	
	B	74.93000	6.17000	4.09000		27.40730	28.9431956	
	SubTotal	**149.86000**			**4.15333**	**55.28264**	**57.8863912**	**53.237**
	Avg	**149.75000**	**6.12500**	**4.12500**	**4.14000**	**54.29945**	**57.77820**	**52.46200**

Table 4.31: Specimens of printed path 02 of PGM3D GPLA-C/Z2W ZY material

	PGM3D GPLA-C/Z2W ZY							
Path 03	**Anisotropy Direction A**							
Specimen	**Section**	**Length (mm)**	**Width (mm)**	**Height (mm)**	**Mass (gr) Avg**	**Specimen Resistance (Ohms)**	**Calc. Specimen Resistance (Ohms)**	**Total Read Specimen Resistance (Ohms)**
PG-PA3-PS1	**A**	75.29000	6.16000	4.07000		28.74393	29.2726065	
	B	37.45000	6.16000	4.07000		13.68066	14.5604876	
	SubTotal	**112.74000**			**3.12667**	**42.42460**	**43.8330941**	**40.7689**
PG-PA3-PS2	**A**	75.11000	6.13000	4.05000		27.66113	29.4904557	
	B	37.41000	6.13000	4.05000		14.96177	14.6882965	
	SubTotal	**112.52000**			**3.11333**	**42.62290**	**44.1787521**	**41.1125**
	Avg	**112.63000**	**6.14500**	**4.06000**	**3.12000**	**42.52375**	**44.00592**	**40.94070**

Table 4.32: Specimens of printed path 03 of PGM3D GPLA-C/Z2W ZY material

	PGM3D GPLA-C/Z2W ZY							
Path 04	**Anisotropy Direction A**							
Specimen	**Section**	**Length (mm)**	**Width (mm)**	**Height (mm)**	**Mass (gr) Avg**	**Specimen Resistance (Ohms)**	**Calc. Specimen Resistance (Ohms)**	**Total Read Specimen Resistance (Ohms)**
PG-PA4-PS1	**A**	37.68000	6.08000	4.14000		15.13503	14.5917101	
	B	75.56000	6.08000	4.14000		30.25170	29.2608709	
	C	37.12000	6.08000	4.14000		14.88573	14.3748482	
	SubTotal	**113.24000**			**4.26667**	**60.27247**	**58.2274291**	**58.0676**
PG-PA4-PS2	**A**	37.38000	6.16000	4.07000		14.06450	14.5332718	
	B	75.63000	6.16000	4.07000		28.25113	29.4047978	
	C	36.59000	6.16000	4.07000		14.15037	14.2261213	
	SubTotal	**113.01000**			**4.24667**	**56.46600**	**58.1641909**	**57.581**
	Avg	**113.12500**	**6.12000**	**4.10500**	**4.25667**	**58.36923**	**58.19581**	**57.82430**

Table 4.33: Specimens of printed path 04 of PGM3D GPLA-C/Z2W ZY material

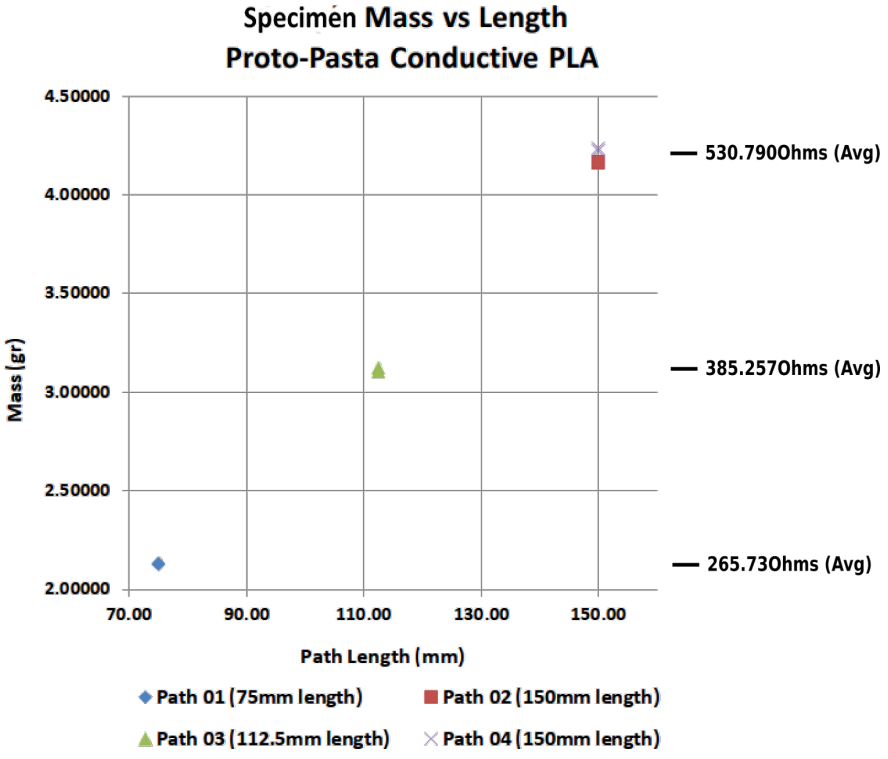

Figure 4.18: Mass vs length, Proto-Pasta Conductive PLA path specimens

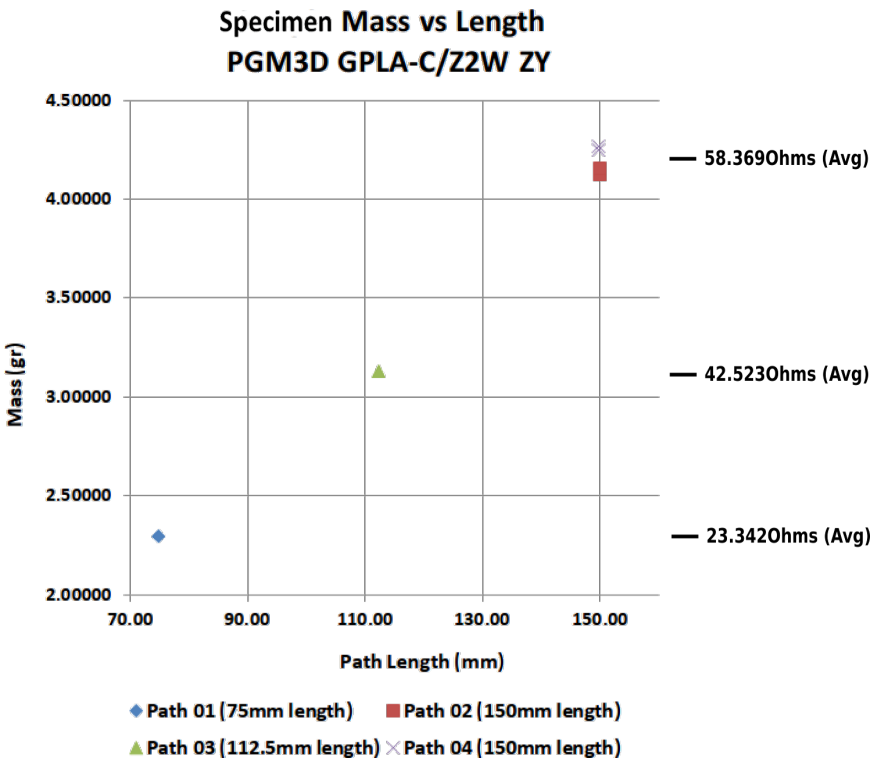

Figure 4.19: Mass vs length, PGM3D GPLA-C/Z2W ZY path specimens

4.9 Conclusions

A report on resistivity and resistance for five ECF materials was created according to the ASTM D4496-13 standard. The measurements were taken using the Measuring System 10 which uses a 4-point technique with constant current and custom fixture. The report includes raw specimens and printed specimens in the anisotropy direction A and B for the five ECF manufacturers. The experimental measurements provided a source of comparison the data reported by the manufacturers. Most of the manufacturers reports resistivity values close to the experimental results. The experimental results of the PGM3D GPLA-C/Z2W ZY material were the closest to the values reported by the manufacturer. The Multi3D Electrifi material presented the lowest resistivity between all materials tested. It had also the higher variability on the measurements. The Proto-Pasta Conductive PLA material had the higher resistivity. All graphene-based materials (Black Magic Graphene PLA, PGM3D GPLA-C/Z2W ZY and Functionalize F-Electric)

presented a similar resistivity of around $1\Omega - cm$. The correct measurement of resistivity/resistance in the anisotropy direction B presented some challenges. Since the perimeter lines are printed by the machine around the geometry of the part, it became difficult to position electrodes in a manner where only the material along the Z axis was in contact with the electrodes. A small contact with the borders and the measurement would correspond to the anisotropy direction A. In addition, the computation of the resistivity in the anisotropy direction B is not valid. Further research should be done to improve the fixtures and obtain a resistivity model for other specimen geometries. One suggestion is to test with specimens of the same geometry but oriented perpendicularly, producing a vertical version of specimens currently produced in the X/Y plane. An experiment was designed to better understand the effects of the infill % and infill angle pattern into the electric resistance. The materials Proto-Pasta Conductive PLA and PGM3D GPLA-C/Z2W ZY were selected for the experiment. The ANOVA results showed that for the Proto-Pasta Conductive PLA material only the infill % has a significant effect on the electric resistance. However, for the PGM3D GPLA-C/Z2W ZY material, the results showed that the infill % and the infill pattern angle factors had a significant effect on the electric resistance. The interaction factor between infill % and infill pattern angle showed to be no significant in both materials. Closer inspection to the resistance of PGM3D GPLA-C/Z2W ZY specimens revealed specimens with 45°pattern angle presented approximately 1Ω more compared to the other specimens. An explanation is that the printer parameters about "Infill width" and "Infill outline overlap" for the PGM3D GPLA-C/Z2W ZY material needed more tight adjustments to avoid an excess of material while doing the diagonal infill pattern angle. Nevertheless, the difference in the electric resistance measurements between specimens of the same infill % with different infill angle patterns was less than 1% for both materials. The residuals plots validated the normality assumption and constant variance. Less than 5% of the observations was flagged as having a large residual. Therefore, the observations model is adequate and meets the assumptions of regression. Results from the analysis of residuals indicates that the model fits the data and meets the assumptions of regression. It was observed that when reducing the infill factor from 100% to 50% and then to 25%, parts are not produced with half or a quarter of the mass of the original. This observation was also present even after

reducing the infill % and the specimen shell from 4, to 2 and to 1. This is important to consider since controlling the mass of an specific part is critical for predicting the electric resistance. There was no significant variation on the mass independently of the infill pattern angle. For the Proto-Pasta Conductive PLA material, the mass of the specimens for 100% and 50% infill was reduced about 25%. The mass of specimens for 50% and 25% infill was reduced about 32%. For the PGM3D GPLA-C/Z2W ZY material, the mass of specimens for 100% and 50% infill was reduced about 17%. The mass of specimens for 50% and 25% infill was reduced about 40%. Further experiments are needed to understand the effect of Infill % on the resulting mass and its effect on the electric resistance of printed parts. An experiment was conducted to check the model of the resistance computation. Four "Paths" that simulate the construction of connected traces were created and specimens printed. As expected, when the length was double, the mass and the electric resistance doubled. There is a direct proportional relationship between length, mass and electric resistance for the Proto-Pasta Conductive PLA and PGM3D GPLA-C/Z2W ZY materials. Knowing the geometry of the path specimens and the resistivity, was possible to compute the electric resistance of individual segments of the path as well as the complete path. The calculated values were highly similar when compared with the readings from the 4-point technique and laboratory equipment. It is recommended that for low resistance of ECF printed parts, a high % of material infill should be used. Short and thin traces can also provide high electrical conductivity. More experiments need to be conducted to determine geometries where the resistance calculation equation is valid.

Chapter 5

ECF Humidity Sensor, Test Case

Environmental monitoring is critical in research such as forecasting, climate change, and healthcare [58]. Presence of gases, humidity and temperature levels, light conditions and air pollution are some variables measured to detect some anomaly condition [59]. In basic weather monitoring, two important variables are relative humidity and temperature [60, 61, 62]. These two variables are also critical in monitoring and controlling specific application environments [63]. A significant amount of research has focused on the development of high-performance sensors. The goal of this research has focused on improving the performance, reducing the cost, and making the fabrication process easier and compatible with mass production [64, 65]. Ideally, a sensor should be highly sensitive, stable, accurate and inexpensive. In addition, it should be easy to fabricate and interface with and able to work under a wide operation range [66, 67]. Typically, a sensor does not meet all of these requirements [68]. Rather, a trade-off may be needed [69, 70]. On the plus side, sensors for specific applications are not required to have all characteristics but just few needed for the specific application [71]. A skin thermometer, for example, the sensor needs to be highly accurate, but the temperature range can be limited [72, 73]. New advances in additive manufacturing have made possible the fabrication of electronic sensors which could not be developed through conventional processes [74, 75]. With current 3D printing technology, it is possible to integrate embedded devices such as sensors, conductive traces, heat sinks, and antennas [76]. Several materials and additive manufacturing techniques have been tested to fabricate sensors for pressure, displacement, optical, tactile, electrocardiography, accelerometers, biosensors, gas, flow, humidity, antennas and RF shields. Literature in [22] presents a complete review of embedded electronic features integrated into

3D printed parts. 3D printed humidity sensors have only been produced by using the "Direct Ink Writing" (DIW) additive manufacturing technique [77] and the Dimatix Materials Printer (DPM) technology [78] (Stratasys PolyJet DMP-2800). There have been no attempts to build a humidity sensor using the hygroscopic properties of graphene molecules in ECF composite materials for FDM. Composite materials made of polylactic acid (PLA) and graphene have been used to produce electrical features into 3D printed parts, mostly for circuit traces [79, 25] and temperature sensors [6]. In this research, a graphene-based conductive filament is used to 3D print embedded sensors. This process is ideal for remote locations and on-demand because FDM is an inexpensive footprint manufacturing technology.

5.1 Experiment Design

It is known that the resistance of the graphene-based conductive filament changes according to the absorption of H2O (water) molecules of the surrounding environment. The kinetics of water molecules absorption in a PLA material has been studied in [55, 56, 80, 81, 82, 83, 84]. However, no research has been reported on its effects on the electric resistance of composites where the PLA is used as the bonding matrix. Although its potential effects have been discussed in [22, 79, 25], no actual research has been reported. Understanding the behavior of the electric resistance response under dry and water-submerged cycles is critical for using ECF materials as humidity sensors.

A statistical experiment to understand the electric resistance response on ECF materials when they are subject to repetitive dry and water-submerged cycles is designed and conducted.

The layout of the experiment is shown in Figure 5.1. The objective of the experiment is to test whether the water absorption in the PLA actually produces a measurable change in the electric resistance of ECF composite materials. Furthermore, as indicated in chapter 3 and 4, measuring the electric resistance of ECF materials is not a trivial task. The variability on the readings could distort the water absorption effect over the electric resistance response. And, if this response is measurable with precision, then the experiment addresses the question if this phenomenon can be reproduced in a timely manner.

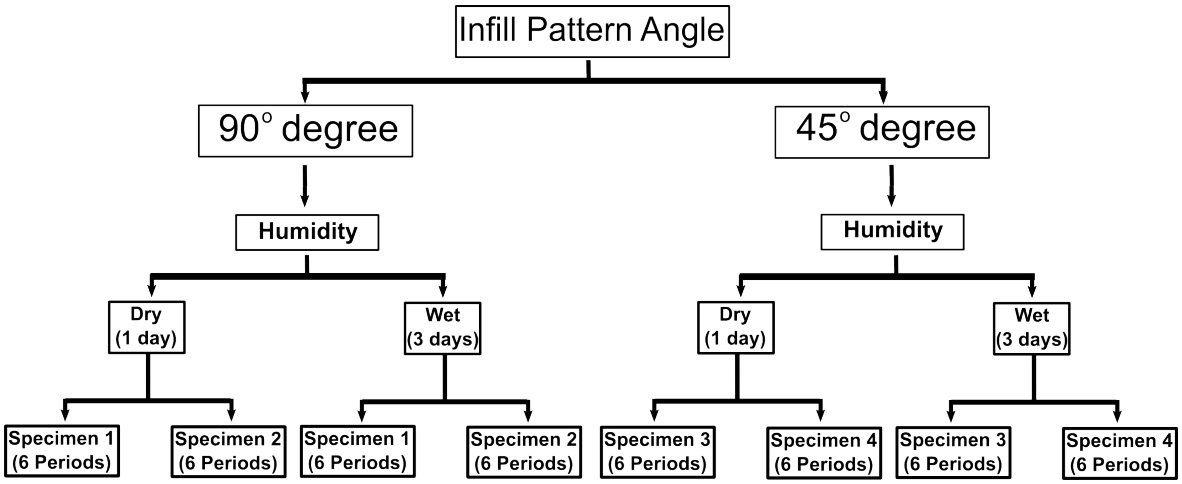

Figure 5.1: ECF characterization of H_2O concentration effects over electric resistance in printed specimens, study design

.

The experiment includes two factors, the *Infill Pattern Angle* and *Humidity* . The Infill Pattern Angle indicates the angle each infill line is drawn while printing the specimen. Figure 4.8 shows pattern angles on a printed part. The $90°$infill pattern angle (fig. 4.8 a and b) changes between perpendicular lines at each layer. The infill pattern angle of $45°$infill also changes between perpendicular lines but on the diagonal compared with the orientation of the part (fig. 4.8 c, d). The infill pattern is set as "Rectilinear" print parameter. All specimens were printed with 100% infill. The *Humidity* factor refers to dry and water-submerged cycles. From observations, the dry cycle was set to one day, while the water-submerged cycle set to three days. Two specimens for each $Humidity$ factor level are printed per each of the infill pattern angles, a total of four specimens. Each specimen is subject to six dry-wet cycles producing a total of twelve observations per specimen for each of the infill patter angle factor levels. The experiment is conducted using specimens of the PGM3D GPLA-C/Z2W ZY material. This material is the closest match between the reported resistivity by the manufacturer and the resistivity obtained by our experimental methods ($1\Omega-cm$ manufacturer vs $0.9747\Omega-cm$ experimental).

The statistical model is given in equation 5.1.

$$Y_{ijk} = \mu + \tau_i + \beta_j + \gamma_{ij} + \epsilon_{ijk} \tag{5.1}$$

where

Y = Dependent variable. Response is measured as resistance (Ω)

μ = Overall mean response

τ = Infill Pattern Angle factor (independent variable), with $i = 1..2$ (45 or 90 $degrees$)

β = Humidity factor (independent variable), with $j = 1..2$ (Dry, Wet)

γ = Interaction between Infill Pattern Angle and Condition

ϵ = Error

The null hypotheses for the experiment are:

- $H_{angle} : \tau_1 = \tau_1 = 0$;
- $H_{humidity} : \beta_1 = \beta_2 = \beta_3 = 0$;
- $H_{interaction} : \gamma_{11} = \gamma_{12} = \gamma_{21} = \gamma_{22} = 0$;

With confidence level $\alpha = 0.05$, the experiment tested whether there is a significant effect of the infill pattern angle and/or humidity factors including their interaction.

5.2 Test Subjects

A total of twelve test subjects units were printed (2 Infill Pattern Angle x 2 Humidity levels x 3 replicas) on the anisotropy direction A (fig 4.1, left) using the PGM3D GPLA-C/Z2W ZY material. This material was the closest match between the reported resistivity by the manufacturer and the resistivity obtained by our experimental methods ($1\Omega-cm$ manufacturer vs $0.9747\Omega-cm$ experimental). The geometry of the test subjects is shown in figure 3.2 (75mm length x 6mm width x 4mm height). The test subjects were printed as described in section 4.1. The print parameters are listed in table 4.1. The reason for choosing the same geometry and printing parameters from previous experiments is traceability. Large data have been collected

on this ECF material. Therefore, comparisons on water absorption on this material was facilitated. Two additional test subjects were printed and used as control units. One of these control subjects was placed under a controlled laboratory condition and its electric resistance was daily measured. The second control subject was placed under water during 27 consecutive days. The equipment calibration and ambient conditions were as in section 4.2. The handling of the test subjects described in section 3.3 was used. The dimensions of the test subjects were registered using a digital caliper and their mass recorded after a dry and water-submerged cycle using an Ohaus Adventurer Pro balance. Three consecutive mass readings were taken and their average calculated.

5.3 Material and Methods

Measuring System 7 was selected for this experiment (table 2.2). The system consists of a Keithley 2000 Benchtop Multimeter and Kelvin alligator probes for a 4-point electrode measuring setup. Test subjects were printed in a single session. The infill pattern angle was printed at randomly selected locations on the print bed (non-positioning pattern). The test subjects were coded and labeled. Before the experiment started, the test subjects were masked and stored in anti-static bags with desiccant packs.

After been under water, it was observed that a test subject produced a noticeable change in its electric resistance after one hour. However, after that hour and during seven days, the electric resistance presented no noticeable change. With the purpose of removing the absorbed water on the material, the test subjects were placed in a dehydration oven surrounded by silica pebbles ($1 - 5mm$ gel beads size silicon dioxide). The water-submerged period was chosen to be 72 hours and the dry period 24 hours. Since the temperature of the test subjects came out above the laboratory ambient average temperatures, each dry period was followed by 12 hours of conditioning. Therefore, each cycle consisted of $24hrs_{Dry} + 12hrs_{Conditioning} + 72hrs_{WaterSubmerge}$.

The experiment started by removing the test subjects from the anti-statics bags and placing them in an open container for the laboratory conditioning period of 12 hours. They were considered initially dry since they had not been on the water-submerged cycle yet. Then, their electric resistance and mass were measured. The test subjects were placed into tubes with $15ml$

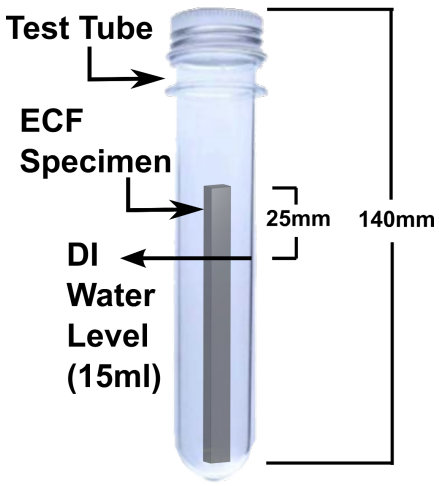

Figure 5.2: Test tubes setup for H_2O absorption experiment over electric resistance in ECF printed specimens

of Deionized Water (DI) at room temperature. They were randomly oriented in the tubes during the water-submerged periods. The water level in the tube left $25mm$ of the test subject outside the water level. Thus, producing a partial water submersion of the test subject (figure 5.2). The reason to leave a section above the water level was to allow for the connection of the electrodes on a dry zone.

After a water-submerged period of $72hrs$, the water was drained from the tube and the test subject was dried using an absorbent paper tower. Before measuring the electric resistance, the test subject was subject to a drying period of $1hr$. Its mass was also measured. The test subjects were then placed inside custom-designed 3D printed containers filled with $250gr$ of silicon dioxide gel beads of $1-5mm$ in size. The color blue in the silica indicates the dry state and the color pink the water saturation (dehydration period). Precautions were taken to not place the test subject at the bottom of the silica granulated material because it could potentially not contact the desiccant material. The test subject was placed for $24hrs$ in the dry oven (figure 5.4) set at $55°C$. After the drying period, the mass of the test subjects mass was collected and the conditioning period of $12hrs$ started. This period was needed because the test subjects after the dehydration period had a higher temperature than the surrounding environment. This situation could lead to higher electric resistance readings than at room temperature due to the heat expansion of the matrix PLA material that separates the conductive graphene nano-rods

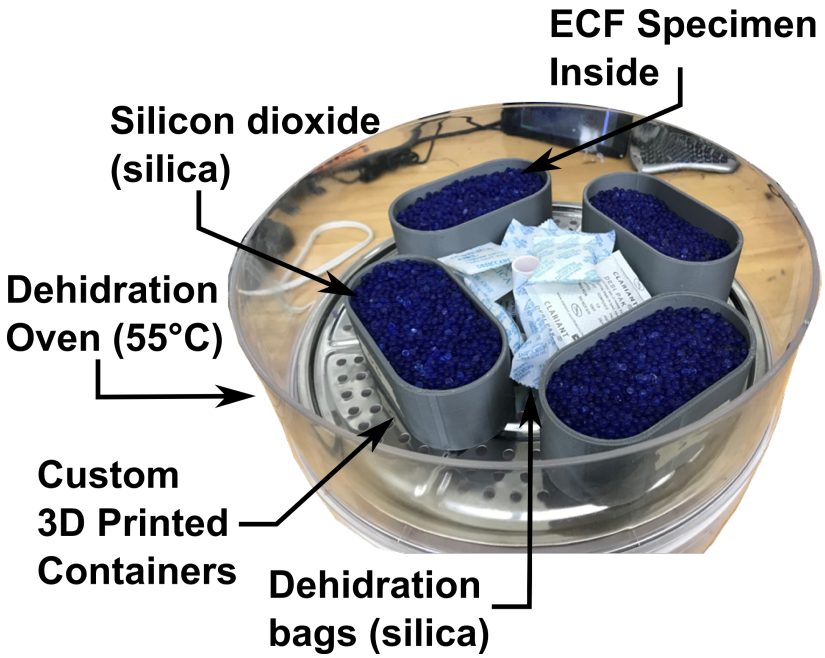

Figure 5.3: ECF specimens placed in dryer oven with silicon dehydration material after water-submersion period

(GNR) [[6]. After the conditioning period, the electric resistance measurements were saved and the test subjects placed back in the tubes using the same amount of DI water. A total of six $Dry - WaterSubmerged$ cycles were done providing six dry and six after water-submerged readings. While the test subjects remained underwater, the silica material was placed on the dehydration oven at $75°C$ for two days to remove the humidity absorbed from the test subjects during the previous dry period. Two days were enough for the silica material to come back to its blue color, indicating a dry state. The duration of the experiment was 27 days.

The dry-control subject was placed into an open container and left at laboratory conditions for the entire duration of the experiment. Daily measurements of its electric resistance were taken. The wet-control subject was placed under water using the same procedure as the test subjects. Except, it was only removed from the water at the end of the experiment. The electric resistance and mass measurements were recorded before and after the dry-control subject was submerged in the water.

Once the conditioning period of a test subject was complete, three resistance and mass measurements were registered and the average calculated.

Figure 5.4: PrintDry dehydration oven [5]

A custom fixture was designed and 3D printed for assuring repeatability of the electrode positioning. The fixture is described in the top-left corner of figure 5.5 (a). Visual markers allows for the test subject to be placed at the same location each time a measurement is taken. Kelvin alligator test leads hook into holders to provide adjustable height and orientation. Markers in the holders ensure that the test leads make contact with the test subject at the same location every time a measurement is taken.

The electric resistance measurements were taken "Off-Line", meaning that each measurement was taken after a dry period, or after the water-submerged period. No measurements of water absorption were taken during the experiment. The test subjects remained in the tube with DI water for the entire duration of the water-submerged period.

To understand the changes on resistance in real-time, additional readings were taken "On-Line". The test subjects were placed in a special container where the half section was submerged in water while both edges were outside the water for electrode placement (figure 5.5, b). Silicon gel was used to seal and avoid water contacting the electrodes. An edge of $12.5mm$ at each side of the test subject was left outside of the container. Figure 5.5(b) shows a test subject placed on the custom fixture during an off-line electric resistance reading. Figure 5.5 (c) shows a test subject during the additional readings. The test subjects are constantly connected to the measuring system for a total of $72hrs$ with on-line readings every hour while in the water.

A custom $C\#$ program ws written to send "Standard Commands for Programmable Instruments" (SCPI) to the Keithley 2000 DMM equipment through a serial port to control the

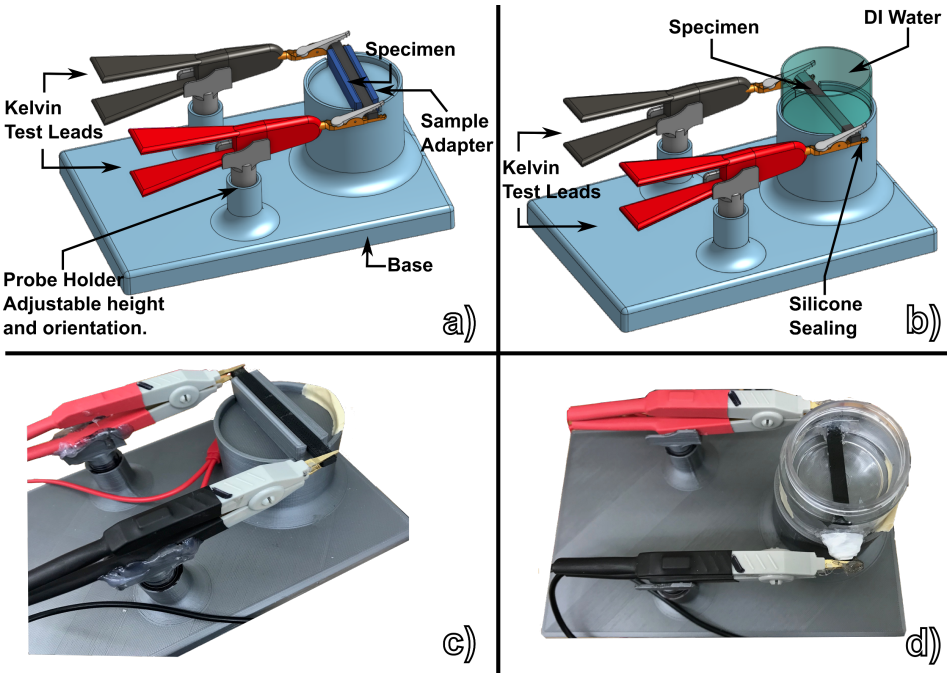

Figure 5.5: Custom 3D printed fixture for electric resistance measurement for water absorption experiment.

frequency of readings. When the system was not reading, the equipment was set by the program to the idle mode (DCV mode) to avoid any current to flow through the test subject. Data were captured in "Comma-separated Values" files (CSV). The test subjects also completed two additional periods of $72 hours$ of water-submersion to have more on-line readings.

5.4 Statistical Analysis

A two-factor analysis of variance (ANOVA) was performed using the Minitab software [46]. The test subjects were printed using the material PGM3D GPLA-C/Z2W ZY. The infill pattern angle and the humidity factors included two levels (90°and 45°, Dry and Wet, respectively). The interaction factor between the infill pattern angle and humidity was also included in the model. A confidence level 0.05 was considered significant. The plots of the residuals were used to determine the normality requirement of the model.

		90°Infill Pattern Angle				45°Infill Pattern Angle			
		Specimen 1		Specimen 2		Specimen 3		Specimen 4	
Cycle	**Period**	**Ohms (Avg)**	**Mass gr (Avg)**	**Ohms (Avg)**	**Mass gr (Avg)**	**Ohms (Avg)**	**Mass gr (Avg)**	**Ohms (Avg)**	**Mass gr (Avg)**
1	**Dry**	26.52283	2.28000	26.88767	2.23000	24.55900	2.28833	9.69244	2.28833
	Wet	30.09443	2.31267	30.03403	2.28033	30.96300	2.34400	11.86244	2.34433
2	**Dry**	27.00233	2.29433	26.39100	2.24669	27.52877	2.29700	10.69082	2.29267
	Wet	31.49717	2.32433	29.62560	2.29114	30.56560	2.34133	11.73269	2.34467
3	**Dry**	28.26207	2.29550	26.99533	2.24040	26.13237	2.29267	10.22181	2.28833
	Wet	29.95323	2.31950	30.17887	2.30060	28.85183	2.35167	11.16803	2.35167
4	**Dry**	26.40827	2.30100	26.87633	2.24551	25.44867	2.28954	9.99457	2.29133
	Dry	28.52964	2.31330	28.89667	2.30477	27.83270	2.34714	10.82820	2.34200
5	**Dry**	25.91870	2.30240	25.97573	2.25240	24.94730	2.29330	9.83100	2.29067
	Wet	28.14517	2.32030	28.68297	2.31770	27.60510	2.35069	10.75783	2.33167
6	**Dry**	25.59110	2.30550	25.83300	2.25660	24.93297	2.29779	9.82912	2.28767
	Wet	27.47467	2.31774	28.20767	2.31050	26.89933	2.34331	10.51771	2.33833

Table 5.1: $Dry - WaterSubmersion$ cycles data for PGM3D GPLA-C/Z2W material specimens

Analysis of Variance	**PGM3D GPLA-C/Z2W ZY**				
Source	**DF**	**Adj SS**	**Adj MS**	**F-Value**	**P-Value**
Condition	1	135.821	135.821	104.99	0.000
Infill Angle Pattern	1	6.356	6.356	4.91	0.032
Condition*Infill Angle Pattern	1	4.961	4.961	3.83	0.057
Error	44	56.922	1.294		
Total	47	204.060			

Table 5.2: Analysis of Variance (ANOVA) for infill pattern angle and condition ($Dry - WaterSubmerge$) using PGM3D GPLA-C/Z2W material specimens

5.5 Experimental Results

The data collected during the experiment are shown in Table 5.1. The data show the average electric resistance after each cycle and period. The ANOVA results are presented in Table 5.2. The table shows that for an $\alpha = 0.05$ the p-value of the Infill Pattern Angle and Humidity is lower than α, indicating that there is significant evidence that changes on either of these factors changes the resistance of the ECF material. However, there is no significant evidence that the interaction of these two factors effects the resistance. The plots for the residuals presented in figure 5.6 validated the normality assumption of the error terms of the model.

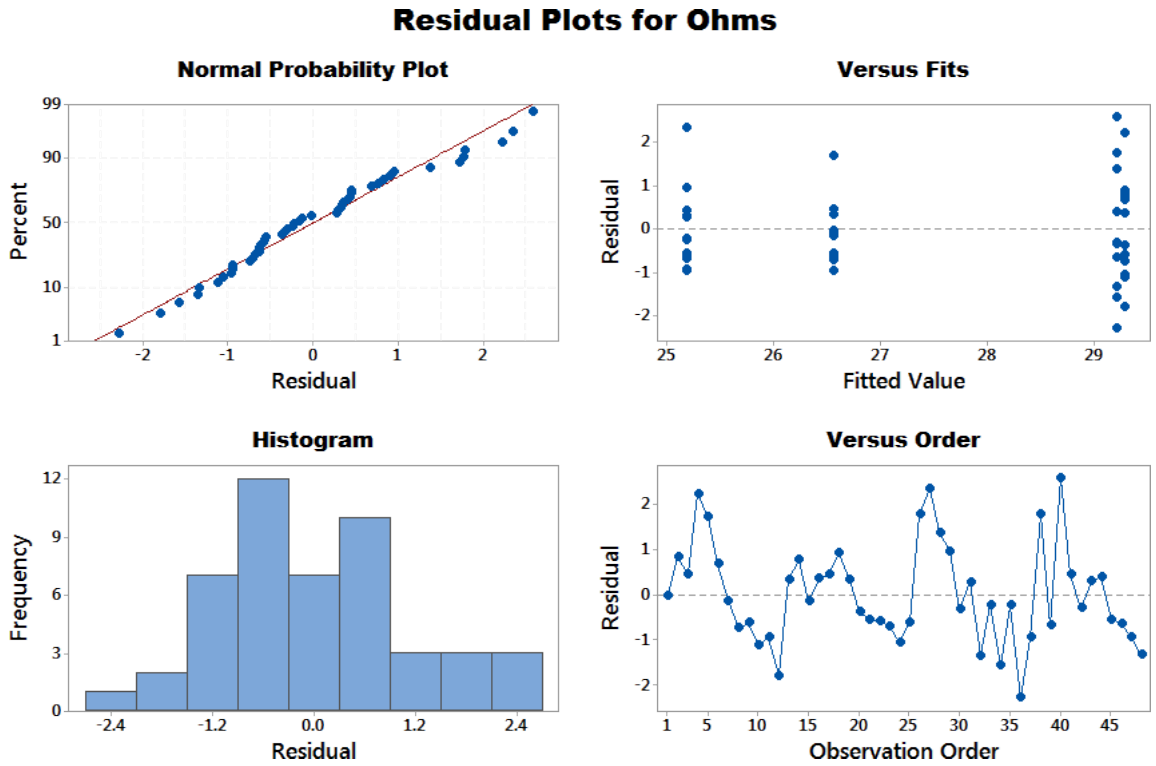

Figure 5.6: Residuals plots for Ohms, PGM3D GPLA-C/Z2W

Since the Humidity factor relates to the mass due the absorption of the water molecules, a distribution plot is presented in figure 5.7. The X axis presents the average mass in grams of the test subjects and the Y axis presents the electric resistance during the $Dry-WaterSubmerged$ cycles. The plot shows a clear differentiation between both conditions. On the left of the plot, the readings correspond to the dry periods with lower values. On the right, the readings correspond to after the $WaterSubmerged$ periods. An increase on the mean value of 10% between the $Dry - WaterSubmerged$ cycles was observed.

From the perspective of the cycles, figure 5.8 shows in the Y axis the average electric resistance over all test subjects and in the X axis the days. Each low value corresponds to a measurement after a Dry period and each high value corresponds to a measurement after a $WaterSubmerged$ period.

From the additional captured data, figure 5.9 presents the average of two $WaterSubmerged$ periods of $72hrs$. The data are captured using a custom $C\#$ program connected through serial port to the DMM equipment (SCPI commands), and saved in CSV files. The readings were taken every hour with the equipment in idle mode during intervals (DCV mode). The X axis

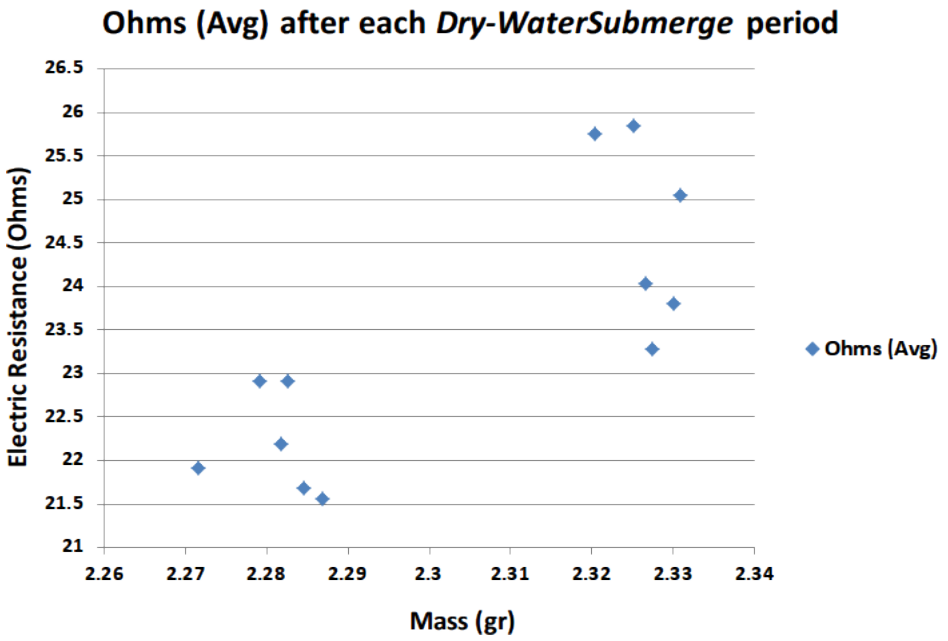

Figure 5.7: Dispersion plot for electric resistance measurements after each $Dry - WaterSubmerge$ period

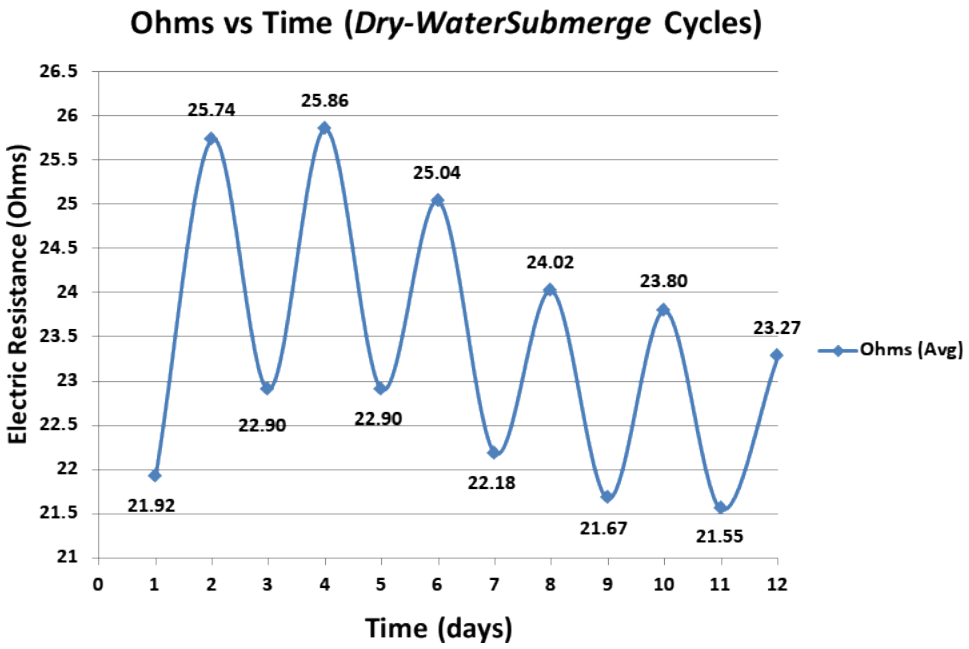

Figure 5.8: $Dry - WaterSubmerge$ cycles, PGM3D GPLA-C/Z2W material

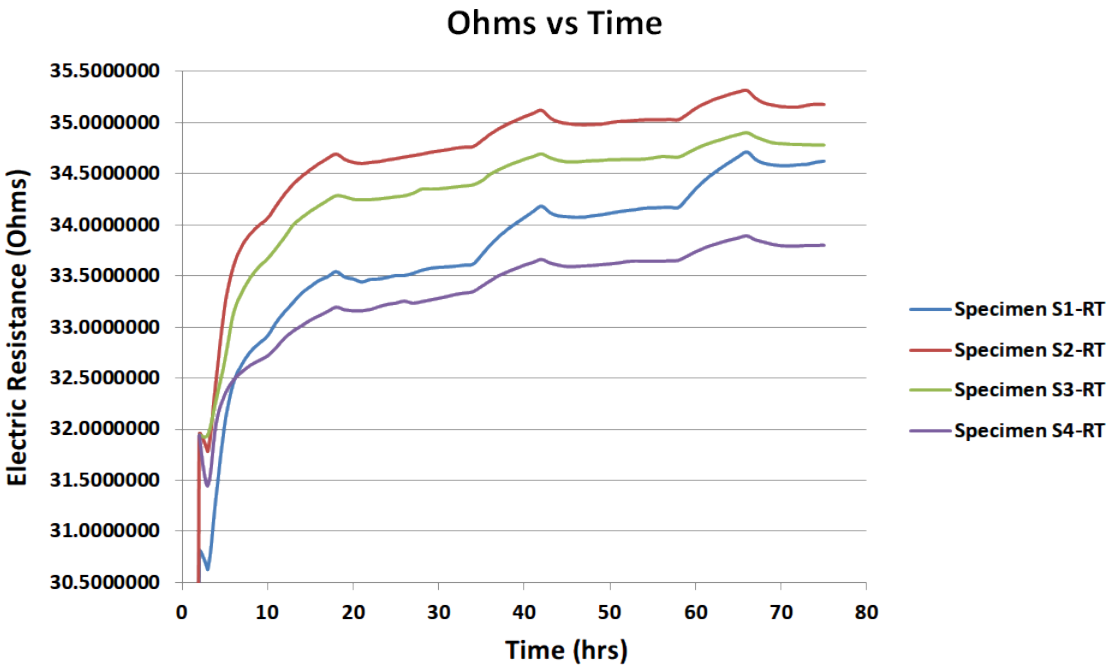

Figure 5.9: On-Line electric resistance measurements, average per specimen, $72hrs$ time-frame

represents time in hours and the Y axis represents the electric resistance for the $Humidity$ factor ($Dry - WaterSubmerged$ cycles). The data show a rapid increment in the electric resistance during the first $10hrs$ and keeps increasing at lower rate.

Average of the "On-Line" data was calculated for each specimen. The initial value was subtracted to allow all curves start at the same origin (0). This is necessary because each specimen have a slightly different initial value. The average curve for all specimens is presented in figure 5.10.

The data presented in the previous two plots correspond to the "On-Line" readings, where the specimen was permanently connected to the DMM equipment for the whole time of the $WaterSubmerged$ period.

Figure 5.11 presents the electric resistance captured data for the dry control specimen. This specimen was never conditioned to $WaterSubmerged$ periods and therefore, as expected, it presents a variability of less than 1%.

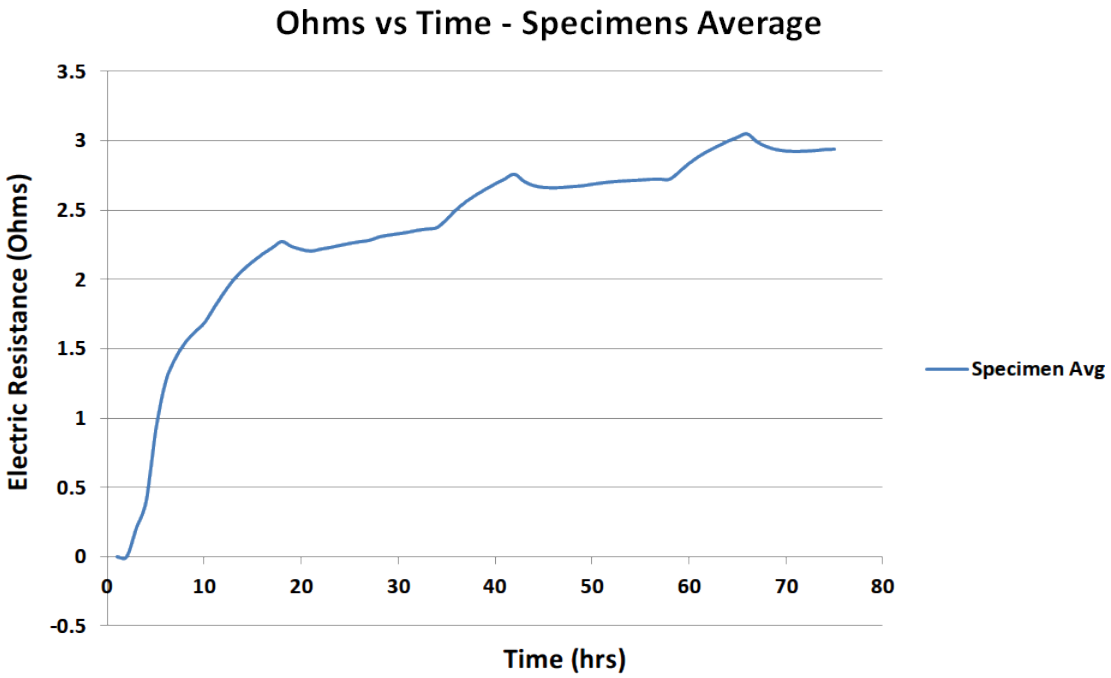

Figure 5.10: On-Line electric resistance measurements average curve

In figure 5.12, the effect of water absorption over longer periods of time on a control specimen of the same material is shown. Notice that even after 5 days, there is still a slow increment in the electric resistance. The effect seems to stabilize around day 7.

Figure 5.13 presents the research conducted by [6], where the micro structure of the graphene nano rod (GNR) can be observed. Images were obtained by a "Field Emission Surface Electron Microscopy" (F-SEM). The conductive nano rods spreads randomly through the PLA matrix material. When water molecules are absorbed by the PLA binding material they increase the volume of the polymer, separating the nano rods and reducing the number in contact. A similar phenomenon is observed when the $graphene + PLA$ composite material is used as temperature sensor [6].

5.6 Conclusions

The ANOVA results indicated that Humidity is the factor with higher contribution to the electric resistance. The experiment showed that the electric resistance produces a detectable cycling change over time. The mean increased 10% between $Dry - WaterSubmerged$ cycles. The reason is that clean water is a very good insulator. It is with the mix of salts and other elements

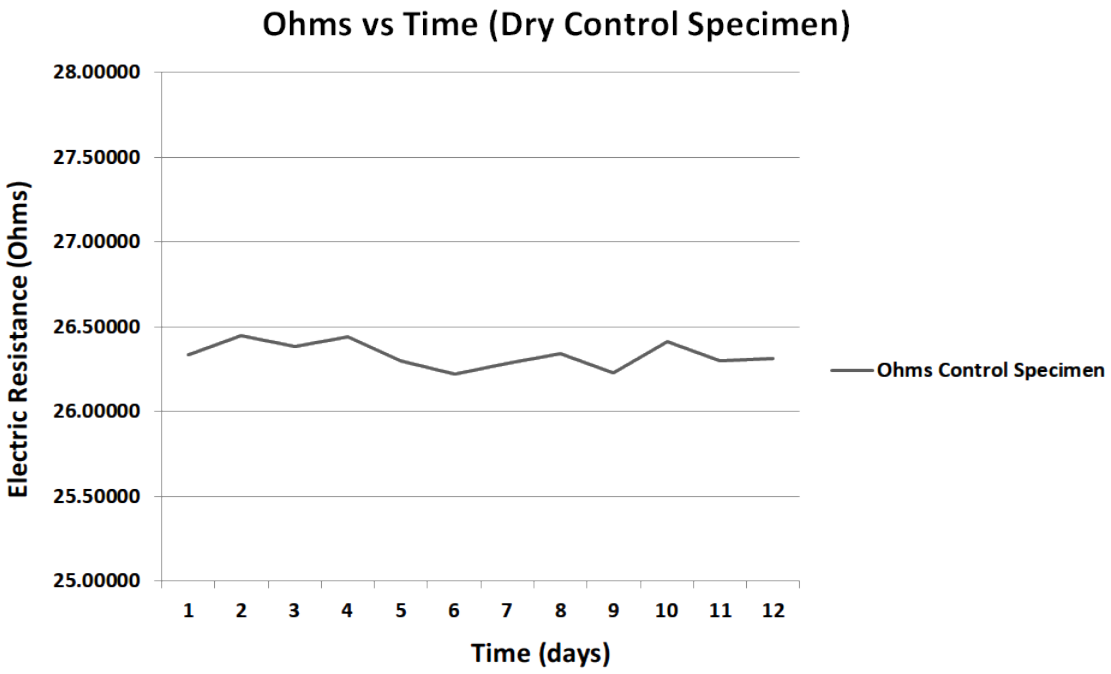

Figure 5.11: Wet control specimen, PGM3D GPLA-C/Z2W material

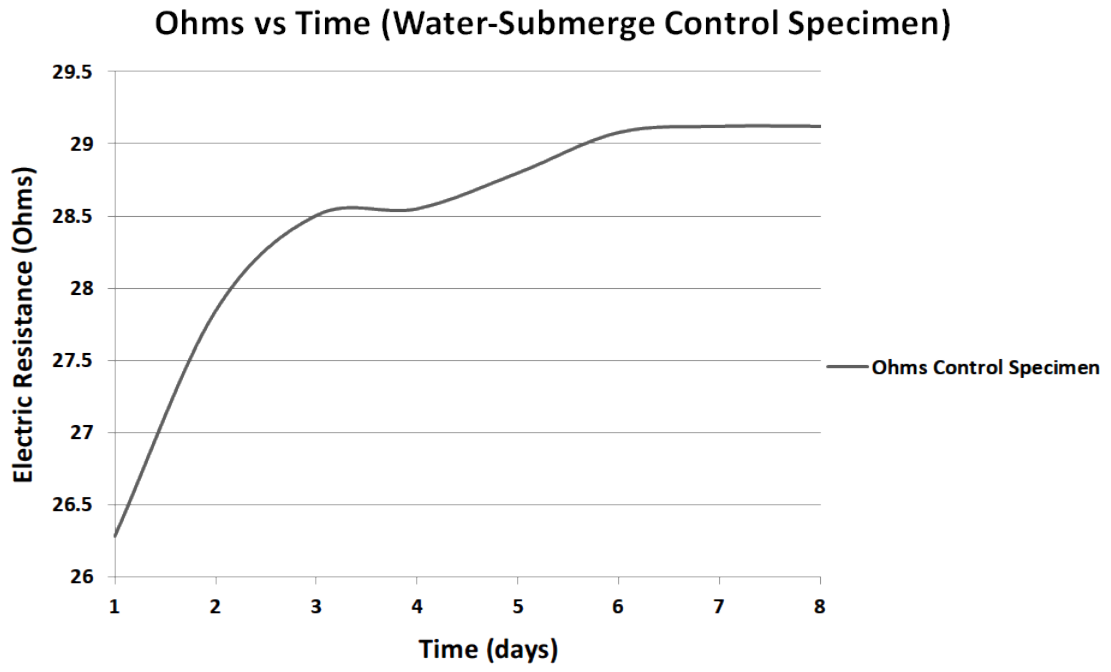

Figure 5.12: Dry control specimen, PGM3D GPLA-C/Z2W material

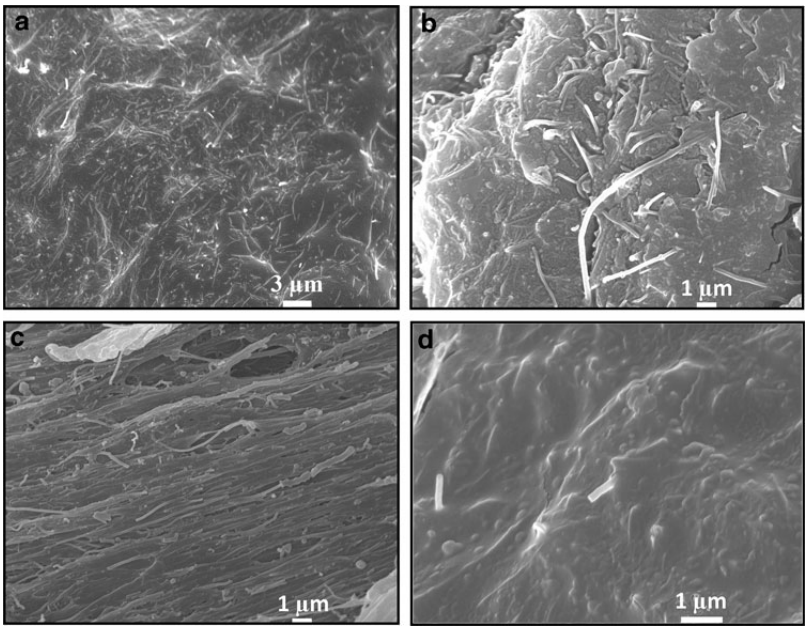

Figure 5.13: FE-SEM images showing morphology at different magnifications of (a) filament surface before printing, (b) filament cross section before printing, (c) filament surface after printing, and (d) filament cross section after printing. FE-SEM, field emission surface electron microscopy [6]

is when water becomes conductive. Some resistance reductions over time were observed. They may be had been produced by inconsistencies in the drying process or dehydration equipment. If the test subject does not dehydrate at the same level as in the previous cycle, the subsequent water absorption could accumulate and alter the initial state. Small variations on the volume of water could also had introduced some noise into the readings. In addition, the material capability to absorb water molecules could have decreased over time. Further experiments are needed to improve the control of ambient variables and to expand the time frame of the experiment. The results showed a rapid increment in the electric resistance response during the first ten hours. The effect kept increasing but at a much lower rate. Water saturation started after day 6. Ideally, the wet-control subject should have been submerged for the whole duration of the experiment. But problems with the container allowed the collection of valid data only until day 8. More experiments are needed to properly identify the extreme point of water saturation when the ECF material is no longer able to absorb water molecules or the change on the electric resistance is no longer detectable. Additional data were captured at two readings per second.

It was possible to detect a stable increase on the electric resistance response of 0.005Ω in only $60seconds$. The experiment showed that the PGM3D GPLA-C/Z2W material can potentially be used as a humidity sensor. The basic form of use could be as a discrete sensor, detecting the presence or absence of water on the immediate surrounding of the material. Also, the water absorption curve was smooth enough to define segments where the absorbed humidity can fit into detectable ranges. In the water absorption curve, ridges were observed. These ridges appeared periodically during the reading period and seem to indicate times in which the material absorbed more water and little later somehow released it. This effect is intriguing since the material is constantly submerged in water and therefore, there is no way that part of the absorbed water could have been released. The measuring system was discarded as the source of these ridges. The instrument did not introduce any current or voltage into the test subjects while the instrument was not reading the electric resistance. It is unlikely that the ridges were produced in fact by a sudden and periodical phenomenon of the ECF material. Rather it could have been produced by a cyclic effect of the connected equipment. The temperature cycles could also have introduced noise to the readings. To explain and eliminate this issue, it is suggested that further experiments be done by introducing additional equipment and compare the readings. Such measuring system should completely disconnect the electrodes from the specimen after each reading but still accumulate large periods of time at high frequency (automated setup). It is also suggested to switch the time in which the water-submerged periods occurs. This process could eliminate cyclic changes in the ambient temperature. In general, a more control of the temperatures of the water, specimens, and containers is also recommended.

Chapter 6

Future Work

Concerning the experiments in Chapter 4, research studies have shown that the distribution of the graphene nanorods in a Graphene+PLA composite material affects its electrical conductance property. A path of connected nanorods is limited to conduct a maximum amount of current and having parallel-connected paths of nanorods can allow more current to flow through the material. To ensure enough nanorods to produce conductive paths, the manufacturer determines the proportion of GNW and PLA binding matrix. The extrusion and melting process of the FDM printing creates more alignments of nanorods and therefore the resistivity property of the printed part changes. In addition, a printed part of higher density creates more aligned nanorods. More research need to be done to model the changes on resistivity of the material after the FDM printing. In addition, increasing the infill-percent factor levels can help to relate the resistance with the density of the nanorods and understand the extreme capabilities of the material (lower and higher resistance). The two anisotropic direction produced by the FDM process resulted in specimens that presented different electric resistance properties depending on their axis orientation. To improve the electric resistance reading in the anisotropic direction B (along the Z-axis), new specimens should be printed having the same shape as the specimens used in chapter 4 but using the length as the height for the new specimen. This new experiment can allow a direct comparison between the two anisotropic directions. The same new experiment using different levels of infill can be performed with the new specimens for a full characterization of the material in term of its electric resistance property.

Concerning the experiments presented in chapter 5, when the Graphene+PLA material is used as a humidity sensor, the water changes the morphology of the polymer matrix holding

the conductive graphene nanorods. Once the PLA starts absorbing the water, the matrix expands and the conductivity reduces due to the drop in the active contacts. After drying, the material returns to its initial matrix and the contacts are restored to their initial form. Because of temperature restrictions of the PLA, the maximum operation temperature of the sensor is limited to $70°C$. Beyond that, there will be a permanent deformation of the matrix and the resistance will not return to its original value. Moreover, the glass transition temperature of the PLA is near $58°C$. Therefore, the recommended operation temperature of the sensor is below $60°C$ to ensure stable results and low hysteresis. In addition, more experiments are needed to properly identify the extreme point of the water saturation of the ECF material. That is when the sensor is no longer able to absorb water molecules or detect a change on the electric resistance. Similarly, for the dry state, the water concentration can be extracted from the specimens using specialized equipment. Knowing the minimum levels of water molecules concentration in the material can help to implement a better drying process where the material roll back to the exact initial dry state. Since small variations on the volume of water could also had introduced some error in the readings, water level sensors and an active control system should be used to control the water volume and temperature. In addition, the material capability to absorb water molecules could have decreased over time. Additional studies over extended periods are needed to better understand this phenomenon. When obtaining the water absorption curve, some ridges were observed. These ridges appeared periodically during the reading period and seem to indicate times in which the material absorbed more water molecules and later somehow released them. Since the absorbed water molecules could not possible have been released while the specimen was under water, additional experiments need to be done to understand this effect. The temperature cycles could also have introduced errors to the readings. To eliminate these issues, further experiments need to be done by using a different measuring system. Such measuring system should completely disconnect the electrodes from the specimen after each resistance reading but still accumulate large periods of readings at high frequency.

Bibliography

[1] ASTM International, "ASTM D991-89, Standard Test Method for Rubber Property-Volume Resistivity Of Electrically Conductive and Antistatic Products," 2019, [Online; accessed 14-Jan-2018]. [Online]. Available: https://compass.astm.org/Standards/WITHDRAWN/D6054.htm

[2] Interlink Electronics, "FSR 406 Force Sensing Resistor," 2019, [Online; accessed 30-March-2019]. [Online]. Available: https://www.interlinkelectronics.com/fsr-406

[3] 3DFuel, "DynaPurge 3D Clean," 2019, [Online; accessed 3-April-2019]. [Online]. Available: https://www.3dfuel.com/products/dyna-purge-3d-clean

[4] Adventurer, "Adventurer AV114," 2018, [Online; accessed 9-June-2018]. [Online]. Available: https://dmx.ohaus.com/WorkArea/downloadasset.aspx?id=2218

[5] PrintDry, "PrintDry - Filament Drying System," 2019, [Online; accessed 8-August-2019]. [Online]. Available: https://www.matterhackers.com/store/l/printdry-filament-drying-system/sk/MNXQRWQC

[6] M. Sajid, J. Z. Gul, S. W. Kim, H. B. Kim, K. H. Na, and K. H. Choi, "Development of 3d-printed embedded temperature sensor for both terrestrial and aquatic environmental monitoring robots," *3D Printing and Additive Manufacturing*, vol. 5, no. 2, pp. 160–169, 2018.

[7] J. L. Morse, "Design of a gage r & r experiment for a basic manufacturing processes course," Ph.D. dissertation, Auburn University, 1996.

[8] J. G. Webster, *Electrical Measurement, Signal Processing, and Displays*. CRC Press, 214, vol. 1.

[9] A. E. Shahat, *Electrical Resistivity and Conductivity*. Intech, 2017, vol. 1.

[10] M. Zenkiewicz, J. Richert, P. Rytlewski, and A. Richert, "Selected electrical and thermal properties of polylactide/graphite composites," *Polimery*, vol. 56, no. 6, pp. 489–493, 2011.

[11] H. Gao, "Exploring the manufacturability and resistivity of conductive filament used in material extrusion additive manufacturing," Ph.D. dissertation, Pennsylvania State University, 2017.

[12] M. Ibrahim, Y. Mogan, and S. S. J. andRaveverma Periyasamy, "Resistivity study on conductive composite filament for freeform fabrication of functionality embedded products," 2006.

[13] ASTM International , "ASTM D4496-13, Standard Test Method for D-C Resistance or Conductance of Moderately Conductive Materials," 2018, [Online; accessed 25-June-2018]. [Online]. Available: https://www.astm.org/Standards/D4496.htm

[14] C. F. Coombs and H. T. Holden, *Printed circuits handbook*. McGraw-Hill New York, 2001, vol. 1.

[15] B. Matisoff, *Handbook of electronics manufacturing engineering*. Springer Science & Business Media, 2012.

[16] D. L. Linne, G. B. Sanders, S. O. Starr, D. J. Eisenman, N. H. Suzuki, M. S. Anderson, T. F. O'Malley, and K. R. Araghi, "Overview of nasa technology development for in-situ resource utilization (isru)," *NASA*, 2017.

[17] G. B. Sanders, "Overview of past lunar in situ resource utilization (isru) development by nasa," *NASA*, 2018.

[18] D. L. Linne, G. Sanders, N. Suzuki, D. Eisenman, P. Hintze, K. Araghi, and T. O'Malley, "Current activities in the advanced exploration systems isru project," *NASA*, 2018.

[19] C. M. S. et al., "3d printing multi-functionality: Embedded rf antennas and components," *Antennas and Propagation (EuCAP), 2015 9th European Conference*, vol. 9, pp. 1–5, 2015.

[20] E. M. D. Espalin, D. W. Muse and R. B. Wicker, "3d printing multifunctionality: structures with electronics," *Int. J. Adv. Manuf. Technol.*, vol. 72, pp. 963–978, 2014.

[21] Voxel8, "3D Electronics Printing," 2015, [Online; accessed 15-Dec-2018]. [Online]. Available: http://www.voxel8.co/

[22] Y. Xu, X. Wu, X. Guo, B. Kong, M. Zhang, X. Qian, S. Mi, and W. Sun, "The boom in 3d-printed sensor technology," *Sensors*, vol. 17, no. 5, p. 1166, 2017.

[23] J. Ou, G. Dublon, C.-Y. Cheng, F. Heibeck, K. Willis, and H. Ishii, "Cilllia: 3d printed micro-pillar structures for surface texture, actuation and sensing," in *Proceedings of the 2016 CHI Conference on Human Factors in Computing Systems*. ACM, 2016, pp. 5753–5764.

[24] M. Saari, B. Xia, B. Cox, P. S. Krueger, A. L. Cohen, and E. Richer, "Fabrication and analysis of a composite 3d printed capacitive force sensor," *3D Printing and Additive Manufacturing*, vol. 3, no. 3, pp. 136–141, 2016.

[25] S.-z. Guo, X. Yang, M.-C. Heuzey, and D. Therriault, "3d printing of a multifunctional nanocomposite helical liquid sensor," *Nanoscale*, vol. 7, no. 15, pp. 6451–6456, 2015.

[26] Multi3D, "Multi3D - Electrifi," 2018, [Online; accessed 8-June-2018]. [Online]. Available: https://www.multi3dllc.com/about-electrifi/

[27] Functionalize, "Functionalize - F-Electric," 2018, [Online; accessed 8-June-2018]. [Online]. Available: http://functionalize.com/about/functionalize-f-electric-highly-conductive-filament/

[28] BlackMagic3D, "BlackMagic3D - Conductive Graphene PLA," 2018, [Online; accessed 8-June-2018]. [Online]. Available: https://www.blackmagic3d.com/Conductive-p/grphn-pla.htm

[29] PMG3D, "PMG3D - GraphenePLA (GPLA-C/Z2W ZY)," 2018, [Online; accessed 8-June-2018]. [Online]. Available: http://www.pmg3d.com/en/English/Materials/GraphenePLA/2016/0608/130.html

[30] ProtoPasta, "ProtoPasta - Composite PLA," 2018, [Online; accessed 8-June-2018]. [Online]. Available: https://www.proto-pasta.com/pages/conductive-pla

[31] Test Equipment Depot, "A Guide to Low Resistance Testing," 2019, [Online; accessed 3-April-2019]. [Online]. Available: http://www.testequipmentdepot.com/megger/pdf/low-resistance-testing.pdf

[32] Tektronix, "Keithley 2000 DMM," 2018, [Online; accessed 9-June-2018]. [Online]. Available: https://openlab.ece.illinois.edu/assets/pdf/manuals/Keithley2000Manual.pdf

[33] CenTech, "CenTech P37772 DMM," 2018, [Online; accessed 9-June-2018]. [Online]. Available: https://manuals.harborfreight.com/manuals/61000-61999/61593.pdf

[34] Klein Tools, "Klein Tools MM200 DMM," 2018, [Online; accessed 9-June-2018]. [Online]. Available: http://www.telmark.pe/pdf/MM200.pdf

[35] UNI-T, "UNI-T UT61-E," 2018, [Online; accessed 9-June-2018]. [Online]. Available: https://www.batronix.com/downloads/UNI-T/UT61_Manual.pdf

[36] Agilent, "Agilent E3633A," 2018, [Online; accessed 9-June-2018]. [Online]. Available: https://www.matsolutions.com/Portals/0/Product%20documents/Agilent%20Technologie//E3634A/E3634A%20User%27s%20Guide.pdf

[37] A. Sahay and M. B. Belt, "Measurement system analysis gage repeatability & reproducibility (gage r&r) study," *Six Sigma Quality: Concepts & Cases*, vol. 1, 2010.

[38] R. Sloop, "Understand gage r&r," *Quality*, vol. 48, no. 9, p. 44, 2009.

[39] ASTM International, "ASTM B193-16, Standard Test Method for Resistivity of Electrical Conductor Materials," 2018, [Online; accessed 1-June-2018]. [Online]. Available: http://www.astm.org/cgi-bin/resolver.cgi?B193-16

[40] ASTM International, "ASTM 618-13, Standard Practice for Conditioning Plastics for Testing," 2019, [Online; accessed 1-June-2018]. [Online]. Available: https://www.astm.org/Standards/D618

[41] PanaViseBuddyJr207, "PanaVise Buddy Jr 207," 2019, [Online; accessed 30-March-2019]. [Online]. Available: https://www.panavise.com/index.html?pageID=1&page=full&--eqskudatarq=227

[42] PanaVise366, "PanaVise 366," 2019, [Online; accessed 30-March-2019]. [Online]. Available: https://www.panavise.com/index.html?pageID=1&page=full&--eqskudatarq=15

[43] P. R. M. Enkiewicz, J. Richert and A. Richert, "Selected electrical and thermal properties of polylactide/graphite composites," *Polimery*, vol. 56-6, no. 6, pp. 489–493, 2011.

[44] O-Basf, "Thermoplastic Polyurethane Elastomers," 2017, [Online; accessed 30-March-2019]. [Online]. Available: http://www.polyurethanes.basf.de/pu/solutions/en/function/conversions:/publish/content/group/Arbeitsgebiete_und_Produkte/Thermoplastische_Spezialelastomere/Infomaterial/elastollan_material_uk.pdf

[45] Arduino, "Arduino Mega 2650," 2019, [Online; accessed 30-March-2019]. [Online]. Available: https://store.arduino.cc/usa/mega-2560-r3

[46] Minitab, "Minitab 18," 2019, [Online; accessed 3-April-2019]. [Online]. Available: http://www.minitab.com/en-US/default.aspx

[47] Prusa Research, "Prusa i3 MK2S," 2018, [Online; accessed 9-June-2018]. [Online]. Available: https://shop.prusa3d.com/en/3d-printers/53-original-prusa-i3-mk2s-3d-printer.html

[48] Simplify3D, "Simplify3D," 2018, [Online; accessed 10-June-2018]. [Online]. Available: https://www.simplify3d.com/

[49] L. M. Galantucci, I. Bodi, J. Kacani, and F. Lavecchia, "Analysis of dimensional performance for a 3d open-source printer based on fused deposition modeling technique," *Procedia CIRP*, vol. 28, pp. 82–87, 2015.

[50] P. Dudek, "Fdm 3d printing technology in manufacturing composite elements," *Archives of Metallurgy and Materials*, vol. 58, no. 4, pp. 1415–1418, 2013.

[51] T. Finnes, "High definition 3d printing–comparing sla and fdm printing technologies," *The Journal of Undergraduate Research*, vol. 13, no. 1, p. 3, 2015.

[52] MerlinFw, "Merlin firmware P.I.D autotune," 2018, [Online; accessed 11-June-2018]. [Online]. Available: http://marlinfw.org/docs/gcode/M303.html

[53] National Instuments, "PID Theory Explained," 2019, [Online; accessed 3-April-2019]. [Online]. Available: http://www.ni.com/en-my/innovations/white-papers/06/pid-theory-explained.html

[54] AUSTTCOL, "PEAKMETER PM6530D," 2019, [Online; accessed 3-April-2019]. [Online]. Available: https://img.banggood.com/file/products/20160823220835MT6800%20English%20User%20Manual.pdf

[55] M. Jamshidian, E. A. Tehrany, M. Imran, M. Jacquot, and S. Desobry, "Poly-lactic acid: production, applications, nanocomposites, and release studies," *Comprehensive Reviews in Food Science and Food Safety*, vol. 9, no. 5, pp. 552–571, 2010.

[56] J. HUA, Z.-m. ZHAO, W. YU, and T.-h. WANG, "Mechanical properties and hygroscopicity of polylactic acid/wood-flour composite," *Journal of Functional Materials*, vol. 10, p. 009, 2011.

[57] R. A. Auras, L.-T. Lim, S. E. Selke, and H. Tsuji, *Poly (lactic acid): synthesis, structures, properties, processing, and applications*. John Wiley & Sons, 2011, vol. 10.

[58] K. H. Choi, M. Sajid, S. Aziz, and B.-S. Yang, "Wide range high speed relative humidity sensor based on pedot: Pss–pva composite on an idt printed on piezoelectric substrate," *Sensors and Actuators A: Physical*, vol. 228, pp. 40–49, 2015.

[59] M. Sajid, S. Aziz, G. B. Kim, S. W. Kim, J. Jo, and K. H. Choi, "Bio-compatible organic humidity sensor transferred to arbitrary surfaces fabricated using single-cell-thick onion membrane as both the substrate and sensing layer," *Scientific reports*, vol. 6, p. 30065, 2016.

[60] K. H. Choi, H. B. Kim, K. Ali, M. Sajid, G. U. Siddiqui, D. E. Chang, H. C. Kim, J. B. Ko, H. W. Dang, and Y. H. Doh, "Hybrid surface acoustic wave-electrohydrodynamic atomization (saw-ehda) for the development of functional thin films," *Scientific reports*, vol. 5, p. 15178, 2015.

[61] K. Karimov, M. Saleem, N. Ahmed, M. Tahir, M. Zahid, M. Sajid, and M. Bashir, "Effect of humidity on the nipc based organic photo field effect transistor," *Proceedings of the Romanian Academy*, vol. 10, 2015.

[62] E. Sauerbrunn, Y. Chen, J. Didion, M. Yu, E. Smela, and H. A. Bruck, "Thermal imaging using polymer nanocomposite temperature sensors," *physica status solidi (a)*, vol. 212, no. 10, pp. 2239–2245, 2015.

[63] M. Sajid, H. B. Kim, Y. J. Yang, J. Jo, and K. H. Choi, "Highly sensitive behp-co-meh: Ppv+ poly (acrylic acid) partial sodium salt based relative humidity sensor," *Sensors and Actuators B: Chemical*, vol. 246, pp. 809–818, 2017.

[64] H. B. Kim, M. Sajid, K. T. Kim, K. H. Na, and K. H. Choi, "Linear humidity sensor fabrication using bi-layered active region of transition metal carbide and polymer thin films," *Sensors and Actuators B: Chemical*, vol. 252, pp. 725–734, 2017.

[65] F. Zhang, Y. Zang, D. Huang, C.-a. Di, and D. Zhu, "Flexible and self-powered temperature–pressure dual-parameter sensors using microstructure-frame-supported organic thermoelectric materials," *Nature communications*, vol. 6, p. 8356, 2015.

[66] M. Sajid, A. Osman, G. U. Siddiqui, H. B. Kim, S. W. Kim, J. B. Ko, Y. K. Lim, and K. H. Choi, "All-printed highly sensitive 2d mos 2 based multi-reagent immunosensor for smartphone based point-of-care diagnosis," *Scientific reports*, vol. 7, no. 1, p. 5802, 2017.

[67] J. Yang, D. Wei, L. Tang, X. Song, W. Luo, J. Chu, T. Gao, H. Shi, and C. Du, "Wearable temperature sensor based on graphene nanowalls," *Rsc Advances*, vol. 5, no. 32, pp. 25 609–25 615, 2015.

[68] J. C. Yeo, C. T. Lim *et al.*, "Emerging flexible and wearable physical sensing platforms for healthcare and biomedical applications," *Microsystems & Nanoengineering*, vol. 2, p. 16043, 2016.

[69] N. Neella, V. Gaddam, K. Rajanna, and M. Nayak, "Negative temperature coefficient behavior of graphene-silver nanocomposite films for temperature sensor applications," in *2016 IEEE 11th Annual International Conference on Nano/Micro Engineered and Molecular Systems (NEMS)*. IEEE, 2016, pp. 329–332.

[70] N. A. Travlou, M. Seredych, E. Rodríguez-Castellón, and T. J. Bandosz, "Activated carbon-based gas sensors: effects of surface features on the sensing mechanism," *Journal of Materials Chemistry A*, vol. 3, no. 7, pp. 3821–3831, 2015.

[71] C.-Y. Lee, C.-H. Lin, and Y.-M. Lo, "Fabrication of a flexible micro temperature sensor for micro reformer applications," *Sensors*, vol. 11, no. 4, pp. 3706–3716, 2011.

[72] T. Vuorinen, J. Niittynen, T. Kankkunen, T. M. Kraft, and M. Mäntysalo, "Inkjet-printed graphene/pedot: Pss temperature sensors on a skin-conformable polyurethane substrate," *Scientific reports*, vol. 6, p. 35289, 2016.

[73] R. Pawlak, M. Lebioda, J. Rymaszewski, W. Szymanski, L. Kolodziejczyk, and P. Kula, "A fully transparent flexible sensor for cryogenic temperatures based on high strength metallurgical graphene," *Sensors*, vol. 17, no. 1, p. 51, 2017.

[74] V. B. S. W. H. W. S. d. W. G. F. H. Gnanasekaran K, Heijmans T, "3d printing of cnt- and graphene-based conductive polymer nanocomposites by fused deposition modeling," *Applied Materials Today*, 2017.

[75] C. C. Seepersad, "Challenges and opportunities in design for additive manufacturing," *3D printing and Additive Manufacturing*, vol. 1, no. 1, pp. 10–13, 2014.

[76] B. Khoda, "Process plan for multimaterial heterogeneous object in additive manufacturing," *3D Printing and Additive Manufacturing*, vol. 1, no. 4, pp. 210–218, 2014.

[77] P. Harrey, B. Ramsey, P. Evans, and D. Harrison, "Capacitive-type humidity sensors fabricated using the offset lithographic printing process," *Sensors and Actuators B: Chemical*, vol. 87, no. 2, pp. 226–232, 2002.

[78] S. Ali, A. Hassan, G. Hassan, J. Bae, and C. H. Lee, "All-printed humidity sensor based on graphene/methyl-red composite with high sensitivity," *Carbon*, vol. 105, pp. 23–32, 2016.

[79] E. García-Tuñon, S. Barg, J. Franco, R. Bell, S. Eslava, E. D'Elia, R. C. Maher, F. Guitian, and E. Saiz, "Printing in three dimensions with graphene," *Advanced Materials*, vol. 27, no. 10, pp. 1688–1693, 2015.

[80] W. L. Tham, B. T. Poh, Z. A. M. Ishak, and W. S. Chow, "Characterisation of water absorption of biodegradable poly (lactic acid)/halloysite nanotube nanocomposites at different temperatures," *Journal of Engineering Science*, vol. 12, p. 13, 2016.

[81] G. Yew, A. M. Yusof, Z. M. Ishak, and U. Ishiaku, "Water absorption and enzymatic degradation of poly (lactic acid)/rice starch composites," *Polymer Degradation and Stability*, vol. 90, no. 3, pp. 488–500, 2005.

[82] Y. Y. Leu and W. S. Chow, "Kinetics of water absorption and thermal properties of poly (lactic acid)/organomontmorillonite/poly (ethylene glycol) nanocomposites," *Journal of Vinyl and Additive Technology*, vol. 17, no. 1, pp. 40–47, 2011.

[83] F. Aranda-García, R. González-Núñez, C. Jasso-Gastinel, and E. Mendizábal, "Water absorption and thermomechanical characterization of extruded starch/poly (lactic acid)/agave bagasse fiber bioplastic composites," *International Journal of Polymer Science*, vol. 2015, 2015.

[84] J. V. Ecker, A. Haider, I. Burzic, A. Huber, G. Eder, and S. Hild, "Mechanical properties and water absorption behaviour of pla and pla/wood composites prepared by 3d printing and injection moulding," *Rapid Prototyping Journal*, 2019.

[85] J. Lin, Z. Peng, C. Xiang, G. Ruan, Z. Yan, D. Natelson, and J. M. Tour, "Graphene nanoribbon and nanostructured sno2 composite anodes for lithium ion batteries," *ACS nano*, vol. 7, no. 7, pp. 6001–6006, 2013.

[86] T. Sreeprasad, A. A. Rodriguez, J. Colston, A. Graham, E. Shishkin, V. Pallem, and V. Berry, "Electron-tunneling modulation in percolating network of graphene quantum dots: fabrication, phenomenological understanding, and humidity/pressure sensing applications," *Nano letters*, vol. 13, no. 4, pp. 1757–1763, 2013.

[87] A.-R. O. Raji, S. Salters, E. L. Samuel, Y. Zhu, V. Volman, and J. M. Tour, "Functionalized graphene nanoribbon films as a radiofrequency and optically transparent material," *ACS applied materials & interfaces*, vol. 6, no. 19, pp. 16 661–16 668, 2014.

[88] C. H. A. Wong and M. Pumera, "Highly conductive graphene nanoribbons from the reduction of graphene oxide nanoribbons with lithium aluminium hydride," *Journal of Materials Chemistry C*, vol. 2, no. 5, pp. 856–863, 2014.

[89] M. A. Cuiffo, J. Snyder, A. M. Elliott, N. Romero, S. Kannan, and G. P. Halada, "Impact of the fused deposition (fdm) printing process on polylactic acid (pla) chemistry and structure," *Applied Sciences*, vol. 7, no. 6, p. 579, 2017.

[90] C.-C. Qin, X.-P. Duan, L. Wang, L.-H. Zhang, M. Yu, R.-H. Dong, X. Yan, H.-W. He, and Y.-Z. Long, "Melt electrospinning of poly (lactic acid) and polycaprolactone microfibers

by using a hand-operated wimshurst generator," *Nanoscale*, vol. 7, no. 40, pp. 16 611–16 615, 2015.

[91] M. M. Nobrega, J. B. Olivato, C. M. Müller, and F. Yamashita, "Biodegradable starch-based films containing saturated fatty acids: thermal, infrared and raman spectroscopic characterization," *Polímeros*, vol. 22, no. 5, pp. 467–474, 2012.

[92] J. Jeon, H.-B.-R. Lee, and Z. Bao, "Flexible wireless temperature sensors based on ni microparticle-filled binary polymer composites," *Advanced Materials*, vol. 25, no. 6, pp. 850–855, 2013.

[93] V. Silverajah, N. A. Ibrahim, N. Zainuddin, W. M. Z. W. Yunus, and H. A. Hassan, "Mechanical, thermal and morphological properties of poly (lactic acid)/epoxidized palm olein blend," *Molecules*, vol. 17, no. 10, pp. 11 729–11 747, 2012.

List of Abbreviations

ABS Acrylonitrile Butadiene Styrene

AM Additive Manufacturing

$ANOVA$ Analysis of Variance

CAD Computer-aided design

$CASIC$ Advanced Science, Innovation and Commerce

CSV Comma-Separated Values

DI Deionized Water

DV Dependent Variable

ECF Electrically Conductive Filament

emf Electromotive force

ESD Electrostatic discharge

FDM Fused Deposition Modeling

$FE-SEM$ Field Emission Surface Electron Microscopy

GNR Graphene Nano Rods

GNW Graphene Nano Wires

IV Independent Variable

$MWCNT$ Multi-Walled Carbon Nano Tubes

PEI Polyetherimide

PID Proportional Integral Derivative

PLA Polylactic acid

$SCPI$ Standard Commands for Programmable Instruments

$V\&V$ Verification and validation